

July 2018

Mathematical and Numerical Modeling of Hybrid Adsorption and Biological Treatment Systems for Enhanced Nitrogen Removal

Karl A. Payne
University of South Florida, karlpayne009@gmail.com

Follow this and additional works at: <https://digitalcommons.usf.edu/etd>



Part of the [Civil Engineering Commons](#)

Scholar Commons Citation

Payne, Karl A., "Mathematical and Numerical Modeling of Hybrid Adsorption and Biological Treatment Systems for Enhanced Nitrogen Removal" (2018). *USF Tampa Graduate Theses and Dissertations*.
<https://digitalcommons.usf.edu/etd/7702>

This Dissertation is brought to you for free and open access by the USF Graduate Theses and Dissertations at Digital Commons @ University of South Florida. It has been accepted for inclusion in USF Tampa Graduate Theses and Dissertations by an authorized administrator of Digital Commons @ University of South Florida. For more information, please contact digitalcommons@usf.edu.

Mathematical and Numerical Modeling of Hybrid Adsorption and Biological
Treatment Systems for Enhanced Nitrogen Removal

by

Karl A. Payne

A dissertation submitted in partial fulfillment
of the requirements for the degree of
Doctor of Philosophy in Civil Engineering
Department of Civil and Environmental Engineering
College of Engineering
University of South Florida

Co-Major Professor: Maya Trotz, Ph.D.
Co-Major Professor: Sarina Ergas, Ph.D.
Jeffrey A. Cunningham, Ph.D.
Mahmood Nachabe, Ph.D.
Bo Zeng, Ph.D.
Razvan Teodorescu, Ph.D.

Date of Approval:
June 30, 2018

Keywords: nitrification, denitrification, computational, ion exchange, algal processes

Copyright © 2018, Karl A. Payne

DEDICATION

This dissertation is dedicated to my family, friends, colleagues, and professors that have served as a great source of inspiration throughout my academic career.

ACKNOWLEDGEMENTS

I would like to extend my sincerest gratitude to everyone that supported me in making this work possible. To my wife Trisha Payne for being a reservoir of strength and my family and friends for their relentless support and words of encouragement. To Dr. Maya Trotz and Dr. Sarina Ergas, for your enduring patience, support, and encouragement in guiding and mentoring me throughout my doctoral journey. To Dr. Cunningham, for extolling the virtues of balancing between simplicity and accuracy in modeling phenomena. To Dr. Nachabe, for always having an open door whenever I needed guidance. I would also like to thank my committee members Dr. Teodorescu and Dr. Bo Zeng, and my dissertation chair Dr. Yuncheng You. I would like to thank Dr. James Mihelcic for his words of wisdom and support. Thank you to my colleagues, Ram Kumar, Veronica Aponte-Morales, Nadezha Zalivina, Michelle Henderson, Meng Wang, Laura Rodriguez-Gonzalez, Qiaochong He, Cove Capodice, Wainella Isaacs, Maya Carrasquillo, Justine Stocks, Charlotte Haberstroh, Amuyl Miriyala, Helene Kassouf, Phillip Dixon, Emma Lopez-Ponnada, and Adib Amini.

The material in this dissertation was made possible by USEPA grant 83556901, NSF PIRE grant 1243510, and NSF REU grant 1156905. Its contents are solely the responsibility of the grantee and do not necessarily represent the official views of these agencies. Further, these agencies do not endorse the purchase of any commercial products or services mentioned in this dissertation.

TABLE OF CONTENTS

LIST OF TABLES	iv
LIST OF FIGURES	v
ABSTRACT.....	vii
CHAPTER 1: INTRODUCTION	1
1.1 Background and Motivation	1
1.2 Research Questions and Objectives	4
1.3 References.....	7
CHAPTER 2: LITERATURE REVIEW	9
2.1 Onsite Wastewater Treatment Systems (OWTS)	9
2.2 Ion Exchange Processes	10
2.2.1 Ion Exchange Equilibrium and Kinetics	11
2.3 Biological Processes	15
2.3.1 Nitrification.....	15
2.3.2 Denitrification.....	17
2.3.3 Biofilm Dynamics.....	18
2.3.4 Algal Processes for Nitrogen Removal.....	22
2.4 Numerical Framework	24
2.4.1 Finite Difference Method (FDM)	24
2.4.2 Finite Difference Implementation of the Homogeneous Surface Diffusion Model (HSDM).....	26
2.5 References	30
CHAPTER 3: BIOREGENERATION OF CHABAZITE DURING NITRIFICATION OF ANAEROBICALLY DIGESTED CENTRATE: EXPERIMENTAL AND MODELING STUDIES	35
3.1 Introduction.....	35
3.2 Materials and Methods.....	38
3.2.1 Anaerobically Digested Swine Waste Centrate	38
3.2.2 Chabazite.....	38
3.2.3 Ion Exchange Studies.....	39
3.2.4 Batch Nitrification Studies.....	39
3.2.5 Chabazite-Amended Nitrification Studies	40
3.2.6 Analytical Methods.....	41
3.2.7 Data Analysis	41
3.3 Mathematical Model Development.....	42

3.4 Results and Discussion	46
3.4.1 Ion Exchange Studies: Equilibrium and Kinetics	46
3.4.2 Nitrification Inhibition Studies	49
3.4.3 Chabazite-Assisted Nitrification	51
3.4.4 Assessment of Mathematical Model	53
3.5 Supplementary Information	55
3.5.1 Derivation of Equation for Aqueous-Phase Concentration of Na^+	55
3.5.2 Numerical Approximation	57
3.6 References	58
 CHAPTER 4: HYBRID ALGAL PHOTOSYNTHESIS AND ION EXCHANGE (HAPIX) PROCESS FOR HIGH AMMONIUM STRENGTH WASTEWATER TREATMENT	
4.1 Introduction	61
4.2 Materials and Methods	64
4.2.1 Characteristics of Anaerobic Digester Centrate	64
4.2.2 HAPIX Reactor Setup	65
4.2.3 Analytical Methods	66
4.2.4 Statistical Analysis	67
4.3 Mathematical Modeling	67
4.4 Results and Discussion	71
4.4.1 NH_4^+ Removal in HAPIX Reactors	71
4.4.2 Temporal Variation of Cations in HAPIX Reactors	73
4.4.3 Biomass Production	74
4.4.4 Effect of Zeolite Dosages on Intracellular Contents of Biomass	75
4.5 Assessment of Mathematical Model for HAPIX	78
4.5.1 HAPIX Model Parameter Determination	78
4.5.2 Prediction of NH_4^+ Concentrations in Aqueous Phase	81
4.5.3 Prediction of Microalgae Biomass Concentration	82
4.6 Conclusions	83
4.7 Supplementary Information	84
4.8 References	87
 CHAPTER 5: MODELING OF MASS TRANSPORT AND BIODEGRADATION IN A HYBRID ADSORPTION AND MIXOTROPHIC DENITRIFICATION BIOREACTOR	
5.1 Introduction	92
5.2 Materials and Methods	95
5.2.1 Batch and Column Experiments	95
5.3 Mathematical Model Development	98
5.3.1 Mass Transport Processes	100
5.3.2 Initial and Boundary Conditions	103
5.4 Numerical Approach	105
5.5 Estimation of Model Parameters	106

5.6 Results and Discussion	108
5.7 Conclusions.....	111
5.8 References	112
CHAPTER 6: CONCLUSIONS AND RECOMMENDATIONS	114
APPENDIX A: COPYRIGHT PERMISSIONS	121
APPENDIX B: SUPPLEMENTARY DATA.....	123

LIST OF TABLES

Table 3.1 Characterization of anaerobically digested swine waste centrate.....	40
Table 3.2 Parameters used to simulate concentration of chemical species in the bioreactors	56
Table 4.1 Characteristics of centrate from anaerobic digestion of waste activated sludge	65
Table 4.2 Profiles of fatty acids of algae harvested in HAPIX reactors from Phase 1 and Phase 3 (% of total fatty acids)	78
Table 4.3 Parameters used in numerical simulation of concentration profiles and the sensitivity scores	80
Table 5.1 Composition of wastewater used in T-SHAD experiments.....	98
Table 5.2 Definition of non-dimensional variables and dimensionless groups characterizing the T-SHAD system	102
Table 5.3 Definition of parameters appearing in dimensionless numbers.....	111
Table B1 Nitrogen species and sodium data for bioreactor without chabazite.....	123
Table B2 Nitrogen species and sodium data for bioreactor with chabazite.....	124

LIST OF FIGURES

Figure 2.1 Passive two-stage biofilters for nitrification followed by denitrification	10
Figure 2.2 Major components of biofilm system and conceptualization of: A) continuum-scale approach, B) discrete-element approach, C) discrete-particle approach	20
Figure 2.3 One dimensional finite difference grid discretized into $N + 1$ grid points	25
Figure 2.4 Discretization of a zeolite particle into radial intervals showing diffusion of NH_4^+ into the zeolite and Na^+ out of the zeolite	28
Figure 3.1 Conceptualization of the IX and bioregeneration processes occurring within the bioreactors for NH_4^+ -N removal	42
Figure 3.2 Ion exchange equilibrium: (A) IX isotherm model for NH_4^+ uptake; B) Effect of chabazite dose on the observed removal efficiency of NH_4^+	47
Figure 3.3 IX kinetics for NH_4^+ uptake onto chabazite and release of counterion Na^+	48
Figure 3.4 Nitrification inhibition: Effect of NH_4^+ -N concentration on nitritation and nitratation reaction rate	50
Figure 3.5 Nitrification without chabazite addition: (A) NH_4^+ concentration history over time, (B) NO_2^- and NO_3^- concentration histories over time.....	51
Figure 3.6 Nitrification with chabazite addition: (A) Simulated and experimental ammonium and sodium concentration during nitrification of 1,000 mg NH_4^+ -N L^{-1} , (B) Simulated and experimental nitrite and nitrate production during nitrification of 1,000 mg NH_4^+ -N L^{-1}	52
Figure 4.1 Overall operational strategy of HAPIX reactors	66
Figure 4.2 Temporal changes in cation concentrations in HAPIX reactors (A) IA-60: chabazite dosage of 60 g L^{-1} ; (B) IA-150: chabazite dosage of 150 g L^{-1} ; and (C) IA-250: chabazite dosage of 250 g L^{-1}	72
Figure 4.3 Algal biomass growth over time.....	75
Figure 4.4 Intercellular contents of algae harvested in HAPIX reactors	76

Figure 4.5 (A) NH_4^+ concentration in HAPIX reactor over time; (B) Algae biomass concentration in HAPIX reactor over time	80
Figure 4.6 NH_4^+ concentration history in HAPIX reactor over time (A) dosage of 60 g L^{-1} , (B) dosage of 250 g L^{-1}	82
Figure 4.7 Algae biomass concentration in HAPIX reactors over time, (A) dosage of 60 g L^{-1} , (B) dosage of 250 g L^{-1}	83
Figure 4.8 Isotherm study of NH_4^+ -N adsorption by zeolite after 24 hours	85
Figure 4.9 Kinetic study of NH_4^+ -N adsorption by 150 g L^{-1} chabazite after 24 hours	85
Figure 4.10 Effect of chabazite dose on the observed removal efficiency of NH_4^+	86
Figure 4.11 IX kinetics for NH_4^+ uptake onto chabazite and release of co-ion Na^+	86
Figure 5.1 Column A shows the T-SHAD column and column B shows the tire-only-column.....	97
Figure 5.2 Conceptualization of major processes occurring within the T-SHAD bioreactor	100
Figure 5.3 Phases of the experiment simulated and used for model initialization	104
Figure 5.4 Mathematical model and experimental data for NO_3^- - N consumption and SO_4^{2-} -S production for an SOD microcosm over a 6.5-day period	107
Figure 5.5 Mathematical model and experimental data for NO_3^- - N from effluent of the T-SHAD column	109
Figure 5.6 Mathematical model and experimental data for SO_4^{2-} - S from effluent of the T-SHAD column.....	110

ABSTRACT

High nutrient loading into groundwater and surface water systems has deleterious impacts on the environment, such as eutrophication, decimation of fish populations, and oxygen depletion. Conventional onsite wastewater treatment systems (OWTS) and various waste streams with high ammonium (NH_4^+) concentrations present a challenge, due the inconsistent performance of environmental biotechnologies aimed at managing nutrients from these sources.

Biological nitrogen removal (BNR) is commonly used in batch or packed-bed reactor configurations for nitrogen removal from various waste streams. In recognition of the need for resource recovery, algal photobioreactors are another type of environmental biotechnology with the potential for simultaneously treating wastewater while recovering energy. However, irrespective of the technology adopted, outstanding issues remain that affect the consistent performance of environmental biotechnologies for nitrogen removal and resource recovery. In OWTS, transient loading can lead to inconsistent nitrogen removal efficiency, while the presence of high free ammonia (FA) can exert inhibitory effects on microorganisms that mediate transformation of nitrogen species as well as microalgae that utilize nitrogen. Therefore, to overcome these challenges there have been experimental studies investigating the addition of adsorption and ion exchange (IX) media that can temporarily take up specific nitrogen ions.

Bioreactors comprised of microorganisms and adsorption/IX media can attenuate transient loading as well as mitigate inhibitory effects on microorganisms and microalgae; however, the interplay between physicochemical and processes in these systems is not well understood. Therefore, the main objective of this dissertation was to develop theoretical and numerical models

that elucidate the complex interactions that influence the fate of chemical species in the bioreactors.

To achieve this objective and address the issues related to improving the understanding of the underlying mechanisms occurring within the environmental biotechnologies investigated, the following three research studies were done: (i) experimental and theoretical modeling studies of an IX-assisted nitrification process for treatment of high NH_4^+ strength wastewater (Chapter 3), (ii) theoretical and numerical modeling of a hybrid algal photosynthesis and ion exchange (HAPIX) process for NH_4^+ removal and resource recovery (Chapter 4), and (iii) mathematical and numerical modeling of a mixotrophic denitrification process for nitrate (NO_3^-) removal under transient inflow conditions (Chapter 5).

The experimental results for the IX-assisted nitrification process showed that by amending the bioreactor with zeolite, there was a marked increase in the nitrification rate as evidenced by an increase in NO_3^- production from an initial concentration of 3.7 mg-N L^{-1} to 160 mg-N L^{-1} . This increase is approximately an order of magnitude greater than the increase in the reactor without chabazite. Therefore, the experimental studies provided support for the hypothesis that IX enhances the nitrification process. To garner further support for the hypothesis and better understand the mechanisms in the bioreactor, a novel mathematical model was developed that mechanistically describes IX kinetics by surface diffusion coupled with a nitrification inhibition model described by the Andrews equation. The agreement between the model and data suggests that the mathematical model developed provides a theoretically sound conceptual understanding of IX-assisted nitrification.

A model based on the physics of Fickian diffusion, IX chemistry, and algal growth with co-limiting factors including NH_4^+ , light irradiance, and temperature was developed to describe a

batch reactor comprised of microalgae and zeolite. The model can reproduce the temporal history of NH_4^+ in the reactor as well as the growth of microalgae biomass. The mathematical model developed for the HAPIX process balances between simplicity and accuracy to provide a sound theoretical framework for mechanisms involved.

In OWTS, transient inflow conditions have an influence on the performance of environmental biotechnologies for nitrogen removal. Prior experiments have shown that for denitrification, a tire-sulfur hybrid adsorption and denitrification (T-SHAD) bioreactor consistently removes nitrogen under varying influent flow and concentration conditions. To enhance the understanding of the underlying mechanisms in the T-SHAD bioreactor, a mathematical model describing mass transport of NO_3^- and SO_4^{2-} in the aqueous phase and mixotrophic denitrification was developed. Additionally, a numerical tool to solve the mathematical model was implemented and compared to previously conducted experiments. Results from the numerical simulations capture the trend of the experimental data showing approximately 90% NO_3^- -N removal under varying flow conditions. Moreover, the model describes the effluent characteristics of the process showing a transient response in correspondence the changes in fluid velocity.

The new tools developed provide new insight into the underlying mechanisms of physical, chemical, and biological processes within these bioreactors. The tools developed in this dissertation have a potential broad impact in environmental biotechnology for wastewater treatment in on-site systems, for treatment of high strength wastewater, and can be extended easily for stormwater management systems aimed at mitigating high nutrient loading to the environment.

CHAPTER 1: INTRODUCTION

1.1 Background and Motivation

The discharge of excess nitrogen (N) to surface and groundwater systems has deleterious environmental impacts (USEPA, 2011). One such environmental impact is eutrophication, which significantly degrades water quality and exacerbates problems of harmful algae blooms (HABs), and sea grass mortality (USEPA, 2011). Sources of excess N include domestic and industrial wastewater treatment facilities, agricultural runoff, stormwater runoff, and atmospheric deposition. Increased global demand for livestock derived products has spurred growth of confined animal feeding operations (CAFOs). Anaerobic digesters (ADs) are being promoted to treat the waste from these systems which have high organic matter and nitrogen concentrations. Despite that, relatively high NH_4^+ concentrations (800-4000 mg L^{-1}) remain in the AD effluent (Deng et al., 2008). Another predominant source of N responsible for accelerating eutrophication is the effluent from onsite wastewater treatment systems (OWTS). In the US, approximately one-third of the population relies on OWTS for wastewater treatment (Lowe et al., 2013). Conventional OWTS are comprised of a septic tank, which primarily separates solids, a drainfield, and a soil infiltration area where biological treatment and pathogen removal occur. These systems have inconsistent performance both hydraulically and from a N removal perspective, which leads to contamination of ground and surface waters (Siegrist et al., 2013).

Biological N removal (BNR) is one of the most common methods for removing N from the waste streams of high NH_4^+ strength wastewater streams and OWTS. BNR utilizes biologically facilitated nitrification and denitrification processes for converting NH_4^+ to NO_3^- (nitrification)

and subsequently NO_3^- to N_2 (denitrification). Additionally, given the need for enhanced nutrient and energy recovery, wastewater treatment systems that utilize algae for N removal while simultaneously producing algal biomass for biofuels and agricultural use have been proposed. However, there are challenges associated with BNR for removal of high NH_4^+ strength wastewater, such as the inhibitory effect of NH_3 on the rate of nitrification (Anthonisen et al., 1976). This same inhibitory effect can also pose problems with algal wastewater treatment processes (Crofts 1966; Lin et al. 2007; Park et al. 2010). Recently, studies have shown that amendment of bioreactors with natural zeolites can ease this inhibitory effect on biological nitrification and algal processes in high NH_4^+ strength wastewater applications (Aponte-Morales et al., 2018; Wang et al., 2018).

Factors affecting OWTS solely reliant on BNR include long idle periods, dynamic influent loading conditions and infrequent maintenance (Oakley et al., 2010). During idle periods, the substrates required for microbial activity are unavailable, while periods of high loading rates leads to nutrient influx in excess of the maximum substrate utilization rate. Therefore, there has been research interest in combining physical and chemical processes with BNR to overcome the challenges associated with systems that depend strictly on biological processes (Rodriguez-Gonzalez et al., 2015).

The advantage of hybrid processes that combine BNR with physical and chemical mechanisms in OWTS is that during periods of high nutrient loading the sorbent adsorbs the nutrient, while desorption and nitrification/denitrification occur during periods of low nutrient loading. Previous experimental studies on bioreactors utilizing clinoptilolite as an IX material in the first stage (nitrification) of OWTS have shown total N reduction greater than 90% (Hirst et al., 2013). For denitrification, a novel process, referred to as a tire-sulfur hybrid adsorption

denitrification (T-SHAD) has shown efficacy for nitrate (NO_3^-) removal and relatively low SO_4^{2-} production (Krayzelova et al., 2014).

Mathematical and numerical models are useful tools that elucidate the understanding of the relationship between physical, chemical, and biological processes. Computational models also serve as decision support tools that facilitate proper planning and design of treatment systems (Siegrist et al., 2009). The approach to modeling of bioreactors generally falls into two categories: (i) analytical models, and (ii) numerical models. In the case of analytical models, a closed form solution is sought to ordinary differential equations (ODEs) or partial differential equations (PDEs) that describe mechanisms within the system.

However, for complex boundary conditions and geometries these approaches are often precluded. Numerical approaches are therefore required to solve the multi-physics problems that represent mechanisms in hybrid treatment systems. There have been research studies of the separate processes, for example studies focused on surface diffusion models of ion exchange (IX) in zeolites and microporous materials (Valverde et al., 2005; Krishna 2006; Lito et al., 2014), and those dedicated to biofilm dynamics on inert substrata for wastewater treatment applications (Wanner, 1996; Eberl, 2001; Tierra et al., 2015). However, there is a dearth of research investigating the interaction between biological and IX mechanisms, perhaps due to the complexity involved in developing such models.

Mathematical modeling efforts in biofilm granular activated carbon (BGAC) systems and biofilters have processes in common with hybrid and biological treatment systems (HABiTS); however, special considerations must be given to the counter-diffusional nature of ion fluxes, high concentrations of the influent wastewater that can lead to self-inhibition issues, and the biofilm mediated mechanisms that cause shifts in the equilibration of nitrogen species. Therefore, this

dissertation develops new theoretical and numerical modeling capabilities that elucidate the interrelationships between physical, chemical, and biological processes within HABiTS. Moreover, the mathematical and computational tools developed facilitate creating novel bioreactor designs and enhancing process performance for environmental biotechnologies incorporating IX, adsorption, and biodegradation mechanisms.

1.2 Research Questions and Objectives

This dissertation addresses three different bioreactors for enhanced N removal. The first system considered (Chapter 3) addresses the problem of overcoming inhibition during nitrification of high ammonia strength wastewater. The batch reactor was comprised of an IX material, chabazite, as well as nitrifying bacteria. A theoretical framework was developed to describe IX kinetics and nitrification with inhibitory kinetics. A new numerical tool was developed that enables simulating the fate of NH_4^+ , NO_2^- , NO_3^- , and Na^+ in the bioreactor.

The second system considered (Chapter 4) addresses the problem of overcoming inhibition during of high ammonia strength wastewater using algal processes for NH_4^+ removal, while simultaneously recovering algal biomass as an agriculture product. The batch photobioreactor reactor was comprised of an IX material, chabazite, as well as algae. A theoretical model was developed to capture IX kinetics and algal biomass growth. A novel computational tool was developed that facilitates simulating the temporal histories of NH_4^+ and microalgae growth in the photobioreactor.

The third system modeled (Chapter 5), was a packed-bed bioreactor for denitrification of wastewater in an OWTS. The reactor materials consisted of scrap tire chips, oyster shells, and elemental sulfur. A theoretical model was developed to capture mass transport by advection, dispersion, and mixotrophic denitrification in the bulk liquid. A novel computational tool was

implemented that facilitates simulating the spatio-temporal dynamics of NO_3^- -N and SO_4^- -S under transient inflow conditions

The main objective of this dissertation was to develop new theoretical models and numerical tools that predict the evolution of chemical species in three different types of novel bioreactors that combine IX/adsorption with microbial and algal processes for treatment of high strength wastewater and nitrified OWT.

The following research questions and corresponding specific objectives guide this dissertation:

The first research question (Chapter 3) was, how accurately does an internal diffusion mass transfer model coupled with a bioprocess model that considers a single limiting substrate predict nitrogen speciation in a bioreactor comprised of zeolite and nitrifying microorganisms? The specific objectives were to:

- Develop a homogenous surface diffusion model (HSDM) for surface diffusion kinetics within the intra-crystalline zeolite structure, with an appropriate boundary condition at the zeolite-bulk interface that establishes equilibrium between the solid and liquid phases.
- Develop bioprocess kinetic models of nitrification and combine with the HSDM model.
- Implement a numerical algorithm to transform the system of PDEs into algebraic expressions and create a computer code to simulate the process.
- Conduct side-by-side control and hybrid bioreactor experiments to investigate the effect of zeolite amendment on easing nitrification inhibition.
- Validate the model by comparing simulation results with experimental NH_4^+ , NO_3^- , NO_2^- , and Na^+ concentration data.

The second research question (Chapter 4) was, can a mechanistic model of surface diffusion combined with a kinetic algal process model predict the temporal history of nitrogen species and microalgae growth in a bioreactor with zeolite and microalgae? The specific objectives were:

- Combine a kinetic model of nitrogen utilization by algae under multiple limiting factors (NH_4^+ , light, temperature) with the HSDM.
- Create a numerical model that predicts microalgae growth, and the concentration of NH_4^+ in the bioreactor as a function of time.
- Calibrate the mathematical model to experimental data derived from experiments for a specific zeolite dosage.
- Validate the model by comparing simulation results with experimental data of NH_4^+ , and microalgae biomass to experimental data for two different zeolite dosages from the calibrated model.

The third research question (Chapter 5) was, how does a mathematical model of mass transport by advection, dispersion, and mixotrophic denitrification under varying influent velocity conditions predict the breakthrough characteristics of an attached growth T-SHAD bioreactor? The specific objectives were:

- Develop a mathematical model that translates the simplified system representation into mathematical equations.
- Estimate the relevant model parameters either via literature or by independently conducted experiments.

- Simulate mass transport by advection, dispersion, combined with mixotrophic denitrification and investigate the numerical model behavior for the T-SHAD column under varying rates of substrate utilization.

Finally, Chapter 6 provides conclusions and recommendations based on the various research questions addressed in Chapters 3 through 5.

1.3 References

Anthonisen, A. C.; Loehr, R. C.; Prakasam, T. B. S.; Srinath, E. G. Inhibition of Nitrification by Ammonia and Nitrous Acid. *J. Water Pollut. Control Fed.* **1976**, 48, (5), 835-852.

Aponte-Morales, V. E.; Payne, K. A.; Cunningham, J. A.; Ergas, S.J. Bioregeneration of Chabazite During Nitrification of Centrate from Anaerobically Digested Livestock Waste: Experimental and Modeling Studies. *Environ. Sci. Technol.* **2018**, 52(7), 4090-4098.

Crofts, A.R. Uptake of ammonium ion by chloroplasts, and its relation to photophosphorylation. *Biochem. Biophys. Res. Comm.* **2006**, 24(5), 725-731.

Deng, L.; Zheng, P.; Chen, Z.; Mahmood, Q. Improvement in post-treatment of digested swine wastewater. *Bioresour. Technol.* **2008**, 99(8), 3136-3145.

Eberl, H. J.; Parker, D. F.; van Loosdrecht, M. A new deterministic spatio-temporal continuum model for biofilm development. *Comput. Math. Method Medic.* **2001**, 3(3), 161-175.

Hirst, J. E.; Anderson, D. L.; Smith, D. P. The Florida Onsite Sewage Nitrogen Reductions Strategies (FOSNRS) Study: Project Overview and Preliminary Results. Florida Water Resources Conference. April 29, 2013 at Orlando, Florida, 2013.

Krayzelova L., Lynn T. J.; Banihani Q.; Bartacek J.; Jenicek P.; Ergas, S. J. A Tire-Sulfur Hybrid Adsorption Denitrification (T-SHAD) process for decentralized wastewater treatment. *Water Res.* **2014**, 61, 191-199.

Krishna, R.; Wesselingh, J. A. The Maxwell-Stefan approach to mass transfer. *Chem. Eng. Sci.* **1997**, 52(6), 861-911.

Krishna, R.; Van Baten, J. M. Describing binary mixture diffusion in carbon nanotubes with the Maxwell–Stefan equations. An investigation using molecular dynamics simulations. *Indus. Eng. Chem. Res.* **2006**, 45(6), 2084-2093.

Lin, L.; Chan, G.Y.S.; Jiang, B.L.; Lan, C.Y. Use of ammoniacal nitrogen tolerant microalgae in landfill leachate treatment. *Waste Manage.* **2007**, 27(10), 1376-1382.

Lito, P. F.; Cardoso, S. P.; Loureiro, J. M.; Silva, C. M. Ion exchange equilibria and kinetics. In *Ion Exchange Technology I* (pp. 51-120). Springer Netherlands, 2012.

Lito, P. F.; Aniceto, J. P. S.; Silva, C. M. Modelling ion exchange kinetics in zeolite- type materials using Maxwell-Stefan approach. *Desal. and Water Treat.* **2014**, 52(28-30), 5333-5342.

Oakley, S. M.; Gold, A. J.; Oczkowski, A. J. Nitrogen control through decentralized wastewater treatment: process performance and alternative management strategies. *Ecol. Eng.* **2010**, 36(11), 1520-1531.

Rodriguez-Gonzalez, L.; Payne, K.; Trotz, M.; Ergas, S. J. Hybrid Adsorption and Biological Treatment Systems (HABiTS) for Onsite Wastewater Treatment. *Proceedings of the Water Environment Federation*, **2015**, (11), 4660-4672.

Siegrist, R. L.; McCray, J. E.; Lowe, K. S.; Cath, T. Y.; Munakata-Marr, J. Onsite and Decentralised Wastewater Systems: Advances from a decade of research and educational efforts. *Water* **2013**, 77-84.

Tierra, G.; Pavissich, J. P.; Nerenberg, R.; Xu, Z.; Alber, M. S. Multicomponent model of deformation and detachment of a biofilm under fluid flow. *J. R. Soc. Interface* **2015**, 12(106), 20150045.

USEPA. Reactive Nitrogen in the United States: An Analysis of Inputs, Flows, Consequences, and Management Options - A Report of the Science Advisory Board. EPA-SAB-11-013. USEPA, 2011.

USEPA. Reactive Nitrogen in the United States. A Report of the EPA Science Advisory Board. EPA Science Advisory Board, 2011.

Valverde, J. L.; De Lucas, A.; Carmona, M.; González, M.; Rodríguez, J. F. Model for the determination of diffusion coefficients of heterovalent ions in macroporous ion exchange resins by the zero-length column method. *Chem. Eng. Sci.* **2005**, 60(21), 5836-5844.

Wang, M., Payne, K., Tong, S., Ergas, S. A hybrid algal photosynthesis and ion-exchange (HAPIX) process for side stream wastewater treatment: Experimental and modeling studies. *Water Res.* **2018** (accepted).

Wanner, O.; Gujer, W. A multispecies biofilm model. *Biotechnol. Bioeng.* 1986, 28(3), 314-328.

CHAPTER 2: LITERATURE REVIEW

2.1 Onsite Wastewater Treatment Systems (OWTS)

It is estimated that centralized wastewater systems serve approximately 75% of the US population (Siegrist et al., 2013). Some of the growing concerns about the sustainability of these systems are related to the excessive chemical and energy requirements as well as sewer systems conveyance. Decentralized systems, such as septic systems, also referred to as onsite systems, require little maintenance and energy relative to centralized wastewater treatment systems, but have mainly been limited to suburban and rural areas (Siegrist et al., 2013).

A conventional OWTS is comprised of three main components: a septic tank, drainfield, and soil infiltration area. The septic tank is an underground treatment unit where domestic wastewater is collected, solids are separated, and some biological treatment occurs. The drainfield is an excavated trench with coarse media that achieves additional treatment by allowing the septic tank effluent to slowly infiltrate through the subsurface soil, which serves as a medium with an attached biofilm.

Conventional septic systems have challenges associated with limited nitrogen removal and inconsistent performance under transient loading conditions and long idle periods (Oakley, 2010). It is not surprising, therefore, that there has been an increasing interest in specialized onsite sewage treatment and disposal systems (FDOH, 2013). According to the Florida Department of Health (FDOH, 2013), the aim of these systems is to reach established performance standards for levels of carbonaceous biochemical oxygen demand (cBOD_5), total suspended solids (TSS), total nitrogen (TN), and total phosphorus (TP).

Passive two-stage bioreactors are promising technologies for improved performance of OWTS. In this configuration, effluent from a septic tank flows to the first bioreactor, which operates under unsaturated conditions and converts NH_4^+ to NO_3^- through biological nitrification (Figure 2.1). The second stage operates under saturated conditions, contains an electron donor, such as wood chips or elemental sulfur pellets, and denitrifies NO_3^- to N_2 . The effluent from the second packed-bed then flows to a drainfield for dispersal.

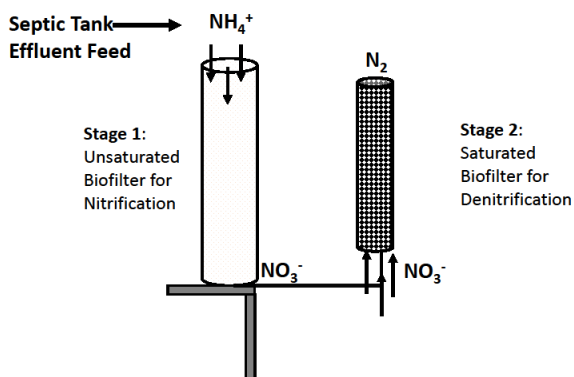


Figure 2.1: Passive two-stage biofilters for nitrification followed by denitrification
(Adapted from Hirst et al., 2013)

2.2 Ion Exchange Processes

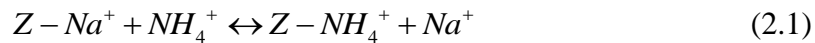
Ion exchange (IX) is the process by which ions in the aqueous phase are exchanged for a stoichiometrically equivalent amount of ions of the same charge in the solid phase (Helfferich, 1962). IX is an important process in several applications including analytical chemistry, biomedical engineering, and water and wastewater engineering. Environmental engineering applications of IX include water softening and removal of nutrients (Hedström, 2001). Many industrial applications use synthetic materials such as resin beads due to their high exchange capacity, fast kinetics, and uniform size and composition (Nazaroff and Alvarez-Cohen, 2001). However, there are natural materials that can be used for IX in wastewater treatment such as zeolites.

Zeolites are aluminosilicate materials that have been used as cation exchangers in wastewater treatment. There are several types of zeolites, with each type being distinguished by the silicon and aluminum ionic composition in the zeolitic framework (Weng and Peng, 2010). The variations in structure of zeolites endows each species with a unique set of physical and chemical properties. A three-dimensional structure of bonds between SiO_4^{4-} and AlO_4^{5-} forms tetrahedral building blocks within the zeolite framework (Payra and Dutta, 2003).

Within the structure of zeolites there exist channels filled with exchangeable cations and water molecules. Cations in solution can be exchanged with the cations within the zeolitic framework. Chabazite and clinoptilolite are among the zeolitic types with the most practical importance to N removal in wastewater treatment since they have a high affinity for NH_4^+ relative to the other zeolite species (Wang and Peng, 2010).

2.2.1 Ion Exchange Equilibrium and Kinetics

IX equilibria describe the relationship between the concentration of solute in the solid phase and the concentration of the solute present in solution at constant temperature. Approaches to IX equilibrium modeling include homogeneous and heterogeneous mass action laws and ion adsorption models (Lito et al., 2012). In the homogenous and heterogeneous mass law approaches, IX is described as a chemical reaction. For example, the equilibrium exchange reaction between sodium (Na^+) initially attached to the zeolite, Z, and NH_4^+ in solution is given by:



For example, the IX isotherm used in this dissertation is derived by using the equilibrium constant, K , which is found by the law of mass action applied to Equation 2.1:

$$K = \frac{[\text{Z} - \text{NH}_4^+][\text{Na}^+]}{[\text{Z} - \text{Na}^+][\text{NH}_4^+]} = \frac{q_{\text{NH}_4^+}[\text{Na}^+]}{(Q_{\text{max}} - q_{\text{NH}_4^+})[\text{NH}_4^+]} \quad (2.2)$$

where $q_{NH_4^+} = [Z - NH_4^+]$ is the NH_4^+ concentration in the solid phase, $[Z - Na^+] = (Q_{tot} - q_{NH_4^+})$ is the Na^+ concentration in the solid phase, $[Na^+]$ is the Na^+ concentration in the liquid phase, $[NH_4^+]$ is the NH_4^+ concentration in the liquid phase, and Q_{max} is the maximum IX capacity. Rearranging Equation 2.2 and making $q_{NH_4^+}$ the subject of the formula yields:

$$q_{NH_4^+} = \frac{KQ_{max}[NH_4^+]}{[Na^+] + K[NH_4^+]} \quad (2.3)$$

The coefficients Q_{max} and K are determined by fitting Equation 2.3 to isotherm data establishing the relationship between the solid-phase concentration of NH_4^+ and liquid-phase concentration of NH_4^+ and Na^+ .

The distinction between homogenous models and heterogeneous models is that in the heterogeneous case, IX sites are neglected and deviations from ideal behavior are accounted for by the introduction of activity coefficients in the solid and liquid phases (Lito et al., 2012). In contrast, ion adsorption models treat IX as an adsorption process, and semi-empirical models such as the Freundlich and Langmuir isotherms are fit to experimental isotherm data.

Diffusion is a microscopic mass transfer process that results from the random thermal motion of molecules; this process is known as Brownian motion (Mori, 1965). Due to the nanoporous nature of zeolites, the diffusion process is characterized by a jump diffusion process, which is inherently stochastic due to probabilistic jumps between IX sites (Auerbach, 2006). Capturing these mechanisms using kinetic models of IX in zeolites and microporous materials generally takes the following approaches: semi-empirical, Fickian-based diffusion models, Nernst-Planck (NP) equations, Maxwell-Stefan equations, and kinetic Monte Carlo (kMC) methods (Lito et al., 2012).

The kMC approach represents perhaps the most physically sound method to modeling surface diffusion in zeolites. Kinetic Monte Carlo models (kMC) are coarse-grained models that simulate diffusion based on ionic jumps between lattice sites (Paschek et al., 2001). However, the kMC approach requires knowledge of the three-dimensional porous zeolite network and specification of probabilistic jumps between IX sites. Therefore, simpler IX kinetic models have been developed, especially when the model purpose is for reactor design rather than understanding fundamental IX kinetic mechanisms.

The seminal work on semi-empirical modeling was done by Lagergren (1893), where the following pseudo-first order model was used:

$$\frac{d\bar{q}_i}{dt} = k_1(\bar{q}_{i,e} - \bar{q}_i) \quad (2.4)$$

where k_1 is the rate constant of first order sorption, $\bar{q}_{i,e}$ is the sorbed solute concentration at equilibrium and \bar{q}_i is the solute concentration in the solid phase at any time. The adsorption and desorption kinetics of NH_4^+ on clinoptilolite were investigated using various models including the pseudo-first order model (Kithome et al., 1998) as given in Equation 2.4. The other models evaluated included a parabolic diffusion model and the Elovich model (Kithome et al., 1998).

Another semi-empirical approach uses an integrated form of the pseudo-second order expression which takes the form:

$$\frac{t}{q_i} = \frac{1}{k_2 \bar{q}_{i,e}^2} + \frac{1}{\bar{q}_{i,e}} t \quad (2.5)$$

where k_2 is the rate constant of second order sorption. The kinetic model (Equation 2.5) provided an excellent fit to data for IX kinetics using zeolite 13X, a by-product from preparation potassium carbonate from potash ores (Zheng et al., 2008).

A mechanistic approach to modeling ionic flux driven strictly by a concentration gradient is based on Fick's laws. In the absence of an electrochemical gradient, for a spherical coordinate system the temporal evolution of ionic concentrations based on Fickian diffusion is given by:

$$\frac{\partial q_i}{\partial t} = D_s \left(\frac{\partial^2 q_i}{\partial r^2} + \frac{2}{r} \frac{\partial q_i}{\partial r} \right) \quad (2.6)$$

where D_s is the surface diffusion coefficient and r is a radial position within a solid particle. The Fickian-based approach has been successfully used to describe the kinetics of dissolved organic carbon (DOC) onto an anionic resin (Bu et al., 2010). The model has also been used in our research group for modeling the rate of uptake of NH_4^+ onto chabazite and is discussed in Chapters 3 and 4 of this dissertation.

A model that considers the effects of an electric field is the Nernst-Planck (NP) equation, which combines the Fickian diffusion model with an additional term accounting for an electric potential. The ionic flux based on the NP approach is given by:

$$J_i = -D_i \left(\frac{\partial q_i}{\partial r} \right) - D_i z_i q_i \frac{F}{R_{ideal} T} \left(\frac{\partial \phi}{\partial r} \right) \quad (2.7)$$

where D_i is the diffusion coefficient for the i^{th} ionic species, F is Faraday's constant, J_i is the ionic flux for the i^{th} ionic species, R_{ideal} is the ideal gas law constant, T is temperature, z_i is the charge of the i^{th} ionic species, and ϕ is the electric potential. The NP model has been used for modeling the kinetics of IX multicomponent systems; however, attention should be paid to the limit of validity of the model as ionic strength increases (Lito et al., 2012).

Another model of IX kinetics in zeolites that accounts for interactions between various ionic species as well as ion-solid interactions is the Maxwell-Stefan (MS) equation. The MS approach is one of the most theoretically sound approaches for modeling multicomponent transport for non-dilute systems and has been previously used for modeling IX kinetics in zeolites and

similar microporous materials (Krishna et al., 2002; Lito et al., 2014). The conceptual model for IX using the MS approach is similar to the Dusty Gas Model (Krishna and Wesselingh, 1997). The driving forces for an ionic flux are a chemical potential gradient and an electrostatic potential gradient. These driving forces are balanced by frictional forces that arise due to ion-ion and ion-solid interactions. To account for ion-solid interactions, a pseudo-species or so-called “dust” particles are introduced. The solid is stationary ($u_s=0$), and ionic velocities are relative to the stationary solid. Given these assumptions, the MS model is given by the following equation:

$$-\nabla \bar{\mu}_i - Fz_i \nabla \phi = \sum_{\substack{j=1 \\ j \neq i}}^{n_c} \frac{y_j RT(u_i - u_j)}{D_{ij}} + \frac{y_s RT u_i}{D_{is}} \quad (2.8)$$

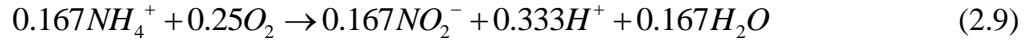
where D_{ij} is a MS surface diffusivity of ion pair i - j , D_{is} is a MS surface diffusivity for the interaction between an ion, i , and the fixed solid phase, u_i and u_j are the velocities of ions i and j relative to the solid, y_j is the molar fraction of component j in the solid phase, y_s is the molar fraction of fixed charged groups, and $\nabla \bar{\mu}_i$ is the surface chemical potential gradient of the i^{th} species. While the MS describes surface diffusion in a physically sound manner, the disadvantage is that diffusivities (D_{ij} and D_{is}) are introduced that are difficult to validate experimentally. In addition, the model is more challenging to numerically implement in comparison to Fickian-based models.

2.3 Biological Processes

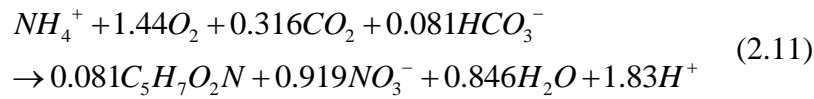
2.3.1 Nitrification

One of the biologically important redox reactions in the nitrogen cycle is nitrification, which is a two-step process facilitated by ammonia oxidizing bacteria (AOB) and/or archaea in the first step and nitrite oxidizing bacteria (NOB) in the second step. Recently, bacteria from the genus *Nitrospira* have been implicated in complete ammonia oxidation to nitrate (NO_3^-); a process referred to as comammox (Daims et al., 2015). Nevertheless, when considering the biochemical

reactions catalyzed by obligate aerobic nitrifiers in a two-step process, the stoichiometric relationships are given by (Rittmann and McCarty, 2001):



The overall stoichiometry of nitrification assuming a yield of 0.15 g of biomass ($C_5H_7O_2N$) per gram of substrate (NH_4^+-N) is given by Ahuja (2014) as:



Design of nitrification bioreactors can be potentially challenging due to the slow growth rate of nitrifying organisms, which can be attributed to factors such as their autotrophic and chemolithotrophic nature (Rittmann and McCarty, 2001).

Conventionally, models of microbially facilitated nitrification reactions are expressed as lumped models that ignore individual microbial reaction pathways. These models often take the form of Monod-type kinetics, which is expressed as (Monod, ;1949; Rittmann and McCarty, 2001):

$$r_u = \frac{\mu_{\max}}{Y} \left(\frac{N}{K_N + N} \right) \left(\frac{DO}{K_{DO} + DO} \right) \quad (2.12)$$

where μ_{\max} is the maximum specific growth rate, r_u is the rate of substrate utilization, Y is the yield coefficient, N is the NH_4^+-N concentration, DO is the dissolved oxygen concentration, and K_{DO} and K_N are the half-saturation constants for NH_4^+-N and DO , respectively. While the Monod-based approach does not capture in detail microbial pathways, well established numerical methods for the solution to ordinary differential equations (ODEs), such as Runge-Kutta techniques, can be used to estimate temporal changes in chemical species and biomass (Smith et al., 1998).

Recently, advances in microbiology have led to a more sophisticated alternative to using Monod-type expressions, known as genome-scale metabolic models (Tartakovsky et al., 2013). This more theoretically sound approach leverages data on genome sequences of microorganisms to understand gene function, thereby enabling the construction of reaction-based models of metabolism (Lovely, 2003). For example, a genome-scale, constraint-based model more accurately estimates NO_x emissions during the nitrification process (Mellbye et al., 2018).

Apart from the slow growing nature of nitrifiers, an important factor that can potentially affect nitrification kinetics is self-inhibition. This self-inhibitory process occurs when substrate concentrations are high and slows down the rate of substrate utilization. This inhibitory effect has implications for treatment of wastewater streams with high free ammonia (FA) concentrations. Modeling of nitrification under self-inhibiting conditions has commonly been described using Andrews kinetics (Andrews, 1968):

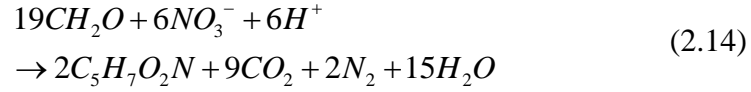
$$r_u = \frac{\mu_{\max}}{Y} \left(\frac{N}{\frac{N^2}{K_I} + K_N + N} \right) \quad (2.13)$$

where K_I is the inhibition coefficient. It should be noted that higher values of K_I correspond to a less significant inhibition, while lower K_I values result in a more significant inhibitory response. Thus in the case where $K_I \rightarrow \infty$, the expression in Equation 2.13 reduces to the Monod expression.

2.3.2 Denitrification

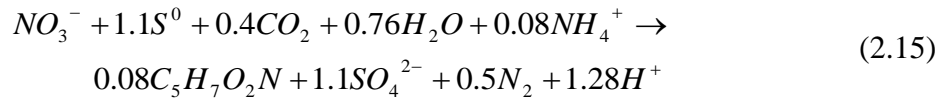
Denitrification is mediated by facultative bacteria that use NO₃⁻ or NO₂⁻ as a terminal electron acceptor under anoxic conditions. The electron donor for denitrification can either be an organic substrate or an inorganic compound such as S⁰, H₂, Fe²⁺ or pyrite (FeS₂). A stoichiometric

reaction for heterotrophic denitrification, including biomass synthesis, is (Rittmann and McCarty, 2001):



Lignocellulosic material, such as wood chips, is one of type of medium that has been used previously in OWTS as an organic substrate for heterotrophic denitrification (Schipper et al., 2010; Lopez-Ponnada et al., 2017).

Autotrophic denitrification with elemental sulfur (S^0) as the electron donor is given by (Batchelor and Lawrence, 1978):



The advantages of SOD for OWTS include (Sengupta et al., 2007): high NO_3^- removal efficiencies, low-cost since it is derived as a by-product of oil processing, and low biomass yield relative to heterotrophic denitrification. In SOD, for each gram of NO_3^- removed, the alkalinity consumed is approximately 4.5 g (as $CaCO_3$). Since inhibition of denitrification can occur below a pH of 5.5, solid-phase buffers are necessary for imparting alkalinity to bioreactors in OWTS (Sengupta et al., 2007). It has been shown previously that crushed oyster shell was the most suitable buffer when compared to marble chips and limestone (Sengupta et al., 2007).

2.3.3 Biofilm Dynamics

Biofilms are agglomerations of microorganisms that secrete extracellular polymeric substances (EPS) in response to environmental stress. EPS are comprised of biopolymers and provide the microbial community with structural integrity, which enables biofilms to resist shear stresses. Biofilms are found in diverse natural and engineered environments, such as soil surfaces and the surface of biofilter media. The benefits of biofilms in removal of nutrients such as nitrogen

have been demonstrated in several water and wastewater treatment studies showing effective removal of nitrogen species (Henze et al., 2008; Krayzelova et al., 2014).

Microorganisms within biofilms use a communication mechanism known as quorum sensing, whereby chemical signaling molecules are used to monitor population density of microbial species. Once a critical biomass density is reached, bacteria coordinate behavior by expressing genes that benefit the entire community (Ng and Bassler, 2009). Recently, it has been shown that biofilms may also communicate electrically by propagating K^+ ions facilitated by ion channels in microbial cell membranes (Prindle et al., 2015).

Computational biofilm models play an integral role in verifying experimental results and allow for testing new hypotheses, which would be otherwise difficult to accomplish experimentally. Processes affecting biofilm growth as well as contaminant fate and transport occur at multiple length and time scales. Substrate advection, diffusion, and reaction occur on time scales several orders of magnitude lower than microbial growth, decay, and detachment (Picioreanu et al., 2000). Moreover, multiple time scales, microbial diversity within biofilms, and the free boundary at the biofilm-liquid interface makes mathematical modeling of biofilm reactors a challenging task.

A review of biofilm modeling for wastewater applications was given by the IWA Task Group (Wanner et al., 2006). Biofilm models can broadly be placed into three categories: continuum, discrete grid-based, and discrete particle-based models, as shown in Figure 2.2. Wanner and Gujer (1986) are recognized as having developed one of the first continuum-scale biofilm models. The model was one-dimensional and considered horizontal growth away from the substratum. The 1D model treated the bulk liquid and biofilm as continuous phases. Advection-diffusion processes were considered in the liquid phase and reaction-diffusion processes were

accounted for in the biofilm phase. Biomass growth was perpendicular to the inert substratum and controlled by a velocity term.

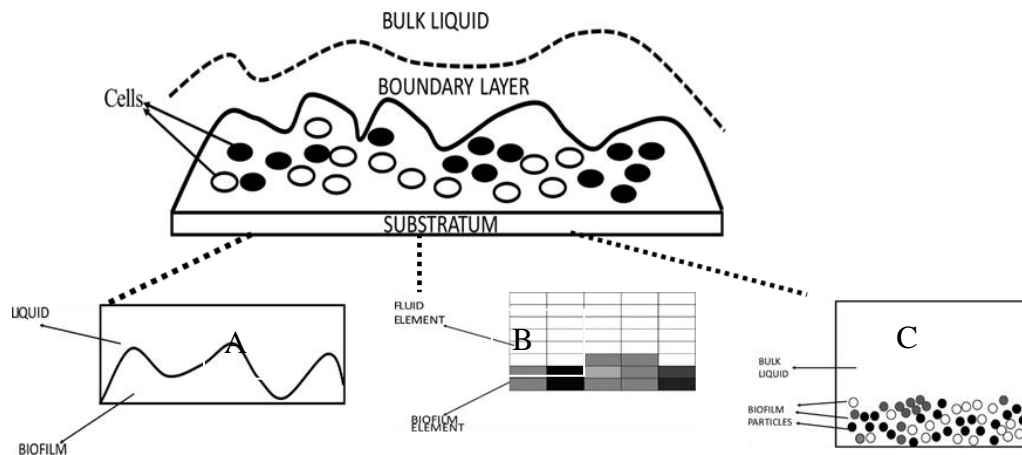


Figure 2.2: Major components of biofilm system and conceptualization of: A) continuum-scale approach, B) discrete-element approach, C) discrete-particle approach. (Adapted from Wanner et al., 2006)

Although the sophistication of continuum-scale models for biofilm dynamics has increased, issues remain in terms of the parameterization of diffusion coefficients in the biofilm phase. Also, because continuum-scale models are top-down rather bottom-up approaches the thickness of the hydrodynamic boundary layer and related concentration boundary layers need to be specified *a priori*.

Advances in experimental techniques have led to an enhanced understanding of biofilm structure. Confocal laser microscopy, a technique for imaging biofilm morphology and structure, highlighted the three-dimensional structure of biofilms (Picioreanu et al., 2000). These developments in biofilm imaging methods have motivated researchers to develop two and three-dimensional continuum-scale models (Eberl et al., 2001; Knutson et al., 2005). Irrespective of the dimensionality of continuum-scale models, a drawback is that the heterogeneity of the microbial community is not well represented. Therefore, discrete-based approaches were introduced to

enhance how biofilm growth models account for this microbial diversity. In discrete grid-based or lattice-based approaches, the model domain is discretized into biomass and fluid elements on a lattice. A mass balance equation is assigned to each lattice element, and when a critical biomass threshold is reached, cellular automaton rules are used to spread biomass to neighboring lattice cells (Tang et al, 2015). However, it has been noted that the rules for how biomass propagates throughout the grid are *ad hoc*. Picioreanu et al. (1998) developed a discrete-based biofilm model to investigate biofilm growth under various substrate and growth conditions. A dimensionless number, G , was introduced that indicated the relative importance of the biomass growth rate to the substrate transport rate, and is mathematically defined as:

$$G = \frac{l_z \mu_{\max} X_m}{D_{sub} C_{sub}} \quad (2.16)$$

where l_z is the biofilm thickness, X_m is the maximum biomass density, D_{sub} is the diffusion coefficient of the substrate in the liquid phase, and C_{sub} is the nutrient concentration in the liquid phase. For higher values of G (> 5), referred to as the transport limited regime, biofilm structure was found to be more irregular due to growth dominated by microorganisms closer to the bulk liquid. In contrast, under the growth limited regime ($G < 5$) biofilm structure was more smooth and compact due to a more homogenous distribution of substrates within the biofilms (Picioreanu et al., 1998).

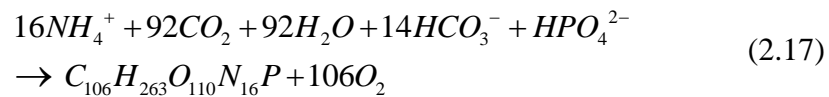
Discrete particle-based models, which are also referred to as individually-based models (IbM), were introduced to allow greater flexibility in terms of spatial movement of biomass. Biomass particles can represent different types of microorganisms and are assigned state variable such as mass and volume (Wanner et al., 2006). Kreft et al. (2001) developed an IbM model to investigate the impact of microbial interactions on biofilm dynamics, using a particle-based description to describe AOB and NOB as distinct entities. Diffusion processes that account for

nutrient transport were decoupled from growth processes since biofilm growth is typically on the order of days and diffusion is on the order of seconds. The model was capable of accurately representing the spatial-temporal distribution of nitrogen species in a nitrifying biofilm.

2.3.4 Algal Processes for Nitrogen Removal

Microalgae are photoautotrophic organisms that have received interest from a broad research community due to their potential to produce biofuels, biopolymers, and products with high protein content for the agriculture industry. In addition, microalgae have been beneficial for wastewater treatment in stabilization ponds to biodegrade organic matter, take up nitrogen and phosphorus, and remove heavy metals (Kosaric et al, 1974; Wilde and Benjamin, 1993; Silkin and Chubchikova, 2007).

Algal growth is dependent on multiple factors including the carbon source, light irradiance, inorganic macronutrients (N and P) and trace nutrients. A promising growth substrate for algae is the nutrient-rich centrate from anaerobic digestion (Park et al., 2010). The removal of nitrogen and algal growth dynamics have previously been investigated to demonstrate the viability of using wastewater as a growth substrate (Lee and Zhang, 2016). A biochemical equation for algal biosynthesis is given by (Ebeling et al., 2006):



where $C_{106}H_{263}O_{110}N_{16}P$ represents algal biomass. The stoichiometry of Equation 2.15 indicates that for each gram of NH_4^+ -N consumed approximately 15.8 grams of algal biomass are produced. Factors that can negatively impact algal processes are inhibition due to high nitrogen concentrations and photoinhibition associated with increasing light irradiance (Han et al., 2000).

Therefore, there have been efforts to better understand the optimal conditions for growth (Kumar et al., 2010) as well as alternative reactor designs to overcome these issues (Wang, 2018).

In general, microalgae kinetic models either use a single limitation or co-limitation approach. In single limitation models, it is commonly assumed that algal growth kinetics are either limited by a single substrate (N, P, CO₂) or by light intensity. For co-limitation models, either a threshold or multiplicative conceptualization is adopted (Lee and Zhang, 2016). The threshold approach assumes the most limited resource affects microalgae growth rate (De Groot, 1983; Spijkerman et al., 2011). In general, a commonly used expression for the threshold assumption is given by:

$$\mu = \min \left(\mu_A \frac{A}{K_A + A}, \mu_B \frac{B}{K_B + B} \right) \quad (2.18)$$

where A and B are limiting factors, μ_A and μ_B are the maximum growth rate of factors A and B , K_A and K_B are the corresponding half saturation constants. In contrast, the multiplicative theory assumes that multiple resources simultaneously affect growth (Lee and Zhang, 2016) and is given by:

$$\mu = \mu_{\max} \frac{A}{K_A + A} \cdot \frac{B}{K_B + B} \quad (2.19)$$

A model incorporating threshold and multiplicative models has been previously successfully implemented to model microalgae growth with centrate from an anaerobic digester as the growth medium (Lee and Zhang, 2016). The model assumed threshold limitation for nitrogen and phosphorus, whereas a multiplicative assumption was adopted for factors including CO₂, light intensity, and temperature. A general expression for the model is expressed as:

$$\mu = \mu_{\max} (f(N), f(P)) \cdot f(\text{CO}_2) \cdot f(I) \cdot f(T) \quad (2.20)$$

where $f(N)$, $f(P)$, $f(CO_2)$, $f(I)$, and $f(T)$ are functions of nitrogen, phosphorus, carbon dioxide, light intensity, and temperature.

2.4 Numerical Framework

2.4.1 Finite Difference Method (FDM)

The description of the physical, chemical, and biological processes occurring within the bioreactors in this dissertation is expressed in terms of ordinary differential equations (ODEs) and partial differential equations (PDEs). Given the complexity of mechanisms, analytical methods that provide closed formed solutions to the equations are precluded. Instead, in this dissertation the equations are discretized using the finite difference method (FDM), which entails transforming differential equations into difference equations, and subsequently solving a system of simultaneous equations (Leveque, 2007).

The FDM consists of the following four steps: (i) pre-processing to sub-divide the domain of interest into discrete elements or cells, (ii) formulation of a discrete model to obtain algebraic approximations of the differential equations representing the mathematical model, (iii) solving the system of algebraic equations to determine the field variables of interest, (iv) post-processing to visualize the spatio-temporal dynamics of the field variables. In this dissertation, the variables of interest are the concentrations of multiple ionic species, which vary temporally in the case of batch systems (Chapters 3 and 4) and both spatially and temporally in the case of fixed film reactors such as biofilters (Chapter 5).

Consider discretizing a domain bounded by $[a, b]$, where $a, b \in \mathbb{R}$ into $N + 1$ grid points/nodes as shown in Figure 2.3.

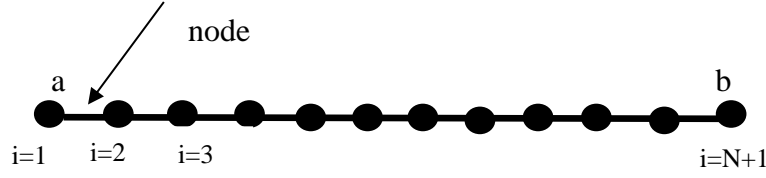


Figure 2.3: One dimensional finite difference grid discretized into $N + 1$ grid points

For an arbitrary function $F(x)$, taking a Taylor series expansion about the point $x = x_i$ in the grid results in:

$$F(x) = F(x_i) + \frac{dF}{dx}_{x=x_i} (x - x_i) + \frac{1}{2!} \frac{d^2 F}{dx^2}_{x=x_i} (x - x_i)^2 + \dots + \frac{1}{n!} \frac{d^n F}{dx^n}_{x=x_i} (x - x_i)^n + O_n \quad (2.21)$$

where O_n refers to higher order terms in the series. Evaluating the Taylor series at the point $x = x_{i+1}$ results in the following expression:

$$F(x_{i+1}) = F(x_i) + \frac{dF}{dx}_{x=x_i} (x_{i+1} - x_i) + \frac{1}{2!} \frac{d^2 F}{dx^2}_{x=x_i} (x_{i+1} - x_i)^2 + \dots + \frac{1}{n!} \frac{d^n F}{dx^n}_{x=x_i} (x_{i+1} - x_i)^n + O_n \quad (2.22)$$

As the grid interval gets small, the higher order terms can be ignored, and Equation 2.22 is truncated to get:

$$F(x_{i+1}) = F(x_i) + \frac{dF}{dx}_{x=x_i} h \quad (2.23)$$

where, we assume an equidistant grid spacing of $x_{i+1} - x_i = h$. Equation 2.23 can be rearranged to obtain a finite difference approximation for the first derivative:

$$\frac{dF}{dx}_{x=x_i} = \frac{F(x_{i+1}) - F(x_i)}{h} \quad (2.24)$$

It should be noted that the spatial derivative approximated by Equation 2.24 introduces a truncation error since higher order terms in the approximation are neglected. The other main source of error

incurred by the FDM is round-off error which is associated with the limited precision for computers to represent decimal quantities (Karniadakis and Kirby, 2003). The expression in Equation 2.24 is referred to as the forward difference approximation to the first derivative (Leveque, 2007). A similar approach can be adopted to derive a backward difference scheme, which can be written as:

$$\frac{dF}{dx}_{x=x_i} = \frac{F(x_i) - F(x_{i-1})}{h} \quad (2.25)$$

A combination of the forward (Equation 2.24) and backward (Equation 2.25) differences leads to a centered difference approximation, which is given by:

$$\frac{dF}{dx}_{x=x_i} = \frac{F(x_{i+1}) - F(x_{i-1}))}{2h} \quad (2.26)$$

The formulas in Equations 2.24 to 2.26 are explicit formulas meaning that the derivatives at a node are computed in terms of function values at neighboring nodes. While explicit formulas are relatively simple to implement and computationally efficient, the main disadvantage is that stable solutions are only obtained within a specific range (Leveque, 2007). If the criterion for stability is not satisfied, spurious oscillations are observed. Thus, in this dissertation we adopt implicit numerical schemes to approximate the derivatives in ODEs and partial differential equations (PDEs).

2.4.2 Finite Difference Implementation of the Homogeneous Surface Diffusion Model (HSDM)

Diffusion-reaction equations are mathematical models that have wide application in biology, chemistry, geology, and physics. In general, a diffusion-reaction equation takes the form:

$$\frac{\partial C}{\partial t} = D\Delta C + f(x, t, C) \quad (2.27)$$

where C is the variable of interest, D is a diffusion coefficient, $f(x, t, C)$ is a function accounting for reactions, and Δ is the Laplacian operator. In the batch bioreactor systems modeled in this dissertation, the term on the left-hand side of Equation 2.27 describes the temporal evolution of chemical species, the first term on the right-hand side describes intra-particle diffusion through zeolites, and the second term on the right-hand side represents biologically mediated processes.

Assuming an IX process between NH_4^+ and Na^+ , which are the main ions being exchanged for the zeolite considered in this dissertation, intra-particle diffusion is described by the HSDM:

$$\frac{\partial q_{\text{NH}_4^+}}{\partial t} = \frac{D_s}{r^2} \frac{\partial}{\partial r} \left(r^2 \frac{\partial q_{\text{NH}_4^+}}{\partial r} \right) \quad (2.28)$$

where $q_{\text{NH}_4^+}$ is the solid-phase concentration of NH_4^+ , D_s is the surface diffusion coefficient, r is the radial coordinate in the solid phase, and t is time. The following equations provide the initial and boundary conditions for the intra-zeolite concentration of NH_4^+ :

$$q_{\text{NH}_4^+}(t = 0, r) = 0 \quad (2.29)$$

$$\frac{\partial q_{\text{NH}_4^+}}{\partial r}(r = 0, t) = 0 \quad (2.30)$$

$$q_{\text{NH}_4^+}(r = R, t) = \frac{QKC_{\text{NH}_4^+}}{C_{\text{Na}^+} + KC_{\text{NH}_4^+}} \quad (2.31)$$

Figure 2.4 shows discretization of a spherical zeolite particle into radial intervals from the center of a particle to the radius. Here, we derive a numerical scheme for Equation 2.28 using a centered difference approximation for spatial derivatives and a Crank Nicolson scheme for the temporal discretization (Crank and Nicolson, 1947).

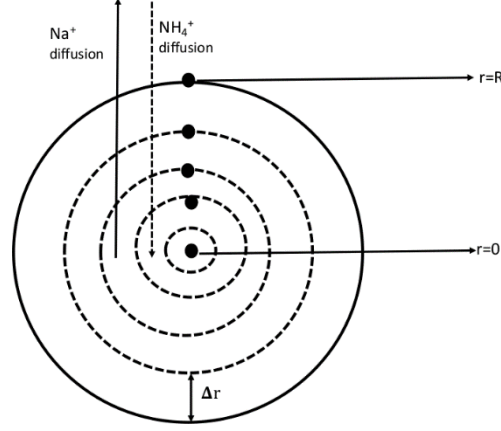


Figure 2.4: Discretization of a zeolite particle into radial intervals showing diffusion of NH_4^+ into the zeolite and Na^+ out of the zeolite

Applying the product rule to the solid-phase mass balance expression (Equation 2.28) yields:

$$\frac{\partial q}{\partial t} = D_s \frac{\partial^2 q}{\partial r^2} + \frac{2}{r} D_s \frac{\partial q}{\partial r} \quad (2.32)$$

A finite difference approximation to the temporal term is given by:

$$\frac{dq}{dt} = \frac{q_j^{n+1} - q_j^n}{\Delta t} \quad (2.33)$$

where q_j^{n+1} is the concentration at the j^{th} node for a new time level and q_j^n is the concentration at the j^{th} node for an old time level. Applying a centered difference scheme and Crank-Nicolson temporal discretization to the first term on the right side of Equation 2.32 for nodes from 2 to N yields:

$$D_s \frac{\partial^2 q}{\partial r^2} = \frac{D_s}{2(\Delta r)^2} [q_{j+1}^{n+1} - 2q_j^{n+1} + q_{j-1}^{n+1} + q_{j+1}^n - 2q_j^n + q_{j-1}^n] \quad (2.34)$$

Applying the same finite difference approximation to the second term on the right-hand side of Equation 2.32 results in:

$$\frac{2}{r} D_s \frac{\partial q}{\partial r} = \frac{D_s}{2r_j(\Delta r)} [q_{j+1}^{n+1} - q_{j-1}^{n+1} + q_{j+1}^n - q_{j-1}^{n+1}] \quad (2.35)$$

Combining Equations 2.33 – 2.35 and rearranging to set the terms for time level $n+1$ on the left-hand side and time level n on right-hand side yields:

$$\begin{aligned} & \left(\frac{\lambda}{j-1} - \lambda \right) q_{j-1}^{n+1} + (1 + 2\lambda) q_j^{n+1} + \left(\frac{-\lambda}{j-1} - \lambda \right) q_{j+1}^{n+1} \\ & = \left(\lambda - \frac{\lambda}{j-1} \right) q_{j-1}^n + (1 - 2\lambda) q_j^n + \left(\lambda + \frac{\lambda}{j-1} \right) q_{j+1}^n \end{aligned} \quad (2.36)$$

where $\lambda = \frac{D_s \Delta t}{2(\Delta r)^2}$ and $r = (j-1)\Delta r$.

In terms of the boundary condition at the center of the particle, that is at node $j=1$, we impose a Neumann boundary condition, and approximate the derivative using an Euler method:

$$\left. \frac{\partial q}{\partial r} \right|_{r=0} = \frac{q_1 - q_2}{\Delta r} = 0 \quad (2.37)$$

where q_1 is the solid phase concentration at the center of a zeolite particle and q_2 is the solid phase concentration at a node located a radial distance Δr from the center. At surface of a zeolite particle, that is for $j=N+1$, the IX isotherm is used as the boundary condition. At node $j=N+2$, which represents the bulk concentration of $C_{NH_4^+}$, is given by:

$$\frac{C_{N+2}^{n+1} - C_{N+2}^n}{\Delta t} = -\frac{3D_s M}{RV} \left(\frac{q_{n+1} - q_n}{\Delta r} \right) \quad (2.38)$$

where M is the mass of chabazite in the bioreactor, V is the liquid volume, and R is the radius of a zeolite particle. The equations can be written in the form of an $(N+3) \times (N+3)$ matrix as follows:

$$\begin{bmatrix}
1 & -1 & 0 & 0 & 0 & 0 & 0 & \dots & 0 \\
\frac{\lambda}{j-1} - \lambda & 1+2\lambda & -\frac{\lambda}{j-1} - \lambda & 0 & 0 & 0 & 0 & \dots & 0 \\
0 & \frac{\lambda}{j-1} - \lambda & 1+2\lambda & -\frac{\lambda}{j-1} - \lambda & 0 & 0 & 0 & \dots & 0 \\
0 & 0 & \frac{\lambda}{j-1} - \lambda & 1+2\lambda & -\frac{\lambda}{j-1} - \lambda & 0 & 0 & \dots & 0 \\
\vdots & \vdots & \vdots & \vdots & \vdots & \vdots & \vdots & \vdots & \vdots \\
\vdots & \vdots & \vdots & \vdots & \vdots & \vdots & \vdots & \vdots & \vdots \\
\vdots & \vdots & \vdots & \vdots & \vdots & \vdots & \vdots & \vdots & \vdots \\
\vdots & \vdots & \vdots & \vdots & \vdots & 0 & 1 & 0 & 0 \\
\vdots & \vdots & \vdots & \vdots & \vdots & -\frac{3MD_s \Delta t}{RV \Delta r} & \frac{3MD_s \Delta t}{RV \Delta r} & 1 & 0 \\
\vdots & \vdots & \vdots & \vdots & \vdots & \vdots & 0 & 1 & 1
\end{bmatrix}
\begin{bmatrix}
q_1^{n+1} \\
q_2^{n+1} \\
q_3^{n+1} \\
q_4^{n+1} \\
\vdots \\
\vdots \\
\vdots \\
\vdots \\
q_{N+1}^{n+1} \\
C_{N+2}^{n+1} \\
A_{N+2}^{n+1}
\end{bmatrix}
= \begin{bmatrix}
0 \\
\left(\lambda - \frac{\lambda}{j-1} \right) q_1^n + (1-2\lambda) q_2^n + \left(\lambda + \frac{\lambda}{j-1} \right) q_3^n \\
\left(\lambda - \frac{\lambda}{j-1} \right) q_2^n + (1-2\lambda) q_3^n + \left(\lambda + \frac{\lambda}{j-1} \right) q_4^n \\
\left(\lambda - \frac{\lambda}{j-1} \right) q_3^n + (1-2\lambda) q_4^n + \left(\lambda + \frac{\lambda}{j-1} \right) q_5^n \\
\vdots \\
\vdots \\
\frac{QKC}{A + KC} \\
C_{N+2}^n \\
C_{initial}
\end{bmatrix}$$

Due to the non-linearity of the IX isotherm (Eq. 2.31), a predictor-corrector scheme was adopted to iterate through time and solve for the concentrations at a new time level.

2.5 References

Ahuja, S. Comprehensive Water Quality and Purification. Elsevier: Waltham, MA, USA, 2014.

Andrews, J. F. A mathematical model for the continuous culture of microorganisms utilizing inhibitory substrates. *Biotechnol. Bioeng.* **1968**, 10(6), 707-723.

Batchelor, B.; Lawrence, A. W. Autotrophic denitrification using elemental sulfur. *J. Water Pollut. Control Fed.* **1978**, 1986-2001.

Bu, S.; Huang, J. F.; Boyer, T. H.; Miller, C. T. An evaluation of solution algorithms and numerical approximation methods for modeling an ion exchange process. *J. Comput. Phys.* **2010**, 229(13), 4996–5010.

Crank, J.; Nicolson, P. A practical method for numerical evaluation of solutions of partial differential equations of the heat-conduction type. *Adv. Comput. Math* **1947**, 6, 207-226.

Daims, H.; Lebedeva, E. V.; Pjevac, P.; Han, P.; Herbold, C.; Albertsen, M.; Kirkegaard, R.H. Complete nitrification by *Nitrospira* bacteria. *Nature* **2015**, 528(7583), 504-509.

De Groot, W. T. Modelling the multiple nutrient limitation of algal growth. *Eco. Modelling* **1983**, 18(2), 99-119.

Eberl, H. J.; Parker, D. F.; van Loosdrecht, M. A new deterministic spatio-temporal continuum model for biofilm development. *Comput. Math. Meth. Medicine* **2001**, 3(3), 161-175.

Ebeling, J.M., Timmons M.B., Bisogni, J.J Engineering analysis of the stoichiometry of photoautotrophic, autotrophic, and heterotrophic removal of ammonia-nitrogen in aquaculture Systems. *Aquaculture* **2006**, 257:346–358.

FDOH Standards for Onsite Sewage Treatment and Disposal Systems, Chapter 64E-6, Florida Administrative Code. Florida Department of Health (FDOH), 2013.

Han, B. P.; Virtanen, M.; Koponen, J.; Straškraba, M. Effect of photoinhibition on algal photosynthesis: a dynamic model. *J. Plank. Res.* **2000**, 22(5), 865-885.

Hedström, A. Ion exchange of ammonium in zeolites: a literature review. *J. Env. Eng.* **2001**, 127(8), 673-681.

Helfferich, F. G. Ion exchange. Courier Dover Publications, 1962.

Hirst, J. E.; Anderson, D. L.; Smith, D. P. The Florida Onsite Sewage Nitrogen Reductions Strategies (FOSNRS) Study: Project Overview and Preliminary Results. Florida Water Resources Conference. April 29, 2013 at Orlando, Florida, 2013.

Karniadakis, G. E.; Kirby II, R. M. Parallel scientific computing in C++ and MPI: a seamless approach to parallel algorithms and their implementation. Cambridge University Press, 2003.

Kithome, M.; Paul, J. W.; Lavkulich, L.M; Bomke, A, A. Kinetics of ammonium adsorption and desorption by the natural zeolite clinoptilolite. *Soil Sci. Soc. America J.* **1998**, vol. 62, 3, 622–629.

Knutson, C. E.; Werth, C. J.; Valocchi, A. J. Pore-scale simulation of biomass growth along the transverse mixing zone of a model two-dimensional porous medium. *Water Res. Res.* **2005**, 41(7).

Kosaric N.; Nguyen H.T.; Bergougrou, M.A. Growth of *Spirulina maxima* algae in effluents from secondary waste-water treatment plants. *Biotechnol. Bioeng.* **1974**, 16 (7):881-896.

Krayzelova L.; Lynn T. J.; Banihani Q.; Bartacek J.; Jenicek P.; Ergas, S. J. A Tire-Sulfur Hybrid Adsorption Denitrification (T-SHAD) process for decentralized wastewater treatment. *Water Res.* **2014**, 61, 191-199.

Kreft, J. U.; Picioreanu, C.; Wimpenny, J. W.; van Loosdrecht, M. C. Individual-based modelling of biofilms. *Microbiology* **2001**, 147(11), 2897-2912.

Krishna, R.; Wesselingh, J. A. The Maxwell-Stefan approach to mass transfer. *Chem. Eng. Sci.* **1997**, 52(6), 861-911.

Kumar, A.; Ergas, S.; Yuan, X.; Sahu, A.; Zhang, Q.; Dewulf, J.; Van Langenhove, H. Enhanced CO₂ fixation and biofuel production via microalgae: recent developments and future directions. *Trends Biotechnol.* **2010**, 28(7), 371-380.

Lee, E.; Zhang, Q. Integrated co-limitation kinetic model for microalgae growth in anaerobically digested municipal sludge centrate. *Algal Res.* **2016**, 18, 15-24.

LeVeque, R. J. Finite difference methods for ordinary and partial differential equations: steady-state and time-dependent problems (Vol. 98). Society for Industrial and Applied Mathematics, 2007.

Lito, P. F.; Cardoso, S. P.; Loureiro, J. M.; Silva, C. M. Ion exchange equilibria and kinetics. In *Ion Exchange Technology I* (pp. 51-120). Springer Netherlands, 2012.

Lito, P. F.; Aniceto, J. P. S.; Silva, C. M. Modelling ion exchange kinetics in zeolite- type materials using Maxwell-Stefan approach. *Desalin. Water Treat.* **2014**, 52(28-30), 5333-5342.

Lopez-Ponnada, E. V.; Lynn, T. J.; Peterson, M.; Ergas, S. J.; Mihelcic, J. R. Application of denitrifying wood chip bioreactors for management of residential non-point sources of nitrogen. *J. Biol. Eng.* **2017**, 11(1), 16.

Lovley, D. R. Cleaning up with genomics: applying molecular biology to bioremediation. *Nat. Rev. Microbol.* **2003**, 1(1), 35.

Mellbye, B. L.; Giguere, A. T.; Murthy, G. S.; Bottomley, P. J.; Sayavedra-Soto, L. A.; Chaplen, F. W. Genome-Scale, Constraint-Based Modeling of Nitrogen Oxide Fluxes during Coculture of *Nitrosomonas europaea* and *Nitrobacter winogradskyi*. *MSystems* **2018**, 3(3), e00170-17.

Monod, J. The growth of bacterial cultures. *Annu. Rev. Microbiol.* **1949**, 3(1), 71-394.

Mori, H. Transport, collective motion, and Brownian motion. *Progress of theoretical Physics* **1965**, 33(3), 423-455.

Nazaroff, W.; L. Alvarez-Cohen. *Environ. Eng. Sci.* New York: John Wiley and Sons, 2001.

Ng, W. L.; Bassler, B. L. Bacterial quorum-sensing network architectures. *Annu. Rev. Genetics* **2009**, *43*, 197-222.

Oakley, S. M.; Gold, A. J.; Oczkowski, A. J. Nitrogen control through decentralized wastewater treatment: process performance and alternative management strategies. *Ecol. Eng.* **2010**, *36*(11), 1520-1531.

Paschek, D.; Krishna, R. Diffusion of binary mixtures in zeolites: kinetic Monte Carlo versus molecular dynamics simulations. *Langmuir* **2001**, *17*(1), 247-254.

Payra, P.; Dutta, P. K. Zeolites: a primer. Handbook of zeolite science and technology, 1-19, 2003.

Picioreanu, C.; Van Loosdrecht, M. C.; Heijnen, J. J. Effect of diffusive and convective substrate transport on biofilm structure formation: a two-dimensional modeling study. *Biotechnol. Bioeng.* **2000**, *69*(5), 504-515.

Picioreanu, C.; Kreft, J. U.; van Loosdrecht, M. C. Particle-based multidimensional multispecies biofilm model. *Appl. Environ. Microbiol.* **2004**, *70*(5), 3024-3040.

Prindle, A.; Liu, J.; Asally, M.; Ly, S.; Garcia-Ojalvo, J.; Süel, G. M. Ion channels enable electrical communication in bacterial communities. *Nature* **2015**, *527*(7576), 59-63.

Rittmann, B.; McCarty, P. Environmental biotechnology: Principles and applications. Boston: McGraw-Hill, 2001.

Sakar, S.; Yetilmezsoy, K.; Kocak, E. Anaerobic digestion technology in poultry and livestock waste treatment-a literature review. *Waste Manage. Res.* **2009**, *27*(1), 3-18.

Schipper, L. A.; Robertson, W. D.; Gold, A. J.; Jaynes, D. B.; Cameron, S. C. Denitrifying bioreactors-an approach for reducing nitrate loads to receiving waters. *Ecol. Eng.* **2010**, *36*(11), 1532-1543.

Sengupta, S.; Ergas, S. J.; Lopez-Luna, E. Investigation of solid-phase buffers for sulfur-oxidizing autotrophic denitrification. *Proceedings of the WaterEnvironment Federation* **2007**, *2*, 1139-1159.

Siegrist, R. L.; McCray, J. E.; Lowe, K. S.; Cath, T. Y.; Munakata-Marr, J. Onsite and Decentralised Wastewater Systems: Advances from a decade of research and educational efforts. *Water* **2013**, 77-84.

Silkin, V.; Chubchikova, I. Kinetics of uptake of phosphates and nitrates by marine multicellular algae, *Gelidium latifolium* (Grev.) *Born. et Thur. Biology Bulletin* **2007**, *34*(2):156-162.

Speitel Jr, G. E.; Dovantzis, K.; DiGiano, F. A. Mathematical modeling of bioregeneration in GAC columns. *J. Environ. Eng.* **1987**, *113*(1), 32-48.

Spijkerman; E., de Castro; F.E., Gaedke, U. Independent colimitation for carbon dioxide and inorganic phosphorus, *PLoS One* **2011**, 6 (12), e28219.

Tang, Y.; Valocchi, A. J.; Werth, C. J.; Liu, H. An improved pore-scale biofilm model and comparison with a microfluidic flow cell experiment. *Water Res. Res.* **2013**, 49(12), 8370-8382.

Wang, S.; Peng, Y. Natural zeolites as effective adsorbents in water and wastewater treatment. *Chem. Eng. J.* **2010**, 156(1), 11-24.

Wanner, O.; Gujer, W. A multispecies biofilm model. *Biotechnol. Bioeng.* **1986**, 28(3), 314-328.

Wanner, O.; Eberl, H.; Morgenroth, E.; Noguera, D; Picioreanu, C; Rittmann, B. E.; van Loosdrecht, M. C. M. Mathematical Modeling of Biofilms. Report of the IWA Biofilm Modeling Task Group, Scientific and Technical Report No. 18, IWA Publishing, London, 2006.

Wilde, E.W.; Benemann, J.R. Bioremoval of heavy-metals by the use of microalgae. *Biotechnol. Adv.* **1993**, 11 (4):781-812.

Zheng, H.; Han, L.; Ma, H.; Zheng, Y.; Zhang, H.; Liu, D.; Liang, S. Adsorption characteristics of ammonium ion by zeolite 13X. *J. Hazard. Mater.* **2008**, 158(2), 577-584.

CHAPTER 3:

BIOREGENERATION OF CHABAZITE DURING NITRIFICATION OF

ANAEROBICALLY DIGESTED CENTRATE: EXPERIMENTAL AND MODELING

STUDIES¹

3.1 Introduction

Livestock wastes contain high concentrations of solids, organic matter, nutrients, pathogens, and other compounds of concern, which can threaten surface and ground waters (Guan and Holley, 2003; Hatfield et al., 1998; Varel et al., 2012). Anaerobic digestion (AD) of livestock wastes stabilizes organic matter while producing methane, which can be used as a biofuel (Cantrell et al., 2008). However, AD effluents are rich in nutrients which often cannot be assimilated by nearby cropland, and further treatment by biological nitrification and denitrification may be needed (Massé et al., 2011). A challenge in the treatment of anaerobically digested swine waste (ADSW) centrate is inhibition of nitrification by high concentrations of free ammonia (FA). Concentrations of FA in ADSW centrate depend on total ammonia nitrogen (TAN) concentrations, pH, and temperature (Weiner, 2012) and range from 10 to 550 mg L⁻¹ (as N) (Boiran et al., 1996); such concentrations have been shown to be inhibitory to nitrifying bacteria (Anthonisen et al., 1976; Kim et al., 2008).

¹ “Adapted with permission from Aponte-Morales, V. E.; Payne, K. A.; Cunningham, J. A.; Ergas, S. J. Bioregeneration of Chabazite During Nitrification of Centrate from Anaerobically Digested Livestock Waste: Experimental and Modeling Studies. *Environ. Sci. Technol.* **2018**, 52(7), 4090-4098. Copyright 2018 American Chemical Society.”

A potential strategy for overcoming nitrification inhibition during treatment of high-TAN wastewaters is combining ion exchange (IX) with nitrification to suppress the concentration of ammonium (NH_4^+) and, hence, FA (Green et al., 1996; Jung et al., 2004). The most commonly used materials for cation exchange in wastewater treatment are natural zeolites, which are porous aluminosilicate minerals with high cation exchange capacities and high selectivity for NH_4^+ ions (Hedstrom, 2001). Clinoptilolite is the most commonly used zeolite due to its low cost; however, chabazite has a higher NH_4^+ exchange capacity (Langwaldt, 2008; Wang and Peng, 2010), which may be advantageous in applications where the zeolite is regenerated and reused.

Regeneration of ion-exchange zeolites is most often accomplished by exposing the saturated zeolite (Z-NH_4^+) to a concentrated sodium chloride (NaCl) or sodium bicarbonate (NaHCO_3) solution (Guo et al., 2013; Koon and Kaufman, 1975). However, the waste brine produced, which is high in both Na^+ and NH_4^+ , presents a disposal problem (Farag and Harper, 2014; Maas, 1993; Sanchez et al., 2004; Semmens and Porter, 1979). An alternative to waste brine disposal is treatment using salt-tolerant nitrifying bacteria, (Green et al., 1996; Semmens and Porter, 1979) allowing the treated brine to be reused for multiple cycles. However, this process requires salt addition, multiple reactors for adsorption, regeneration and brine treatment, and the need to use halophilic nitrifying bacteria (He et al., 2007; Wei et al., 2014).

To overcome these drawbacks, a novel method for IX-assisted nitrification with simultaneous direct bioregeneration of NH_4^+ -saturated chabazite has been recently demonstrated (Aponte-Morales et al., 2016). In this process, a small fraction of NH_4^+ is desorbed from the zeolite by exchange with cations present in the wastewater or with chemicals added to supplement alkalinity losses during nitrification. Nitrifying bacteria oxidize NH_4^+ in solution, and desorption continues until the solution NH_4^+ concentration decreases to negligible values. A proposed major

advantage of this approach is that the chabazite dose can be set so that concentration of FA in solution remains below the inhibitory concentration for nitrification. In addition, there is no waste brine produced, the use of halophilic nitrifying bacteria is not necessary, and the process can be carried out in a single reactor.

This process of IX-assisted nitrification and bioregeneration was previously demonstrated using chabazite in a sequencing batch reactor (Zeo-SBR) that included both aerobic and anoxic phases (Aponte-Morales et al., 2016). The process was successful at removing nitrogen from ADSW; however, the beneficial effect of the chabazite towards reducing FA inhibition of nitrification was not quantified or verified experimentally. Furthermore, a mathematical framework had not be previously developed to quantitatively describe the physicochemical and biological processes involved. Such a mathematical model, along with a numerical implementation to solve the governing equations, would represent a useful tool for designing or engineering IX-assisted biological treatment processes.

Therefore, the overall goal of this Chapter is to develop the theoretical foundation of the novel IX-assisted nitrification/bioregeneration process described above. The guiding hypotheses are (i) that chabazite addition can increase the nitrification rate by easing FA inhibition, (ii) that nitrifying bacteria can directly bioregenerate chabazite loaded with NH_4^+ , allowing for its reuse, and (iii) that appropriate models of IX equilibrium and kinetics, combined with a kinetic model of FA-inhibited nitrification, can provide an accurate quantitative description of the overall process. The specific objectives of this Chapter are to (1) determine the effectiveness of chabazite addition for reducing FA inhibition of nitrification, (2) develop a mathematical model that describes the process, accounting for simultaneous IX and FA-inhibited nitrification, and (3) assess the model's ability to predict experimental results without the use of "fitting parameters." Accomplishment of

these objectives will facilitate the improved design of environmental biotechnologies that utilize zeolites and nitrification processes for treatment of high-ammonium-strength wastewaters.

3.2 Materials and Methods

3.2.1 Anaerobically Digested Swine Waste Centrate

A pilot-scale anaerobic digester managed in our laboratory as a semi-continuous batch reactor with a working volume of 26 L supplied the ADSW centrate for this study. The reactor was operated at a ~20-day solids retention time (SRT) by feeding 2.6 L of swine manure collected from a local farm three times per week. Additional details on pilot reactor operation can be found elsewhere (Amini et al., 2017). ADSW centrate (Table 1) was obtained by centrifuging the effluent from the reactor at 4000 rpm for 15 min in a Thermo scientific Sorvall Legend RT Plus centrifuge (Waltham, MA). In addition, two synthetic wastewaters were used in the experiments: 1) SYN-1 (Table 1) was formulated to contain NH_4^+ and cations at concentrations similar to those of real centrate and contained (g L^{-1}) NH_4Cl (3.8), NaHCO_3 (2.0), K_2HPO_4 (0.4), NaCl (1.9), KCl (0.9), $\text{MgCl}_2 \cdot 6\text{H}_2\text{O}$ (2.0) and $\text{CaCl}_2 \cdot \text{H}_2\text{O}$ (2.4) in deionized (DI) water; 2) SYN-2 was used in the nitrification inhibition studies and consisted of DI water with $2.0 \text{ g L}^{-1} \text{ NaHCO}_3$, $0.4 \text{ g L}^{-1} \text{ K}_2\text{HPO}_4$, and varying concentrations of $\text{NH}_4^+\text{-N}$ ($0.06\text{--}3.8 \text{ g L}^{-1}$).

3.2.2 Chabazite

Chabazite (ZS500H) was obtained from St. Cloud™ Zeolite (Winston, New Mexico). Chabazite was sieved to obtain a particle size range of 1–2 mm, washed with DI water to remove residual powder, and dried at 100°C for 24 h. The dry chabazite was pretreated by soaking in local groundwater for 3 h with shaking, rinsed with DI water, and dried at 100°C for 24 h. St. Cloud™ Zeolite data sheet provided a characterization of chabazite indicating that sodium is the main cation loaded.

3.2.3 Ion Exchange Studies

Batch IX tests were performed in duplicate using USEPA protocols (USEPA, 2008; Roy and Roulier, 1991) to determine equilibrium and kinetic IX parameters. For equilibrium studies, varying masses of chabazite (0, 2.5, 3.75, 5, 10, 20, and 30 g) were placed in contact with a fixed volume (200 mL) of ADSW centrate ($806 \pm 145 \text{ mg-N L}^{-1}$) in 250-mL Erlenmeyer flasks. The flasks were covered with parafilm and maintained at 22°C for 48 h on a shaker table at 170 rpm. After 48 h samples were collected and analyzed for anion and cation concentrations as described below. The concentration of NH_4^+ adsorbed to the chabazite (meq NH_4^+ per g chabazite) was calculated based on the difference between the initial and final aqueous NH_4^+ concentrations, assuming other loss mechanisms were negligible.

IX kinetics were determined in similar systems using ADSW and a chabazite dose of 150 g L^{-1} . The initial aqueous concentration of NH_4^+ was $914 \pm 7 \text{ mg-N L}^{-1}$ and the initial aqueous concentration of Na^+ was $330 \pm 2 \text{ mg L}^{-1}$. Samples were collected at 0.5, 1, 1.5, 2, 3, 4, 10, 15, 20, and 24 h, and analyzed for anion and cation concentrations as described below.

3.2.4 Batch Nitrification Studies

Nitrification inhibition studies were carried out to quantify how NH_4^+ concentration affects the rate of nitrification. Tests were conducted in six 1-L beakers containing 600 mL of seed sludge with a volatile suspended solids (VSS) concentration between $5.4\text{--}5.5 \text{ g L}^{-1}$. Synthetic wastewater consisted of SYN-2 with varying $\text{NH}_4^+\text{-N}$ concentrations (50, 100, 200, 350, 500, and 1000 mg L^{-1}) and a pH of 7.5. Seed sludge consisted of mixed liquor obtained from a municipal wastewater treatment plant (Northwest Regional Water Reclamation Facility, Hillsborough County, FL) that uses a 5-stage Bardenpho process for biological nutrient removal. Mixing was provided at 100 rpm using a Phipps & Bird PB-700™ Jartester (Richmond, VA) at room temperature. Aeration was supplied with Whisper Tetra air pumps (St. Blacksburg, VA) and diffuser stones to maintain

dissolved oxygen (DO) concentrations above 6 mg L⁻¹. Additional batch nitrification tests were performed with SYN-2 at an NH₄⁺-N concentration of 100 mg L⁻¹ with and without 2,000 mg L⁻¹ of Na⁺ added to determine the impact of high Na⁺ concentrations on nitrification. Samples were collected every two hours for 16 hours and analyzed for anion and cation concentrations as described below.

3.2.5 Chabazite-Amended Nitrification Studies

Batch nitrification studies were also performed to determine the effectiveness of chabazite in improving the nitrification rate during the treatment of high-strength wastewater. Six reactors were set up as described in the previous nitrification inhibition section. R1, R2, and R3 were operated without the addition of chabazite, whereas R4, R5, and R6 were amended with a pretreated chabazite at a dose of 150 g L⁻¹. All reactors were operated with SYN-1 (Table 3.1) and a MLSS concentration of 3 g L⁻¹. Samples were collected daily over eight days and analyzed for anion and cation concentrations as described below.

Table 3.1: Characterization of anaerobically digested swine waste centrate

Parameter	Unit	ADSW centrate	SYN-1
NH ₄ ⁺	mg-N L ⁻¹	861 ± 99	1,000
Na ⁺	mg L ⁻¹	275 ± 85	700
K ⁺	mg L ⁻¹	693 ± 211	450
Ca ²⁺	mg L ⁻¹	373 ± 62	660
Mg ²⁺	mg L ⁻¹	136 ± 27	240
PO ₄ ³⁻	mg-P L ⁻¹	58 ± 9	70
pH		7.28 ± 0.20	7.5
Alkalinity	CaCO ₃ mg L ⁻¹	3,100 ± 114	2,000
sCOD	mg L ⁻¹	1,900 ± 220	---

3.2.6 Analytical Methods

Concentrations of cations (NH_4^+ , Ca^{2+} , Mg^{2+} , Na^+ , K^+) and anions (NO_3^- , NO_2^-) were measured using a Metrohm 881 Compact Ion Chromatography (IC) Pro system (Metrohm Inc., Switzerland) using IC Application No. C-115 and No. S-236. Detection limits using this method were 0.20, 0.01, 0.07, 0.27, 0.20, 18.50, and 0.09 mg L^{-1} for NO_2^- -N, NO_3^- -N, NH_4^+ -N, Ca^{2+} , Mg^{2+} , Na^+ , and K^+ , respectively. Standard Methods (APHA, 2012) were used to measure: DO (4500-O), VSS (2540), pH (4500-H), alkalinity (2320), conductivity (2510), and soluble chemical oxygen demand (sCOD; 5220). Due to high Cl^- peaks (which interfere with anion chromatography) during the chabazite-amended nitrification studies, NO_2^- was measured using Standard Method 4500 (APHA, 2012) and NO_3^- was measured using the Resorcinol Method (Zhang and Fischer, 2006). Detection limits for NO_2^- -N and NO_3^- -N by these methods were 0.01 and 0.21 mg L^{-1} , respectively.

3.2.7 Data Analysis

All experiments were performed in duplicate except for the chabazite-amended nitrification studies, which were performed in triplicate. Values in tables and figures are presented as means with max/min values. Student's t-tests were used to determine if two sets of data were significantly different from each other. The test was performed at a confidence level of 95%, rejecting the null hypothesis (no difference between data sets) if $p < 0.05$.

Nitritation rates ($\text{mg-N L}^{-1} \text{ h}^{-1}$) were calculated as the negative slope of a graph of NH_4^+ -N concentrations versus time. Nitrataion rates ($\text{mg-N L}^{-1} \text{ h}^{-1}$) were calculated as the positive slope of a graph of NO_3^- -N concentrations versus time. Slopes were calculated by performing linear regression on the data points between 2 and 10 h. Specific nitritation and nitrataion rates ($\text{mg-N h}^{-1} \text{ mg-VSS}^{-1}$) were calculated by dividing the calculated rate by the VSS concentration.

The percent bioregeneration of the chabazite was calculated by dividing the final soluble total nitrogen (TN) concentration in aqueous solution by the initial soluble TN concentration in aqueous solution.

3.3 Mathematical Model Development

We developed a mathematical model to describe the underlying physico-chemical and biological processes occurring within the bioreactors. A conceptualization of the main mechanisms within the bioreactors is shown in Figure 3.1. The species accounted for in the aqueous phase are NH_4^+ , NO_2^- , NO_3^- , and Na^+ ; the adsorbed NH_4^+ concentration was predicted in the solid phase. In the bulk liquid, the mechanisms affecting the NH_4^+ concentration are IX and biological nitrification. The overall mass balance for NH_4^+ in the bulk liquid is given by:

$$\frac{dC_{\text{NH}_4^+}}{dt} = \frac{J_{\text{NH}_4^+} A}{V} - r_s \quad (3.1)$$

where A (m^2) is the interfacial area of the zeolite particles, V (L) is the volume of the liquid, $C_{\text{NH}_4^+}$ (meq L^{-1}) is the NH_4^+ concentration in the aqueous phase, $J_{\text{NH}_4^+}$ ($\text{meq m}^{-2} \text{h}^{-1}$) is the flux of NH_4^+ ions between the bulk liquid and chabazite, r_s is the rate of substrate utilization ($\text{meq L}^{-1} \text{h}^{-1}$), and t (h) is time.

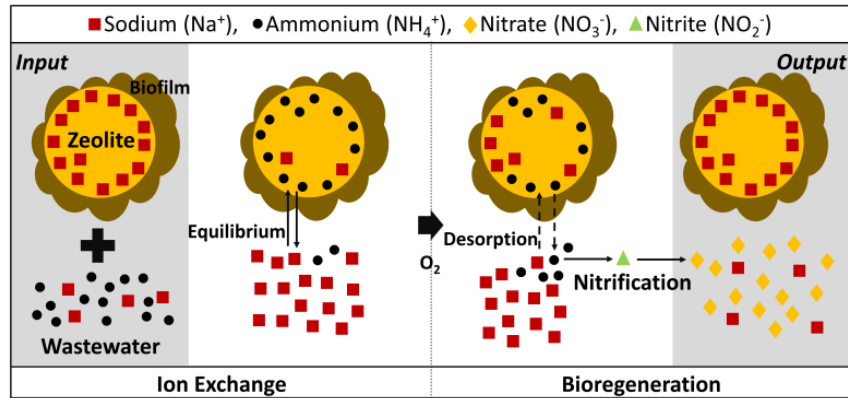


Figure 3.1: Conceptualization of the IX and bioregeneration processes occurring within the bioreactors for NH_4^+ -N removal

The diffusion of ions in zeolitic materials is dominated by surface diffusion, in which mass transport is characterized by probabilistically rare jumps between cages that host ions (Aponte-Morales, 2015). Kinetic models that have been applied to surface diffusion include semi-empirical, Fickian-based, Nernst-Planck, and Maxwell-Stefan models (USEPA, 2008). An approach that strikes a balance between simplicity and accuracy is the homogeneous surface diffusion model (HSDM). This model assumes the IX material is homogeneous and spherical, and that diffusion is Fickian, so that the flux from the bulk liquid into the IX grains is given by:

$$J_{NH_4^+} = -\rho D_s \left. \frac{\partial q_{NH_4^+}}{\partial r} \right|_{r=R} \quad (3.2)$$

where ρ (g m^{-3}) is the density of the chabazite particles, D_s ($\text{m}^2 \text{h}^{-1}$) is the surface diffusivity, r (m) is the radial coordinate within the solid material, $q_{NH_4^+}$ (meq g^{-1}) is the solid-phase NH_4^+ concentration, and R (m) is the radius of a chabazite particle. The mass balance for NH_4^+ in the solid phase based on the HSDM is given by:

$$\frac{\partial q_{NH_4^+}}{\partial t} = \frac{D_s}{r^2} \frac{\partial}{\partial r} \left(r^2 \frac{\partial q_{NH_4^+}}{\partial r} \right) \quad (3.3)$$

The following equations provide the initial and boundary conditions for the adsorbed (intra-zeolite) concentration:

$$q_{NH_4^+}(t=0, r) = 0 \quad (3.4)$$

$$\frac{\partial q_{NH_4^+}}{\partial r}(r=0, t) = 0 \quad (3.5)$$

$$q_{NH_4^+}(r=R, t) = \frac{QKC_{NH_4^+}}{C_{Na^+} + KC_{NH_4^+}} \quad (3.6)$$

where C_{Na^+} is the aqueous-phase concentration (meq L⁻¹) of Na⁺, Q is the maximum IX capacity (meq g⁻¹) of the chabazite, and K is the selectivity coefficient (dimensionless), which is related to the ionic affinity for the zeolite (Roy and Roulier, 1991). Equation 3.6 is based on the assumption that, at the surface of the zeolite, the aqueous-phase and sorbed-phase concentrations of NH₄⁺ are in equilibrium.

For high-NH₄⁺-strength wastewater, ammonia-oxidizing bacteria (AOB) and nitrite-oxidizing bacteria (NOB) can be inhibited by their own substrates (APHA, 2012). A suitable model for explaining microbial kinetics when microbes are exposed to inhibitory substrates is the Andrews equation (APHA, 2012). Assuming an inhibitory effect due to a high NH₄⁺ concentration, the rate of substrate utilization for AOB and NOB in Equation 3.1 is written as:

$$r_s = r_{AOB} = \frac{\mu_{\max,AOB} C_{NH_4^+} X_{AOB}}{Y_{AOB} \left(\frac{C_{NH_4^+}^2}{K_{I,AOB}} + K_{S,NH_4^+} + C_{NH_4^+} \right)} \quad (3.7)$$

$$r_{NOB} = \frac{\mu_{\max,NOB} C_{NO_2^-} X_{NOB}}{Y_{NOB} \left(\frac{C_{NH_4^+}^2}{K_{I,NOB}} + K_{S,NO_2^-} + C_{NO_2^-} \right)} \quad (3.8)$$

where $\mu_{\max,AOB}$ (h⁻¹) is the maximum specific growth rate of AOB, $\mu_{\max,NOB}$ (h⁻¹) is the maximum specific growth rate of NOB, X_{AOB} (mgVSS L⁻¹) is the AOB biomass concentration, X_{NOB} (mgVSS L⁻¹) is the NOB biomass concentration, Y_{AOB} is the AOB yield coefficient, Y_{NOB} is the NOB yield coefficient, K_{S,NH_4^+} (meq L⁻¹) is the half-saturation constant for AOB, K_{S,NO_2^-} (meq L⁻¹) is the half-saturation constant for NOB, $K_{I,AOB}$ (mg L⁻¹) is the inhibition coefficient for AOB, and $K_{I,NOB}$ (meq L⁻¹) is the inhibition coefficient for NOB. Since chabazite is a cation exchanger under the experimental conditions maintained in the bioreactor (neutral pH), the affinity for the anionic

species (NO_3^- and NO_2^-) can be ignored. Assuming the sequential nitrification reactions are inhibited by the presence of high NH_4^+ concentrations, mass balances for NO_2^- and NO_3^- in the reactor are expressed as:

$$\frac{dC_{\text{NO}_2^-}}{dt} = \frac{\mu_{\max, AOB} C_{\text{NH}_4^+} X_{AOB}}{Y_{AOB} \left(\frac{C_{\text{NH}_4^+}^2}{K_{I, AOB}} + K_{S, \text{NH}_4^+} + C_{\text{NH}_4^+} \right)} - \frac{\mu_{\max, NOB} C_{\text{NO}_2^-} X_{NOB}}{Y_{NOB} \left(\frac{C_{\text{NH}_4^+}^2}{K_{I, NOB}} + K_{S, \text{NO}_2^-} + C_{\text{NO}_2^-} \right)} \quad (3.9)$$

$$\frac{dC_{\text{NO}_3^-}}{dt} = \frac{\mu_{\max, NOB} C_{\text{NO}_2^-} X_{NOB}}{Y_{NOB} \left(\frac{C_{\text{NH}_4^+}^2}{K_{I, NOB}} + K_{S, \text{NO}_2^-} + C_{\text{NO}_2^-} \right)} \quad (3.10)$$

Substitution of Equations 3.2 and 3.7 into the mass balance expression (Equation 3.1) yields the following equation for simulating the temporal evolution of NH_4^+ during the IX-assisted nitrification process:

$$\frac{dC_{\text{NH}_4^+}}{dt} = -\frac{3M}{RV} D_s \frac{\partial q_{\text{NH}_4^+}}{\partial r} \bigg|_{r=R} - \frac{\mu_{\max, AOB} C_{\text{NH}_4^+} X_{AOB}}{Y_{AOB} \left(\frac{C_{\text{NH}_4^+}^2}{K_{I, AOB}} + K_{S, \text{NH}_4^+} + C_{\text{NH}_4^+} \right)} \quad (3.11)$$

where M (g) is the mass of chabazite in the bioreactor.

Finally, the aqueous concentration of sodium, C_{Na^+} , can be modeled by assuming that 1 meq of Na^+ is released from the chabazite for each 1 meq of NH_4^+ that is adsorbed onto the zeolite. To determine the mass of NH_4^+ sorbed onto chabazite, a numerical integration is required, as discussed in the Supporting Information (SI).

To predict the concentrations of NH_4^+ , NO_2^- , NO_3^- , and Na^+ in the reactor, Equations (3.3), (3.9), (3.10), and (3.11) must be solved simultaneously, subject to the initial and boundary conditions (3.4)–(3.6). The numerical approach used to solve these equations is described in the

SI. The SI also includes initial conditions for the aqueous concentrations of NH_4^+ , NO_2^- , NO_3^- , and Na^+ ; these are omitted here in the interest of space.

3.4 Results and Discussion

3.4.1 Ion Exchange Studies: Equilibrium and Kinetics

Results of the equilibrium IX studies are shown in Figure 3.2. The IX isotherm model (Equation 3.6) was fit to the experimental data and is shown in Figure 3.2 A. The isotherm constants, Q and K , were determined by linearizing the non-linear isotherm and finding the best-fit values using linear regression. The correlation coefficient (R^2) obtained was 0.987. The value of Q , which is the maximum IX capacity, was estimated to be 1.81 meq g^{-1} , which is about 32% lower than the value of 2.67 meq g^{-1} reported in previous studies (Kim et al., 2008; Zhang and Fischer, 2006). We suspect that this moderate difference is due to the natural variability of mineral composition within different chabazite deposits (Sawyer et al., 1994). The value of K obtained was found to be 2.92. The K parameter is a selectivity coefficient, indicative of the preference of one ion (NH_4^+) relative to another (Na^+) for exchange onto IX sites in chabazite (Crittenden et al., 2012). There are no prior published studies of the use of this model in this application to compare with our results. The efficiency of NH_4^+ removal as a function of chabazite dose is shown in Figure 3.2B. A chabazite dose of 150 g L^{-1} resulted in a removal efficiency of 88%, which was sufficient to reduce the NH_4^+ concentration below the inhibitory level, as will be discussed subsequently.

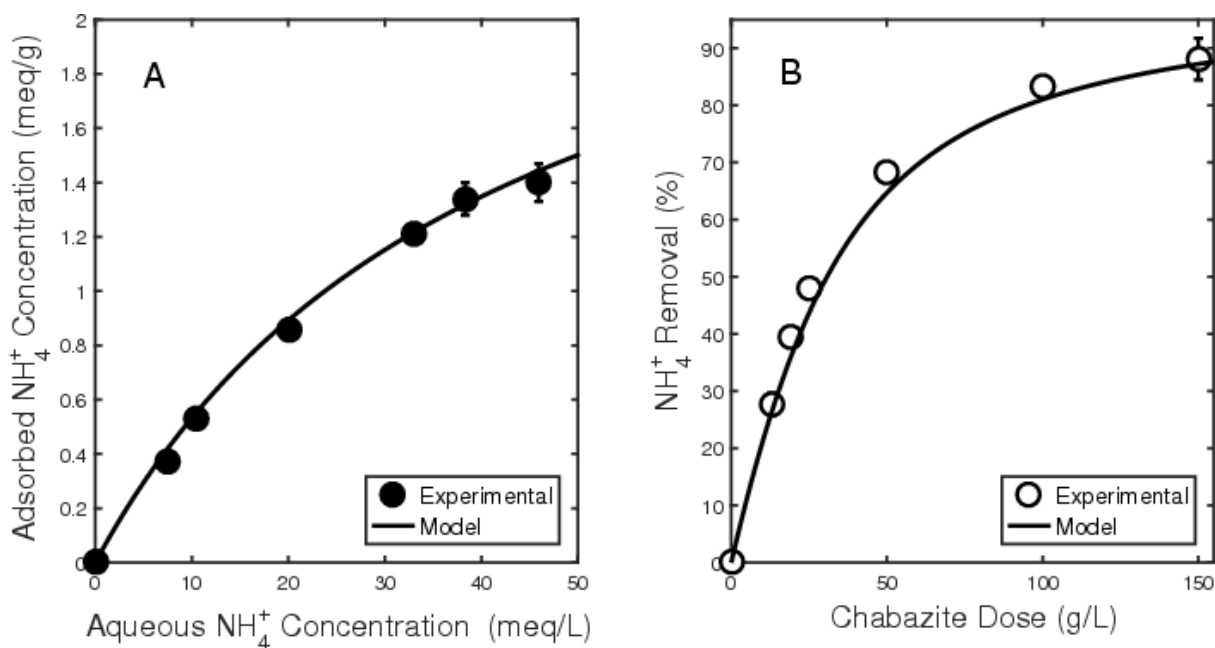


Figure 3.2: Ion exchange equilibrium: (A) IX isotherm model for NH_4^+ uptake; (B) Effect of chabazite dose on the observed removal efficiency of NH_4^+

The results of the IX kinetic study performed at a chabazite dose of 150 g L^{-1} over 24 h are shown in Figure 3.3. Most of the NH_4^+ adsorption occurred within the first four hours of contact. A finite-difference implementation of the HSDM (Equation 3.3), subject to the initial and boundary conditions Equations (4) –(6) for the solid phase, and initial conditions for the aqueous concentrations of NH_4^+ and Na^+ (see Supporting Information) was used to simulate the IX kinetics. The model was used to predict the rates of NH_4^+ uptake onto and Na^+ release from chabazite. The surface diffusion coefficient, D_s , was the only adjustable parameter in the numerical model. A value of $5.6 \times 10^{-13} \text{ m}^2 \text{ s}^{-1}$ was found to provide a good fit between the experimental data and surface diffusion model (Figure 3.3).

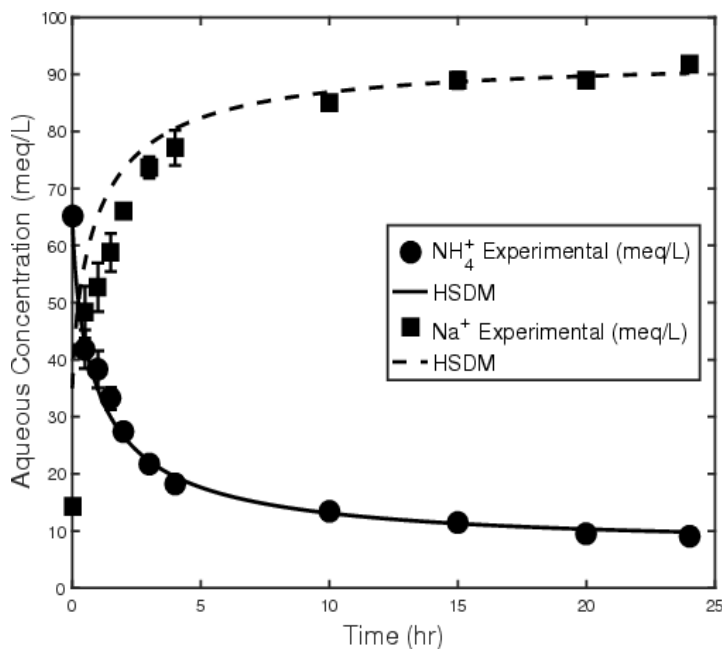


Figure 3.3: IX kinetics for NH_4^+ uptake onto chabazite and release of counterion Na^+

Although there are no reported literature values of surface diffusion coefficients for the zeolite used in this study, reported diffusion coefficients for NH_4^+ in zeolites range from $6.8 \times 10^{-12} \text{ m}^2 \text{ s}^{-1}$ to $4.2 \times 10^{-11} \text{ m}^2 \text{ s}^{-1}$ (Lahav and Green, 2000). Factors that affect the rate of diffusion in zeolites include shape selectivity, particle and pore size (Smit and Maesen, 2008). A comparative study of sorption kinetic models of NH_4^+ adsorption onto zeolites showed that the rate of uptake decreased when the particle size increased from 1.0 to 3.2 mm to 8.0–15 mm (Wen et al., 2006). The value obtained here was an order of magnitude lower than the previously observed range of surface diffusivities, which could be due to the effect of particle size or pore topology of chabazite particles used in the study. The HSDM provided an excellent explanation for the kinetics of uptake and release of NH_4^+ and Na^+ . While the HSDM does not account for electrostatic interactions, a major advantage of the HSDM for modeling surface diffusion kinetics over approaches such as the Maxwell-Stefan (MS) model is that it obviates the need to calibrate for parameters that are not widely documented. The slight discrepancy between the predicted and experimental Na^+

concentrations in the first five hours of the IX kinetic experiment was possibly due to presence of K^+ ions, which were not accounted for in the model. Based on the experimental data (Aponte-Morales, 2015), during IX both NH_4^+ and K^+ were adsorbed and Na^+ was the main cation desorbed.

3.4.2 Nitrification Inhibition Studies

Nitrification is a two-step process of nitrification (oxidation of NH_4^+ to NO_2^-) followed by nitrification (oxidation of NO_2^- to NO_3^-); both steps can be inhibited by the presence of FA (Kim et al., 2008). The effect of NH_4^+ concentration on the rate of initial NH_4^+ and NO_2^- oxidation is shown in Figure 3.4. During nitrification, as the NH_4^+ concentration increases, the NH_4^+ oxidation rate increases up to a maximum rate of $0.87 (\pm 0.21) \text{ mg-N g-VSS}^{-1} \text{ h}^{-1}$ at a TAN concentration of 100 mg-N L^{-1} ($FA = 1.47 \text{ mg-N L}^{-1}$). At higher concentrations of NH_4^+ , the rate is inhibited, although the effect is weak. During nitrification, as the NH_4^+ concentration increases, the NO_2^- oxidation rate increases up to a maximum rate of $0.66 (\pm 0.06) \text{ mg-N g-VSS}^{-1} \text{ h}^{-1}$ at a TAN concentration of 50 mg-N L^{-1} ($FA = 0.74 \text{ mg-N L}^{-1}$). At higher concentrations of NH_4^+ , the rate of nitrification is strongly inhibited. The observation that NOB are inhibited at lower concentrations of NH_4^+ than AOB is consistent with previous studies, which have shown that AOB are inhibited in the range of $10\text{--}150 \text{ mg NH}_3\text{-N L}^{-1}$ whereas NOB are inhibited at concentrations as low as $0.1\text{--}1.0 \text{ mg NH}_3\text{-N L}^{-1}$ (Kim et al, 2008; Green et al., 1996; Carrera et al., 2004).

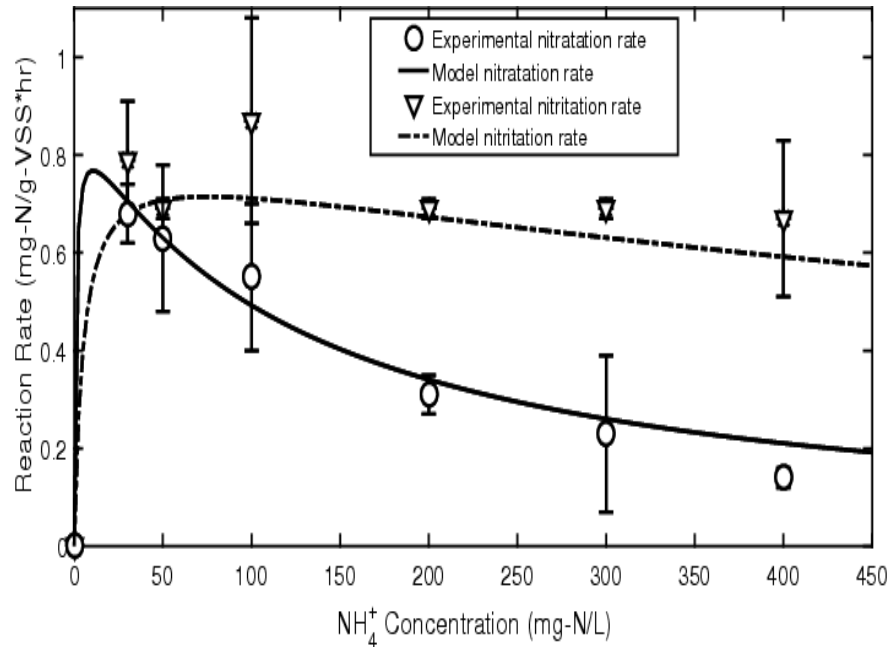


Figure 3.4: Nitrification inhibition: Effect of $\text{NH}_4^+\text{-N}$ concentration on nitrification and nitrataion reaction rate

Data from inhibition experiments were fit using the Andrews model, which resulted in a moderately good fit to the experimental data for both nitrification steps, as shown in Figure 3.4. The K_s value for the nitrification and nitrataion steps were set to 5.0 and 0.9 mg-N L⁻¹, respectively, based on prior literature (Leyva-Ramos et al., 2010). The data could then be used to find best-fit values of the inhibition coefficient, K_I , and the maximum rate of substrate utilization, $\mu_{\max}X/Y$ (see Equations (3.7) and (3.8)). The calibrated K_I values for AOB and NOB were found to be 1,120 mg-N L⁻¹ and 120 mg-N L⁻¹, respectively.

Results of the IX studies (Figures 3.2 and 3.3) showed that a chabazite doze of 150 g L⁻¹ can reduce the concentration of $\text{NH}_4^+\text{-N}$ in ADSW from around 800–900 mg L⁻¹ to below 150 mg L⁻¹ in a few hours. This suggests that adding such a dose of chabazite to the ADSW during nitrification may reduce the NH_4^+ concentration to a level that is only weakly inhibitory and may therefore increase the overall rate of nitrification.

3.4.3 Chabazite-Assisted Nitrification

The fates of NH_4^+ , NO_2^- and NO_3^- over an eight-day nitrification study with high NH_4^+ strength synthetic wastewater (SYN-2; $1,000 \text{ mg-N L}^{-1}$ of NH_4^+), without and with chabazite addition, are shown in Figures 3.5 and 3.6. Results from the bioreactors without chabazite addition (Figure 3.5) were consistent with our previous findings in the nitrification inhibition studies, where the presence of the inhibitory substrate, NH_4^+ , led to a relatively low NH_4^+ oxidation rate. In fact, the NH_4^+ concentration decreased by only 13% over the 8-d study period. Also, because NOB are more strongly inhibited than AOB by the presence of TAN (Figure 3.4), it was observed that NO_2^- accumulated during the experiment: the concentration of NO_2^- increased from 4.5 mg-N L^{-1} to 82 mg-N L^{-1} , but there was essentially no formation of NO_3^- (Figure 3.5B).

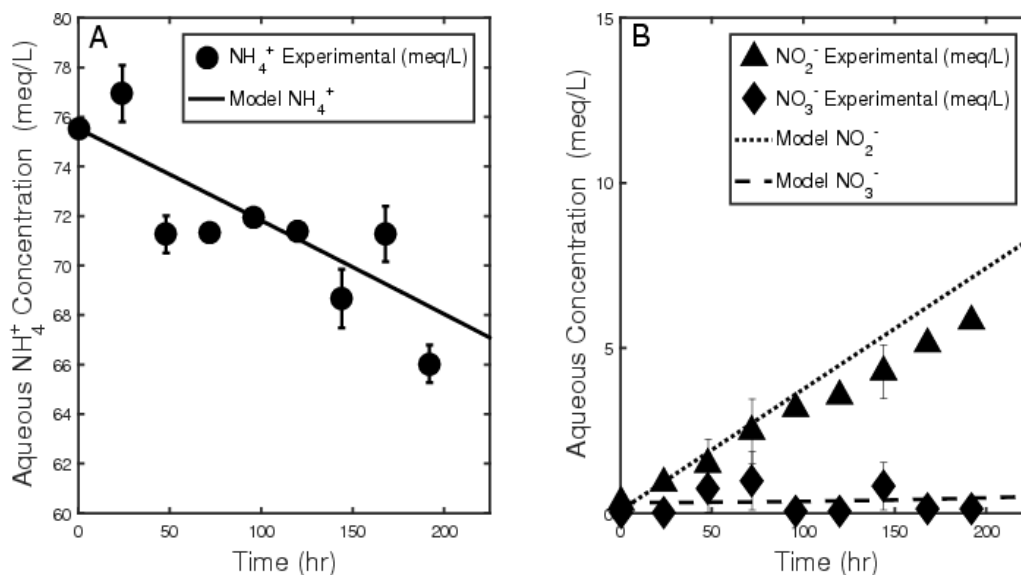


Figure 3.5: Nitrification without chabazite addition: (A) NH_4^+ concentration history over time, (B) NO_2^- and NO_3^- concentration histories over time

Figure 3.6A shows NH_4^+ and Na^+ concentrations as a function of time in the chabazite-amended reactors. The experimental data show a decrease in the NH_4^+ concentration by 87% over

the first 24 hours of the experiment, after which concentrations remained below the inhibitory level for nitrification. Moreover, the data show an increase in the nitrification rate in the chabazite-amended reactor, as evidenced by an increase in NO_3^- production (Figure 3.6B) from an initial concentration of 3.7 mg-N L^{-1} to 160 mg-N L^{-1} . This increase in the NO_3^- concentration by $\sim 155 \text{ mg-N L}^{-1}$ in the reactor with chabazite, compared to an increase by only $\sim 10 \text{ mg-N L}^{-1}$ in the reactor without chabazite. Comparison of Figure 3.5 and 3.6 supports the Chapter's hypothesis that addition of an appropriate dose of chabazite moderates the inhibitory effect of FA, and therefore leads to a faster rate of nitrification.

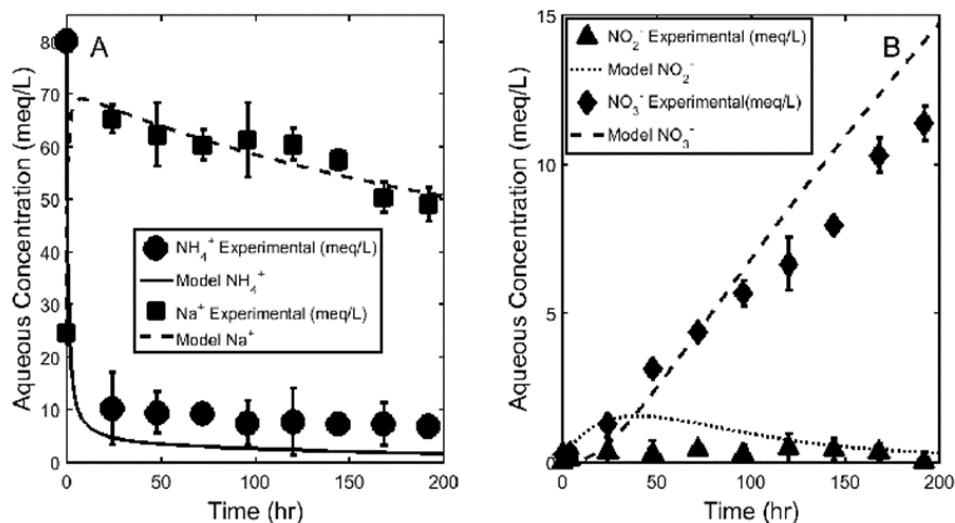


Figure 3.6: Nitrification with chabazite addition: (A) Simulated and experimental ammonium and sodium concentration during nitrification of $1,000 \text{ mg NH}_4^+\text{-N L}^{-1}$ (B) Simulated and experimental nitrite and nitrate production during nitrification of $1,000 \text{ mg NH}_4^+\text{-N L}^{-1}$

3.4.4 Assessment of Mathematical Model

Goals of this Chapter include the development and assessment of a mathematical model that can describe simultaneous IX and FA-inhibited nitrification without the use of “fitting parameters.” To achieve these goals, the model was calibrated incrementally in three stages, then tested on the data in Figures 3.5 and 3.6.

First, the equilibrium isotherm data (Figure 3.2) were used to determine the optimum values of the maximum IX capacity, Q , and selectivity coefficient, K . Second, once the isotherm parameters were determined, the HSDM was calibrated to experimental IX kinetic data (Figure 3.3) to determine the surface diffusion coefficient, D_s . Third, parameters for the biological component of the mathematical model were determined by calibrating the Andrews equation to the results shown in Figure 3.3. The biological parameters calibrated were the inhibition coefficient, K_I , and the factor $\mu_{\max}X/Y$, which can be thought of as an effective rate coefficient. These parameters were determined for both AOB and NOB (Figure 3.4).

Each of these three calibration steps was performed on a simplified system that included only a sub-set of the overall IX-assisted nitrification process. Finally, the overall model was tested by application to the full nitrification process, both without chabazite addition (Figure 3.5) and with chabazite addition (Figure 3.6). For these simulations, the model used the parameters obtained during the calibration steps, i.e., no additional fitting parameters were used. The parameters used for all simulations are provided in Table 3.2 in the SI.

Examination of Figures 3.5 and 3.6 shows that the model is able to accurately predict the concentrations of all tracked species (NH_4^+ , Na^+ , NO_2^- , NO_3^-) in either the presence or absence of chabazite. The excellent performance of the model strongly suggests that the mathematical equations used are a sufficient representation of the true underlying physics, chemistry, and

biology. In other words, the mathematical model presented herein provides a theoretically sound conceptual understanding of the IX-assisted nitrification process. Furthermore, it appears that estimates of model parameters (e.g., Q , K) obtained from a simplified experiment (e.g., equilibrium adsorption) remain valid during the full IX-assisted nitrification process.

Despite the excellent performance of the model, there are minor discrepancies between the model predictions and the experimental observations, which may indicate some limitations to the model. For instance, predicted rates of NH_4^+ removal and NO_3^- production are slightly faster than the observed rates (Figure 3.6). A possible explanation is that the model assumes that no biofilm growth occurred over the study period, and no hydrodynamic boundary layer exists. However, growth of nitrifying biofilms on the chabazite surface would lead to increased mass transfer resistance, thereby retarding the rate of ionic flux between the bulk liquid and the solid phase, which has been suggested by other authors (Picioreanu, 2004).

An additional factor that may affect the model performance is nitrification inhibition due to Na^+ ions released from the chabazite (Sanchez et al., 2004). Batch nitrification studies were conducted in synthetic wastewater (SYN-2) with $100 \text{ mg L}^{-1} \text{ NH}_4^+\text{-N}$, with and without $2,000 \text{ mg L}^{-1}$ of added Na^+ (Aponte-Morales). These values were selected based on typical NH_4^+ and Na^+ concentrations observed after IX of $1,000 \text{ mg-N L}^{-1} \text{ NH}_4^+$. The nitrification rate was observed to decrease from $1.19 \text{ mg-N (g-VSS)}^{-1} \text{ h}^{-1}$ in batch reactors without added Na^+ to $0.45 \text{ mg-N (g-VSS)}^{-1} \text{ h}^{-1}$ in the presence of $2,000 \text{ mg L}^{-1} \text{ Na}^+$, verifying inhibition. The model accounts for the inhibitory effect of NH_4^+ but not of Na^+ . Note also that in our prior long-term (40-week) Zeo-SBR demonstration, Na^+ inhibition of nitrification was transient, as washout of Na^+ occurred over the first few SBR cycles (Aponte-Morales et al., 2016).

Despite these limitations, the excellent performance of the model in Figures 3.5 and 3.6, without the use of any adjustable parameters, suggests that the model developed herein can serve as a useful tool for designing and operating IX-assisted biological processes in the future.

3.5 Supplementary Information

3.5.1 Derivation of Equation for Aqueous-Phase Concentration of Na^+

The aqueous-phase concentration of Na^+ is required in the ion exchange (IX) isotherm (Equation 3.6), to establish equilibrium between the aqueous-phase and sorbed-phase concentrations of NH_4^+ . The aqueous concentration of sodium, C_{Na^+} , can be modeled by assuming that 1 meq of Na^+ is released from the chabazite for each 1 meq of NH_4^+ that is adsorbed onto the zeolite. Therefore, to determine the concentration of Na^+ in the liquid-phase, the volume-averaged solid phase NH_4^+ concentration is required. For spherical chabazite grains, the equation for the volume-averaged NH_4^+ concentration is given by:

$$\langle q_{\text{NH}_4^+} \rangle = \frac{3}{4\pi R^3} \int_{r=0}^{r=R} (4\pi r^2 dr) q_{\text{NH}_4^+}(r, t) \quad (3.12)$$

where $\langle q_{\text{NH}_4^+} \rangle$ is the volume-averaged NH_4^+ in the solid phase, R is the radius of a chabazite grain, $q_{\text{NH}_4^+}(r, t)$ and is the solid-phase concentration of NH_4^+ at coordinate r in the zeolite, and the limits of the integrand are from the center of a particle to the surface of the grain.

Application of the trapezoidal rule for numerical integration of Equation 3.12 results in

$$\langle q_{\text{NH}_4^+} \rangle = \frac{3M}{R^3 V} \sum_{i=1}^n \left[\frac{1}{2} (q_i + q_{i+1}) \right] \left[\frac{(2n-1)^2 \Delta r^3}{8} \right] \quad (3.13)$$

where n is the number of nodes in the finite difference grid utilized, q_i is the NH_4^+ concentration at i^{th} node, and Δr is the radial distance between nodes.

Thus, based on the assumption of a 1:1 ratio of IX between NH_4^+ and Na^+ , the equation for Na^+ in the aqueous phase is written as:

$$C_{\text{Na}^+} - \langle q_{\text{NH}_4^+} \rangle = 0 \quad (3.14)$$

Table 3.2: Parameters used to simulate concentration of chemical species in the bioreactors

Parameter	Definition	Value	Source
D_s	Surface diffusion coefficient	$5.6 \times 10^{-13} \text{ m}^2 \text{ s}^{-1}$	Fitted to homogeneous surface diffusion model (HSDM)
K	Selectivity coefficient	2.92 (dimensionless)	Fitted to ion exchange (IX) isotherm
Q	Maximum ion exchange capacity	1.81 meq g^{-1}	Fitted to ion exchange (IX) isotherm
$K_{I, AOB}$	AOB inhibition coefficient	1123 mg-N L^{-1}	Fitted to Andrew's equation
$K_{I, NOB}$	NOB inhibition coefficient	$122.2 \text{ mg-N L}^{-1}$	Fitted to Andrew's equation
$K_{s, AOB}$	half saturation coefficient AOB	5.0 mg-N L^{-1}	Rittmann and McCarty, 2003
$K_{s, NOB}$	half saturation coefficient NOB	0.9 mg-N L^{-1}	Rittmann and McCarty, 2003
$\hat{q}_{AOB} X_{AOB}$	maximum specific rate of substrate utilization for AOB multiplied by AOB biomass concentration	$0.89 \text{ mg-N g-VSS hr}^{-1}$	Fitted to Andrew's equation
$\hat{q}_{NOB} X_{NOB}$	maximum specific rate of substrate utilization for NOB multiplied by NOB biomass concentration	$1.53 \text{ mg-N g-VSS hr}^{-1}$	Fitted to Andrew's equation

3.5.2 Numerical Approximation

Equations 3.3-3.11 in the manuscript represent the IX-assisted nitrification model and requires a numerical approximation to simulate the concentration histories of all chemical species. The numerical simulations were performed using the MATLAB software version 2016a. To determine the temporal evolution of concentrations of chemical species in the zeolite-amended bioreactor, a finite-difference approximation was used. A Crank-Nicolson scheme was adopted for the temporal discretization (Crank and Nicolson, 1996), and the spatial discretization utilized a centered difference approximation. A predictor-corrector method was used to iterate the algorithm through time due to the non-linearity arising from the IX isotherm in Equation 3.6 in the manuscript. The time step was specified as 0.01 h and chabazite particles were discretized into 50 equally spaced radial intervals. A trapezoidal numerical integration was done for the solid phase to determine the volume-averaged NH_4^+ concentration. The initial conditions for the solid phase are given in the manuscript, and the initial conditions for species in the aqueous phase are given by:

$$\left\{ \begin{array}{l} C_{\text{NH}_4^+}(t=0) = C_{0,\text{NH}_4^+} \\ C_{\text{NO}_2^-}(t=0) = C_{0,\text{NO}_2^-} \\ C_{\text{NO}_3^-}(t=0) = C_{0,\text{NO}_3^-} \\ C_{\text{Na}^+}(t=0) = C_{0,\text{Na}^+} \end{array} \right\} \quad (3.15)$$

where the terms in the right-hand side of Equation 3.15 are initialized based on experimental conditions. The parameters used for simulations are provided in Table 3.2.

3.6 References

- American Public Health Association. *Standard Methods for the Examination of Water and Wastewater*. 22nd ed.; American Public Health Association, American Water Works, Water Environment Federation: Washington, DC, 2012.
- Amini, A.; Aponte-Morales, V.; Wang, M.; Dilbeck, M.; Lahav, O.; Zhang, Q.; Cunningham, J. A.; Ergas, S. J. Cost-effective treatment of swine wastes through recovery of energy and nutrients. *Waste Manage.* **2017**, *69*, (Supplement C), 508-517.
- Anthonisen, A. C.; Loehr, R. C.; Prakasam, T. B. S.; Srinath, E. G. Inhibition of Nitrification by Ammonia and Nitrous Acid. *J. Water Pollut. Control Fed.* **1976**, *48*, (5), 835-852.
- Aponte-Morales, V. E. Ammonium Removal from High Strength Wastewater Using a Hybrid Ion Exchange Biological Process. Ph.D. Dissertation, University of South Florida, Tampa, FL, 2015.
- Aponte-Morales, V. E.; Tong, S.; Ergas, S. J. Nitrogen Removal from Anaerobically Digested Swine Waste Centrate Using a Laboratory-Scale Chabazite-Sequencing Batch Reactor. *Environ. Eng. Sci.* **2016**, *33*, (5), 324-332.
- Boiran, B.; Couton, Y.; Germon, J. C. Nitrification and denitrification of liquid lagoon piggery waste in a biofilm infiltration-percolation aerated system (BIPAS) reactor. *Bioresour. Technol.* **1996**, *55*, (1), 63-77.
- Cantrell, K. B.; Ducey, T.; Ro, K. S.; Hunt, P. G. Livestock waste-to-bioenergy generation opportunities. *Bioresour. Technol.* **2008**, *99*, (17), 7941-7953.
- Carrera, J.; Jubany, I.; Carvallo, L.; Chamy, R.; Lafuente, J. Kinetic models for nitrification inhibition by ammonium and nitrite in a suspended and an immobilised biomass systems. *Process Biochem.* **2004**, *39*, (9), 1159-1165.
- Crittenden, J. C.; Trussell, R. R.; Hand, D. W.; Howe, K. J.; Tchobanoglous, G. Ion Exchange. In *MWH's Water Treatment: Principles and Design, Third Edition*, John Wiley & Sons, Inc.: Hoboken, NY, 2012; 1263-1334.
- Dyer, A. *An Introduction to Zeolite Molecular Sieve*. John Wiley & Son, Ltd.: Chichester, 1988; 53, 164.
- Farag, A. M.; Harper, D. D. A review of environmental impacts of salts from produced waters on aquatic resources. *Int. J. Coal Geol.* **2014**, *126*, 157-161.
- Gee Chai, S.; Suidan Makram, T.; Pfeffer John, T. Modeling of Nitrification Under Substrate-Inhibiting Conditions. *J. Environ. Eng.* **1990**, *116*, (1), 18-31.
- Green, M.; Mels, A.; Lahav, O. Biological-ion exchange process for ammonium removal from secondary effluent. *Water Sci. Technol.* **1996**, *34*, 449-458.

Guan, T. Y.; Holley, R. A. Pathogen Survival in Swine Manure Environments and Transmission of Human Enteric Illness—A Review Sponsoring organizations: Manitoba Livestock Manure Management Initiative and Manitoba Rural Adaptation Council. *J. Environ. Qual.* **2003**, 32, (2), 383-392.

Guo, X.; Zeng, L.; Jin, X. Advanced regeneration and fixed-bed study of ammonium and potassium removal from anaerobic digested wastewater by natural zeolite. *J. Environ. Sci.* **2013**, 25, (5), 954-961.

Hand, D.; Crittenden, J.; Thacker, W. User-Oriented Batch Reactor Solutions to the Homogeneous Surface Diffusion Model. *J. Environ. Eng.* **1983**, 109, (1), 82-101.

Hatfield, J.; Brumm, M.; Melvin, S. Swine manure management. In *Agricultural uses of municipal, animal, and industrial byproducts*; Wright, R.J., Kemper, W.D, Millner, P.D., Power, J.F., Korcak, R.F., Eds.; U.S. Department of Agriculture, Agricultural Research Service: **1998**, 44, 78-90.

He, S.-B.; Xue, G.; Kong, H.-n.; Li, X. Improving the performance of sequencing batch reactor (SBR) by the addition of zeolite powder. *J. Hazard. Mater.* **2007**, 142, 493-499.

Hedstrom, A. Ion Exchange of Ammonium in Zeolites: A Literature Review. *J. Environ. Eng.* **2001**, 127, (8), 673-681.

Jung, J.-Y.; Chung, Y.-C.; Shin, H.-S.; Son, D.-H. Enhanced ammonia nitrogen removal using consistent biological regeneration and ammonium exchange of zeolite in modified SBR process. *Water Res.* **2004**, 38, (2), 347-354.

Kim, Y. M.; Park, D.; Lee, D. S.; Park, J. M. Inhibitory effects of toxic compounds on nitrification process for cokes wastewater treatment. *J. Hazard. Mater.* **2008**, 152, (3), 915-921.

Koon, J. H.; Kaufman, W. J. Ammonia Removal from Municipal Wastewaters by Ion Exchange. *J. Water Pollut. Control Fed.* **1975**, 47, (3), 448-465.

Krishna, R.; Wesselingh, J. A. The Maxwell-Stefan approach to mass transfer. *Chem. Eng. Sci.* **1997**, 52, (6), 861-911.

Langwaldt, J. Ammonium removal from water by eight natural zeolites: A comparative study. *Sep. Sci. Technol.* **2008**, 43, (8), 2166-2182.

Leyva-Ramos, R.; Monsivais-Rocha, J. E.; Aragon-Piña, A.; Berber-Mendoza, M. S.; Guerrero-Coronado, R. M.; Alonso-Davila, P.; Mendoza-Barron, J. Removal of ammonium from aqueous solution by ion exchange on natural and modified chabazite. *J. Environ. Manage.* **2010**, 91, (12), 2662-2668.

Lito, P. F.; Cardoso, S. P.; Loureiro, J. M.; Silva, C. M. Ion Exchange Equilibria and Kinetics. In *Ion Exchange Technology I: Theory and Materials*, Inamuddin-Luqman, M. Eds. Springer Netherlands: Dordrecht, 2012; 51-120.

Maas, E. In *Testing crops for salinity tolerance*, Proc. Workshop on Adaptation of Plants to Soil Stresses. Riverside, CA, August 1-4, 1993; Maranville, J.W., Baligar, B.V., Yohe, J.M., Eds.; Univ of Ne: Lincoln, NE, 234-247.

Massé, D. I.; Talbot, G.; Gilbert, Y. On farm biogas production: A method to reduce GHG emissions and develop more sustainable livestock operations. *Anim. Feed Sci. Technol.* **2011**, *166–167*, 436-445.

Piciooreanu, C.; Kreft, J.-U.; van Loosdrecht, M. C. M. Particle-Based Multidimensional Multispecies Biofilm Model. *Appl. Environ. Microbiol.* **2004**, *70*, (5), 3024-3040.

Rittmann, B. E.; McCarty, P. L. *Environmental Biotechnology: Principles and Applications*. The McGraw-Hill Companies: NY, 2012.

Roy, W. R.; Roulier, M. H. *Batch-type procedures for estimating soil adsorption of chemicals*; Technical Report EPA/530/SW-87/006-F; USEPA: Washington, DC, 1991.

Sanchez, O.; Aspe, E.; Marti, M. C.; Roeckel, M. The effect of sodium chloride on the two-step kinetics of the nitrifying process. *Water Environ. Res.* **2004**, *76*, (1), 73-80.

Semmens, M.; Porter, P. Ammonium removal by ion exchange: using biologically restored regenerant. *J. Water Pollut. Control Fed.* **1979**, 2928-2940.

Turk, O.; Mavinic, D. S. Maintaining nitrite build-up in a system acclimated to free ammonia. *Water Res.* **1989**, *23*, (11), 1383-1388.

U. S. Environmental Protection Agency, Fate, *Transport and Transformation Test Guidelines - Adsorption/Desorption Batch Equilibrium*; Technical Report OPPTS 835.1230; USEPA: Washington, DC, 2008.

Varel, V. H.; Wells, J. E.; Shelver, W. L.; Rice, C. P.; Armstrong, D. L.; Parker, D. B. Effect of anaerobic digestion temperature on odour, coliforms and chlortetracycline in swine manure or monensin in cattle manure. *J. Appl. Microbiol.* **2012**, *112*, (4), 705-715.

Wang, S.; Peng, Y. Natural zeolites as effective adsorbents in water and wastewater treatment. *Chem. Eng. J.* **2010**, *156*, (1), 11-24.

Wei, Y.; Ye, Z.; Wang, Y.; Ma, M.; Li, Y. Enhanced ammonia nitrogen removal using consistent ammonium exchange of modified zeolite and biological regeneration in a sequencing batch reactor process. *Environ. Technol.* **2011**, *32*, (12), 1337-1343.

Weiner, E. R. *Applications of Environmental Aquatic Chemistry: A Practical Guide, Third Edition*. Taylor & Francis Group: Boca Raton, FL, 2012.

Zhang, J.-Z.; J. Fischer, C. *A simplified resorcinol method for direct spectrophotometric determination of nitrate in seawater*. *Marin Chem.* **2006**, *99*, 220-226.

CHAPTER 4:

HYBRID ALGAL PHOTOSYNTHESIS AND ION EXCHANGE (HAPIX) PROCESS FOR HIGH AMMONIUM STRENGTH WASTEWATER TREATMENT²

4.1 Introduction

Management of the nitrogen (N) cycle was identified by the National Academy of Engineering as one of the grand challenges of the 21st century. A major source of N is high ammonium (NH_4^+) strength wastewaters, such as industrial wastewaters (e.g. food processing, fertilizer, plastic industries), landfill leachate, source separated urine and centrate from anaerobic digestion. These wastewater streams are challenging and expensive to treat (Kjeldsen et al. 2002, Udert et al. 2003). Anaerobic digestion centrate is of particular interest since anaerobic digestion technology is being promoted for stabilization and bioenergy recovery from waste resources, such as sewage sludge and food waste (Cantrell et al. 2008). The high NH_4^+ strength centrate is often recycled back to the head of the wastewater treatment plant, resulting in high irregular nutrient loads that can upset mainstream biological N removal (BNR) processes and increase costs (Fux et al. 2006, Wett and Alex 2003).

Although a number of advanced BNR processes, such as shortcut N removal (nitrification-denitrification) and anaerobic ammonium oxidation (anammox), have been developed to reduce the energy and chemical costs of high NH_4^+ strength wastewater treatment (Kotay et al. 2013, Lackner et al. 2014, Third et al. 2005), utilization of algae for treatment of these wastewater presents an

² “This chapter is adapted from an accepted manuscript in *Water Research* by Wang, M.; Payne, K.; Tong, S.; Ergas, S. A hybrid algal photosynthesis and ion-exchange (HAPIX) process for side stream wastewater treatment: Experimental and modeling studies.”

opportunity for co-production of biofuels, high value chemicals and animal feeds (Li et al. 2011, Park et al. 2010, Rusten and Sahu 2011, Wang and Park 2015, Wang et al. 2015). The high nutrient concentrations in these wastewaters also have the potential to support higher algal biomass densities than low-strength wastewaters (e.g. secondary & tertiary effluent), resulting in lower downstream costs for thickening and dewatering (Halfhide et al. 2014). A challenge with this approach is that $\text{NH}_4^+\text{-N}$ concentrations greater than 200 to 300 mg L^{-1} are known to inhibit algae growth due to the uncoupling effect of free NH_3 on the photosynthetic processes in chloroplasts (Crofts 1966, Lin et al. 2007, Park et al. 2010). Prior studies have addressed this issue by dilution with fresh water or low strength wastewater or using a fed-batch bioreactor approach (Wang et al. 2010, Wang et al. 2015, Yuan et al. 2012). Strategies to reduce the NH_3 toxicity are needed to promote the implementation of algae cultivation in high NH_4^+ strength wastewater

Zeolites are natural hydrated aluminosilicate materials with a high affinity for NH_4^+ ions (Malovanyy et al. 2013, Rožić et al. 2000). Common forms of natural zeolite include clinoptilolite, mordenite, phillipsite, chabazite, stilbite, analcime and laumontite (Wang and Peng 2010). Clinoptilolite is the most abundant and lowest cost natural zeolite material; however, its NH_4^+ capacity is low compared with chabazite (Amini et al. 2017, Aponte-Morales 2015). Prior studies of biological treatment of high NH_4^+ strength wastewaters have successfully used the ion exchange (IX) capacity of natural zeolites to reduce the toxicity of free NH_3 to nitrifying prokaryotes (Aponte-Morales et al. 2016, Aponte-Morales et al. 2018, Martins et al. 2017, Tada et al. 2005). Combining IX process with algae cultivation has the potential to treat high NH_4^+ strength wastewater without dilution. Furthermore, there is a lack of studies investigating the mathematical description of IX combined with algal photosynthesis. Such a study can improve the understanding of the underlying physical, chemical, and biological mechanisms.

Several prior studies have focused on surface diffusion models of IX in zeolites and microporous materials (Auerbach et al. 2003, Krishna and Wesselingh 1997, Lito et al. 2014) or algal photosynthesis kinetics (Juneja et al. 2013, Lee and Zhang 2016). However, coupling IX and algal photosynthesis kinetics into a mathematical framework has not previously been investigated. A prior study in our research group demonstrated that a Fickian-based continuum-scale model, the homogenous surface diffusion model (HSDM), can accurately describe IX kinetics in zeolites (Aponte-Morales et al., 2018). On the other hand, microalgae growth is influenced by several factors including temperature, light availability, pH and the concentrations of nutrients such as N and phosphorus (P) (Juneja et al. 2013). A comprehensive review of the various models of microalgae growth kinetics is presented elsewhere (Lee and Zhang 2016); in general, models of microalgae growth kinetics can be categorized as single limitation or co-limitation approaches. In single limitation models, it is commonly assumed that algal growth kinetics is either limited by a single substrate (N, P, CO₂) or light intensity. For co-limitation models, either a threshold or multiplicative conceptualization is adopted (Lee and Zhang 2016).

In this study, we propose a novel hybrid algal photosynthesis and ion-exchange (HAPIX) process to recover nutrients from high NH₄⁺ strength wastewater. It is hypothesized that NH₄⁺ in the wastewater will be absorbed by the zeolite and exchanged with cations such as Na⁺ and K⁺. Adsorption of NH₄⁺ will reduce free NH₃ concentrations in the liquid phase to below inhibitory levels for algae growth. Moreover, algae grown under N-depleted conditions tend to accumulate lipids, while algae grown in high N wastewater tend to have a higher protein content (Shifrin and Chisholm 1981, Solovchenko et al. 2008). We hypothesize that by controlling the zeolite dosages aqueous phase NH₄⁺ concentrations are controlled, which will tune the intracellular contents of harvested algae. For example, low IX doses will result in algae with a high protein content, which

can be used as a biofertilizer, while high IX doses will produce algae with a high lipid content, which can be used for biofuel production.

To our knowledge, this is the first study to combine IX with algal photosynthesis for high NH_4^+ strength wastewater treatment. HAPIX process benefits are to: 1) reduce the toxicity of high strength NH_4^+ wastewater; 2) handle the shock load by the hybrid IX process and enhance system stability (Jorgensen and Weatherley 2003); 3) regulate the production of intracellular products by varying zeolite dosages. The specific objectives of this study are to: 1) evaluate the impact of zeolite dosage on the nutrient removal efficiencies; 2) assess the impact of zeolite dosages on intracellular compounds of harvested algal biomass; 3) develop a mathematical model to predict NH_4^+ removal and biomass growth in the HAPIX reactor.

4.2 Materials and Methods

4.2.1 Characteristics of Anaerobic Digester Centrate

Centrate used in this study was obtained from a pilot anaerobic digester treating waste activated sludge from an enhanced biological N and P removal treatment facility (Tampa, Florida). The anaerobic digester had a working volume of 24 L and was operated for over 100 days under thermophilic (45 -55°C) conditions with a solids residence time (SRT) of 20 days. Effluent from the digester was centrifuged at 4000 rpm for 15 minutes. The supernatant from this initial solid-liquid separation step was further filtered through 1.5 μm filter paper (934-AH, Whatman). Characteristics of the centrate are summarized in Table 4.1.

Table 4.1: Characteristics of centrate from anaerobic digestion of waste activated sludge

Parameters	Unit	Value
NH ₄ ⁺ -N	mg L ⁻¹	1,180
PO ₄ ³⁻ -P	mg L ⁻¹	267±0.0
VFA	mg L ⁻¹	822±4.9
COD	mg L ⁻¹	2,340±0
Alkalinity	mg L ⁻¹ as CaCO ₃	2,585±304
pH	-	8.0±0.1

4.2.2 HAPIX Reactor Setup

Wild-type algae *Chlorella* (95% of the total cells) originally harvested from a local wastewater treatment plant were enriched in diluted anaerobic digester centrate for this study (Halfhide et al. 2014). Algae were settled for 24 hours, and the settled algae were collected as the inoculum for the HAPIX reactors. The chlorophyll *a* and dry weight of the algal inoculum was 81.1±2.5 mg L⁻¹ and 5,412 ± 159 mg L⁻¹, respectively. The algal inoculum was washed three times with DI water to remove residuals from the diluted sludge centrate before seeding the HAPIX reactors.

Bowie chabazite (a type of zeolite, product code: AZLB-Ca) from St. Cloud Mine (New Mexico) was sieved to obtain a particle size between 1.0-1.4 mm. Chabazite particles were washed with DI five times to remove fine particles. Washed chabazite was placed in 500 mL Erlenmeyer flasks with DI water and shaken at 110 rpm for 24 hours. The pretreated chabazite was dried at 100 °C in an oven for the following experiments. Chabazite dosages evaluated were 60 (IA-60), 150 (IA-150) and 250 (IA-250) g L⁻¹, based on isotherm and kinetics studies (S1). The operational strategy of the HAPIX reactors is shown in Figure 1. Briefly, one liter Erlenmeyer flasks were set up with 500 mL of centrate and various chabazite dosages. Reactors were set up in duplicate in a 21±2°C constant temperature room. A shaking table set at 100 ± 10 rpm provided mixing for all the reactors. After 24 hours' adsorption when the NH₄⁺ concentration was reduced below 200 mg

L⁻¹, 40 mL of pre-washed algae inoculum was added to each flask, which was recorded as Day 0 of the HAPIX process. DI water was added as needed to account for water evaporation. The reactors were continuously illuminated at $121 \pm 6 \mu\text{mol m}^{-2} \text{s}^{-1}$ by three 35 W Commercial Electric white LED lights. Chabazite always remained resident at the bottom of reactors due to its high density. The HAPIX reactors were operated in three phases (Figure 4.1). During Phase 1, algae were grown in the centrate after IX. Suspended algae were harvested by centrifugation at 3,800 rpm for 10 minutes when the algal biomass concentrations reached stationary state. Supernatant after algae harvesting was replaced into the original reactors for the continuous growth of algae during Phase 2 and Phase 3. Reactors with only algal biomass were also set up as controls (A-control). Chabazite at the same dosages as HAPIX reactors without the addition of algae were set up as the IX controls (IX-60, IX-150 and IX-250). The IX controls were covered with parafilm and aluminum foil to reduce the potential biological activity.

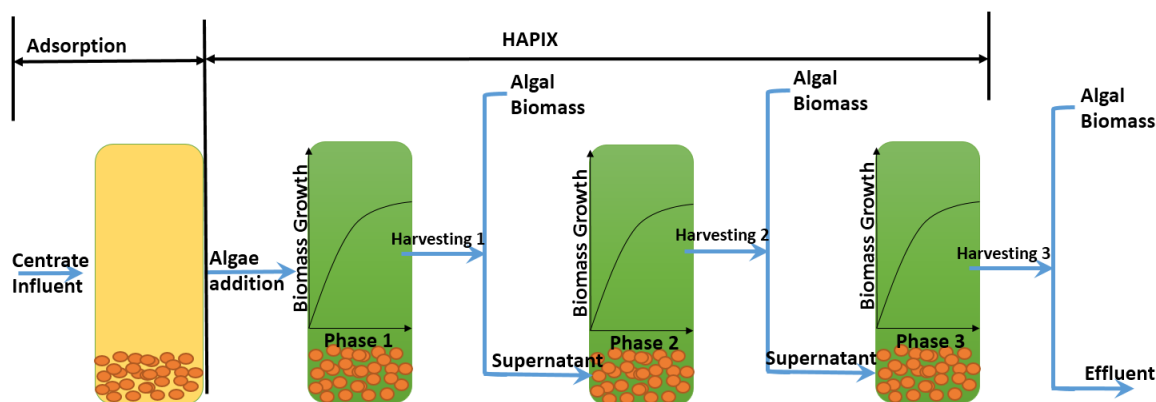


Figure 4.1: Overall operational strategy of HAPIX reactors

4.2.3 Analytical Methods

Biomass dry weight (total suspended solids [TSS]), total volatile solids (VSS) and alkalinity were measured according to *Standard Methods* (APHA et al. 2012). COD was measured according to *Standard Methods* (5200B) using Orbeco-Hellige mid-range (0-1,500 mg L⁻¹) COD

kits. Total P was measured using Hach TNT plus 845 test kits. Total N was measured by Hach TNT plus 827 and TNT 828 test kits. Volatile fatty acid (VFA) concentrations as acetic acid were measured by the esterification method using Hach TNT plus 872 test kits. Cations, including NH_4^+ , Na^+ , K^+ , Ca^{2+} , and Mg^{2+} concentrations were measured using a Metrohm Peak 850 Professional AnCat ion chromatography (IC) system (Metrohm Inc., Switzerland).

The harvested algae were freeze-dried (Labconco, US) for starch, lipid, and protein analysis. The total starch content of the algal biomass were measured using Megazyme total starch (AA/AMG) kits (catalog # K-TSTA), following Association of Official Agricultural Chemists (AOAC) Method 996.11. Protein content was analyzed by the bicinchionic acid colorimetric method (BAC) using Micro BC Assay Kits (Interchim, France). The lipid contents were analysis by a commercial laboratory (Eurofins Scientific, US) according to the AOAC Method 996.06.

4.2.4 Statistical Analysis

The statistical differences of the nitrogen removal and intracellular contents of algae at different zeolite dosages were evaluated by ANOVA ($P < 0.05$) using Excel 2013 (Microsoft, US).

4.3 Mathematical Modeling

A mathematical model was developed to test the hypothesis that IX and photosynthetic growth of algae captures the processes of NH_4^+ removal and biomass production in the HAPIX reactors. The model considers the limiting diffusion process as intraparticle surface diffusion, which is characterized by probabilistically rare hops of ions between IX sites in the zeolite framework (Auerbach et al. 2003). For ionic fluxes based on Fickian diffusion, the flux term is given by:

$$J_{\text{NH}_4^+} = -\rho D_s \left. \frac{\partial q_{\text{NH}_4^+}}{\partial r} \right|_{r=R} \quad (4.1)$$

where $J_{NH_4^+}$ (meq m⁻² h⁻¹) is the flux of NH₄⁺ ions, ρ (g m⁻³) is the density of the chabazite particles, D_s (m² h⁻¹) is the surface diffusivity, r (m) is the radial coordinate within the solid material, $q_{NH_4^+}$ (meq g⁻¹) is the solid-phase NH₄⁺ concentration, and R (m) is the radius of a chabazite particle. In the solid phase, the mass transfer of NH₄⁺ ions by surface diffusion is given by:

$$\frac{\partial q_{NH_4^+}}{\partial t} = \frac{D_s}{r^2} \frac{\partial}{\partial r} \left(r^2 \frac{\partial q_{NH_4^+}}{\partial r} \right) \quad (4.2)$$

where r (m) is the radial coordinate within the solid material, $q_{NH_4^+}$ (meq g⁻¹) is the solid-phase NH₄⁺ concentration (meq g⁻¹), t (d) is time, and D_s (m² d⁻¹) is the surface diffusion coefficient. Key limiting factors of algal growth are light, CO₂, N, and P (Lee and Zhang 2016). Recently, a co-limitation kinetic model was developed and provided a reasonable growth prediction rate in comparison to experimental *Chlorella* growth data (Lee and Zhang 2016). It has been shown previously that for NH₄⁺-N concentrations ≤ 150 mg L⁻¹, co-limitation without inhibition is an appropriate assumption (Lee and Zhang 2016); therefore, we adopted a Monod expression for the N utilization rate. Light and temperature factors were expressed using the Chalker model combined with the Arrhenius equation, which leads to the following rate equation:

$$r_A = \frac{\mu_{\max} C_{NH_4^+} X_A}{Y_A (K_{S,NH_4^+} + C_{NH_4^+})} * \theta^{(T-20)} \tanh(I_{av} / I_k) \quad (4.3)$$

where μ_{\max} (d⁻¹) is the maximum specific growth rate, X_A (g L⁻¹) is the algal biomass concentration, Y_A is the yield coefficient (dimensionless), K_{S,NH_4^+} (meq L⁻¹) is the half saturation constant, θ (dimensionless) is the Arrhenius growth coefficient, I_k (μ mol photon m⁻² d⁻¹) is the light half saturation coefficient, T is temperature (°C), and I_{av} (μ mol photon m⁻² d⁻¹) is the average irradiance.

The average irradiance term, I_{av} ($\mu\text{mol photon m}^{-2} \text{ d}^{-1}$), is included to account for light attenuation in the HAPIX reactor, caused by self-shading by algal biomass and is given by:

$$I_{av} = \frac{I_0}{kdX_A} [1 - \exp(-kdX_A)] \quad (4.4)$$

where I_0 ($\mu\text{mol photon m}^{-2} \text{ d}^{-1}$) is the incident light intensity, k ($\text{m}^2 \text{ g}^{-1}$) is the light attenuation coefficient, and d (m) is the reactor diameter. Assuming the temporal dynamics of the aqueous phase NH_4^+ -N concentration is driven by IX and algal biosynthesis, we combined the rate expression (Equation 4.3) with a Fickian surface diffusion flux term to get the following expression for the aqueous phase NH_4^+ -N concentration:

$$\left. \frac{dC_{\text{NH}_4^+}}{dt} = -\frac{3M}{RV} D_s \frac{\partial q_{\text{NH}_4^+}}{\partial r} \right|_{r=R} - \frac{\mu_{\max} C_{\text{NH}_4^+} X_A}{Y_A (K_{S,\text{NH}_4^+} + C_{\text{NH}_4^+})} * \theta^{(T-20)} \tanh(I_{av} / I_k) \quad (4.5)$$

where M (g) is the mass of zeolite, R is the radius of a chabazite particle (m), and V is the volume of liquid (L). We assume no biomass decay, so that the phototrophic biomass growth rate can be obtained from the rate equation for algal photosynthesis:

$$\frac{dX_A}{dt} = Y_A r_A \quad (4.6)$$

To complete the mathematical model initial boundary conditions are required to solve the HAPIX system represented by Equations 4.5 and 4.6. To simulate the experimental conditions, during the 24-hour adsorption phase, no NH_4^+ was assumed to initially be present in the zeolite. When algae were added after the IX phase, both IX and NH_4^+ assimilation by algae occurred (HAPIX phase). The end of the adsorption phase provided the starting point for the simulation of the HAPIX phase. The following equations describe the initial conditions used for the solid phase:

$$q_{\text{NH}_4^+}(t=0, r) = 0 \quad \text{for the IX phase} \quad (4.7)$$

$$q_{NH_4^+}(t=0, r) = q_{hpx} \quad \text{for the HAPIX phase} \quad (4.8)$$

where $q_{NH_4^+}$ (meq g⁻¹) is initialized to have no adsorbed ions during the first 24 hours of the experiment, designated as the IX phase, and q_{hpx} (meq g⁻¹) is initial solid phase concentration during the HAPIX phase. The boundary conditions are given by:

$$\frac{\partial q_{NH_4^+}}{\partial r} = 0, r = 0, t > 0 \quad (4.9)$$

$$q_{NH_4^+}(r = R, t) = \frac{QKC_{NH_4^+}}{C_{Na^+} + KC_{NH_4^+}} \quad (4.10)$$

where C_{Na^+} (meq L⁻¹) is the aqueous phase concentration of Na⁺, and Q (meq g⁻¹) and K (dimensionless) are constants in the IX isotherm related to maximum adsorption capacity and affinity for the exchanger. Equation 4.9 imposes a symmetry boundary condition at the center of a chabazite particle and Equation 4.10 assumes that at the surface of the zeolite, the aqueous and sorbed phase concentrations of NH₄⁺ are in equilibrium. The initial conditions for species in the aqueous phase, and algal biomass concentration are given by:

$$\left\{ \begin{array}{l} C_{NH_4^+}(t=0) = C_{0,NH_4^+} \\ C_{Na^+}(t=0) = C_{0,Na^+} \\ X_A(t=0) = X_{0,A} \end{array} \right\} \quad (4.11)$$

where the terms on the right-hand side of equation 4.11 were initialized according to the observed experimental conditions. The model was implemented in Matlab 2016 (MathWorks, US). Details on the numerical implementation of the HAPIX model is discussed in the supplementary information.

4.4 Results and Discussion

4.4.1 NH₄⁺ Removal in HAPIX Reactors

Cation concentration results from all HAPIX reactors showed that Na⁺ was the major cation exchanged with NH₄⁺ (Figure 4.2). K⁺ in the centrate was also adsorbed by the chabazite. Prior studies have shown that the cation affinity sequence for chabazite is K⁺>NH₄⁺>Na⁺> Ca²⁺ > Mg²⁺ (Hedström 2001). The presence of K⁺ will compete with NH₄⁺ for IX sites (Wang and Peng 2010). However, NH₄⁺ concentrations (84 meq L⁻¹) in the centrate were eight times higher than K⁺ concentrations (10 meq L⁻¹), thus the effect of competition between K⁺ and NH₄⁺ was negligible during the initial 24 hours of the IX process.

Zeolite dosages of 60, 150 and 250 g L⁻¹ reduced the NH₄⁺-N concentrations from 1,180 mg L⁻¹ to 184 ± 40, 107 ± 7, and 53 ± 15 mg L⁻¹ after adsorption, respectively (Figure 4.2). The FA concentration, which was affected by total ammonia nitrogen (TAN, NH₃-N+NH₄⁺-N) concentration, pH, and temperature, was calculated according to Equation 4.12 (Anthonisen et al. 1976 and Kim et al. 2008):

$$NH_3 - N = \frac{TAN \times 10^{pH}}{\exp[(6334)/(273 + T)] + 10^{pH}} \quad (4.12)$$

where, NH₃-N is the concentration of FA, mg N L⁻¹; TAN is the concentration of TAN, mg L⁻¹ and T is the temperature, °C. The FA concentration of centrate used in this study was 4.7mM, which is much higher than the threshold inhibition level of algae of 2mM (Källqvist and Svenson 2003). Addition of zeolite at 60, 150, and 250 g L⁻¹ reduced the FA concentrations to 0.18, 0.05 and 0.07 mM, respectively, below the inhibitory level for algae.

The growth of algae in IA-60, IA-150 and IA-250 reactors during Phase 1 further reduced the aqueous $\text{NH}_4^+\text{-N}$ concentrations to 47.3 ± 11.9 , 10.5 ± 2.8 , and 5.5 ± 0.2 mg L^{-1} , respectively. However, $\text{NH}_4^+\text{-N}$ concentrations in IX controls without algae remained constant at 140 ± 10 , 50 ± 10 , and 22 ± 6 mg L^{-1} for IX-60, IX-150, and IX 250, respectively. Harvesting algae and recycling the supernatant in Phases 2 and 3 supported the continuous growth of algae and maintained stable low $\text{NH}_4^+\text{-N}$ concentrations in the HAPIX reactors. The $\text{NH}_4^+\text{-N}$ concentrations of IA-60, IA-150 and IA-250 were reduced to 10.1 ± 0.8 , 6.5 ± 0.2 and 6.5 ± 1.1 mg L^{-1} at the end of Phase 3. The 60 g L^{-1} zeolite dosage resulted in significantly higher final $\text{NH}_4^+\text{-N}$ concentration ($P=0.003$) than dosages of 150 and 250 g L^{-1} , while final $\text{NH}_4^+\text{-N}$ concentrations with zeolite dosages of 150 and 250 g L^{-1} were not significantly different ($p=1$).

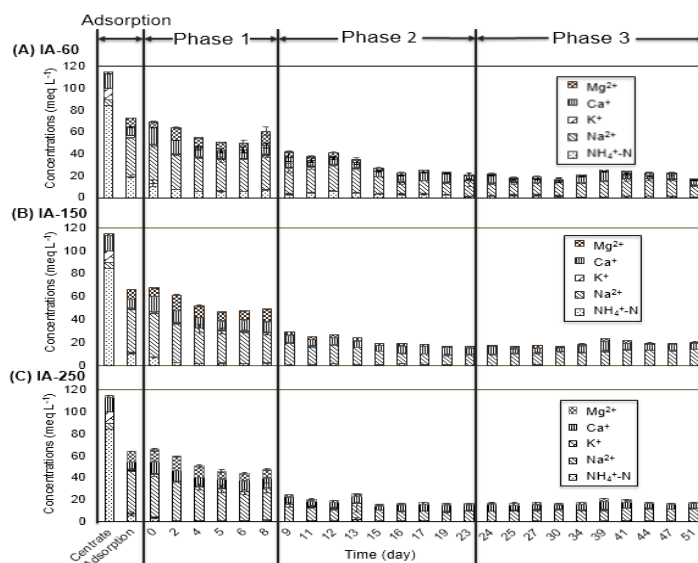


Figure 4.2: Temporal changes in cation concentrations in HAPIX reactors (A) IA-60: chabazite dosage of 60 g L^{-1} ; (B) IA-150: chabazite dosage of 150 g L^{-1} ; and (C) IA-250: chabazite dosage of 250 g L^{-1} . Centrate: cations in the centrate; Adsorption: cations after adsorption for 24 hours; Day 0 indicates the time when algae were added; Phase 1: initial algae growth phase; Phase 2 3; algae grown in recycled supernatant

4.4.2 Temporal Variation of Cations in HAPIX Reactors

The overall cation concentrations in all the HAPIX reactors showed decreasing trends. Besides IX onto chabazite, several physical, chemical, and biological mechanisms may contribute to changes in aqueous phase cation concentrations. The increase in pH from 7.5 to 9.5-10.1 on day 9 likely induced precipitation of Ca^{2+} and Mg^{2+} , which contributed to the decrease in cations and conductivity. Similar results were observed by Wang et al. (2016), whereby precipitation contributed to Ca^{2+} and Mg^{2+} removal in an algal system used to treat reverse osmosis concentrate. In addition to chemical precipitation, cell-surface adsorption and intracellular accumulation of metals by algae may have contributed to the decrease in cations (Suresh Kumar et al. 2015). The cell wall of algae consists of polysaccharides, proteins, lipids, and functional groups, such as carboxyl ($-\text{COOH}$), hydroxyl ($-\text{OH}$), phosphate ($-\text{PO}_3$), diphosphorus trioxide ($-\text{P}_2\text{O}_3$), amino ($-\text{NH}_2$), sulfhydryl ($-\text{SH}$), amide, primary amine-group, halide-group and aliphatic alkyl-group, which lead to a negative charge of the algal cell surface and a high affinity for cations. Most of the sites bond with Na^+ , Ca^{2+} and Mg^{2+} at high pH (González-Dávila 1995), which may have contributed to the decrease in cations. Furthermore, algae have been shown to favor assimilation of K^+ over Na^+ (Schaedle and Jacobson, 1965; 1967). In this study, a slight decrease in Na^+ was observed during Phase 2 after Day 13. The algae biomass most likely started to uptake Na^+ from solution when the K^+ was depleted (Barber and Shieh 1973).

The presence of anionic complexing ligands or organic matter in the centrate may have also affected the IX capacity. The ligands may compete with the surface for coordination reactions with metal ions (Suresh Kumar et al. 2015). The presence of organic matter may reduce the surface tension of the aqueous phase thereby enhancing the access of ions in the bulk liquid to the pores within the exchanger (Jorgensen and Weatherley 2003). Further research on cation transport and

uptake by algae is needed to identify the mechanisms involved, which will be helpful to understand the fate of cations in HAPIX reactors.

4.4.3 Biomass Production

As discussed in Section 4.4.1, the addition of chabazite decreased the FA concentration below the toxic level for algae at all dosages. Algae biomass in all the HAPIX reactors increased from 500 mg L⁻¹ to over 1500 mg L⁻¹ by Day 8 prior to harvesting (Figure 4.3). However, inhibition of algae growth due to the high NH₄⁺ concentrations of the centrate (>1,000 mg N L⁻¹) was observed in the algal control reactor without chabazite addition. Algae in IA-60 and IA-150 reached peak biomass concentrations on Day 8. However, algae in IA-250 reached steady state after only 6 days due to the relatively lower NH₄⁺ concentrations in the aqueous phase.

During Phase 3, a longer lag period for the algae growth was observed due to the constant low NH₄⁺ concentrations in the aqueous phase. The total biomass harvested over the three phases from IA-60, IA-150 and IA-250 were 1,587 mg, 1,248 mg and 1,187 mg, respectively. More biomass was harvested from the reactor with lower chabazite dosage. Supernatant was recycled in the reactors during Phases 2 and 3, thus less cations were available for IX with NH₄⁺ adsorbed in the solid phase. Introducing fresh centrate with selective cations and creating a concentration gradient between the aqueous and solid phases may increase the selective reversal of NH₄⁺ desorption to the aqueous phase. Additionally, the growth of biofilm on the surface of chabazite during the latter periods of Phases 2 and 3 may have inhibited mass transfer of NH₄⁺ from the chabazite to the aqueous phase. A longer lag period is required to stimulate algae growth when less NH₄⁺ is available in the aqueous phase.

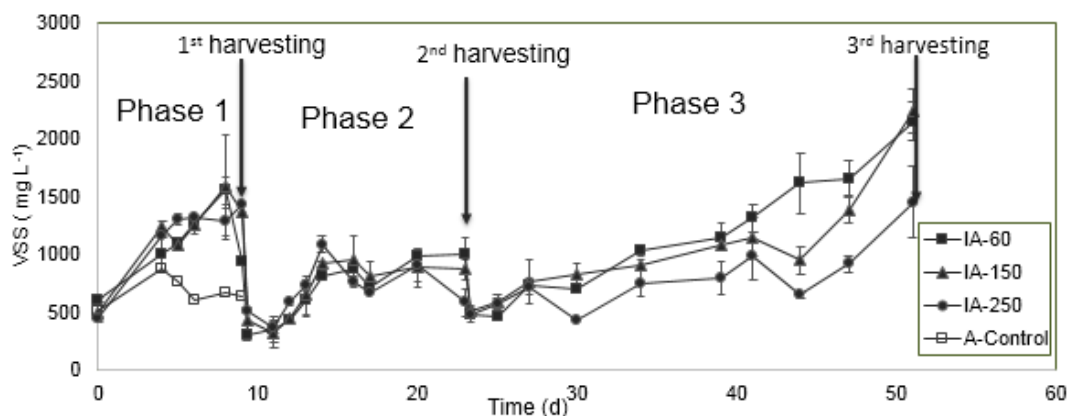


Figure 4.3: Algal biomass growth over time. Arrows indicate algae harvesting

4.4.4 Effect of Zeolite Dosages on Intracellular Contents of Biomass

The intercellular contents of algae were regulated by the NH_4^+ concentrations, which could be controlled by modifying chabazite dosages in HAPIX reactors. In this study, protein contents of the harvested biomass ranged from 27.7% to 57.1% (by dry weight) and were much higher than starch or lipid contents at all chabazite dosages (Figure 4.4). Algae grown in IA-60 had a significantly higher protein content (43.9 and 53.7 % for Phase 1 and Phase 3, respectively) in the biomass than IA-150 and IA-250, while differences between protein contents of algae harvested in chabazite dosage at 150 g L^{-1} and 250 g L^{-1} were not significant ($P=0.73$). Prior studies have shown that protein in algae are mainly enzymatic proteins, which could be useful as an animal feed source (Becker 2007).

The starch contents of biomass in IA-60, IA-150, and IA 250 during Phase 1 were 6.8, 4.8 and 2.8 % by dry weight, respectively. The starch contents of IA-60 and IA-150 in Phase 3 increased to 11.2 and 8.9% by dry weight, respectively. While the starch content of biomass in IA-250 was the same as Phase 1, probably due to the increase in ash content of the biomass in Phase 3. The VSS to TSS ratio of IA-250 in Phase 3 was only $54 \pm 15\%$. While the VSS to TSS ratio of

biomass harvested in IA-60 and IA-150 were $80 \pm 8\%$ and $80 \pm 1\%$, respectively. In general, the starch contents decreased with increasing zeolite dosages.

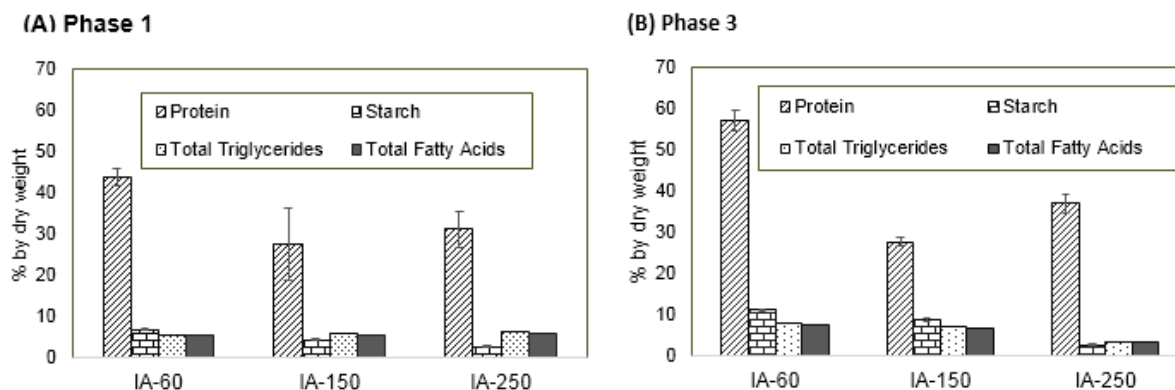


Figure 4.4: Intercellular contents of algae harvested in HAPIX reactors.

The total lipid as triacylglycerides (TGA) were less than 10% by dry weight for all the chabazite dosages (Figure 4.4). Algae harvested in Phase 3 had higher TGA content than Phase 1 at dosages of 60 g L^{-1} (IA-60) and 150 g L^{-1} (IA-150), due to the low aqueous NH_4^+ concentrations in Phase 3. However, the TGA content of IA-250 in Phase 3 was lower than that of Phase 1 because of the high ash content of the biomass harvested in Phase 3, as described earlier. Algae grown in wastewater with a high N content tend to have a low lipid content. *C. vulgaris* grown at 247 mg N L^{-1} had lipid content of 5.9% by dry weight (Converti et al. 2009). *Chlorella* grown in wastewater had the fatty acid methyl ester content of 9.98-11.04% by total VSS (Li et al. 2011). Algae accumulate lipids under N starvation conditions due to the intracellular fatty acid acyl-CoA and activate diacylglycerol acyltransferase that converts fatty acid acyl-CoA to triglyceride (Shifrin and Chisholm 1981, Solovchenko et al. 2008, Sukenik and Livne 1991). High NH_4^+ strength centrate treated by HAPIX reactors did not induce lipid accumulation in the algal biomass. However, using the HAPIX reactors to treat low strength wastewater, such as primary or secondary effluent, may create N deficient conditions that could accumulate high lipid contents in algae for biofuel production.

The lipid content of algae mainly consisted of triacylglycerols, which are composed of saturated and unsaturated fatty acids (Wang et al. 2010). Approximately 67-70% of fatty acids in the biomass harvested from HAPIX reactors were unsaturated, of which 43%-54% were polyunsaturated fatty acids (Table 2). The fatty acids are mainly composed of C16:0, C16:1, C18:0, C18:2 and C18:3, among which palmitic acid (C16:0), oleic acid (C18:1), linoleic acid (C 18:2), and linolenic acid (C 18:3) were the dominant fatty acids. Similar results were found by Wang et al. (2012), where the dominant fatty acids produced by *Chlorella* were hexadecanoic acid (C 16:0), linoleic acid (C 18:2), and linolenic acid (C 18:3). Although the unsaturated fatty acids are an ideal feedstock to produce biofuels, the low fatty acid content in the algae from the HAPIX reactors treating high NH_4^+ strength wastewater ($>1000 \text{ mg N L}^{-1}$), make them less economically viable for biofuel production.

Table 4.2: Profiles of fatty acids of algae harvested in HAPIX reactors from Phase 1 and Phase 3 (% of total fatty acids).

Samples Parameters	Phase 1			Phase 3		
	IA-60	IA-150	IA-250	IA-60	IA-150	IA-250
C16:0 (Palmitic Acid)	23%	23%	23%	26%	25%	24%
C16:1 Total (Palmitoleic Acid + isomers)	6%	5%	5%	4%	5%	5%
C 16:4 (Hexadecatetraenoic Acid)	2%	2%	1%	0%	0%	0%
C18:0 (Stearic Acid)	1%	2%	1%	1%	1%	1%
C18:1, Total (Oleic Acid + isomers)	19%	22%	19%	11%	12%	13%
C18:2, Total (Linoleic Acid + isomers)	28%	28%	30%	47%	45%	41%
C18:3, Total (Linolenic Acid + isomers)	18%	14%	16%	8%	10%	12%
Other Fatty Acids	3%	4%	5%	3%	2%	4%
Total Monounsaturated Fatty Acids	21%	24%	22%	15%	16%	17%
Total Polyunsaturated Fatty Acids	46%	43%	46%	54%	54%	53%
Total Saturated Fatty Acids	27%	28%	26%	30%	29%	29%
Total Trans Fatty Acid	6%	6%	5%	1%	1%	1%

4.5 Assessment of Mathematical Model for HAPIX

4.5.1 HAPIX Model Parameter Determination

Application of the mathematical model requires determination of parameters related IX process and algal photosynthetic processes. The experimental data for a chabazite dose of 150 g L⁻¹ was used for model calibration, while the doses of 60 g L⁻¹ and 250 g L⁻¹ were used for model validation. Estimation of the parameters for IX was performed in two steps: (i) the maximum ion

exchange capacity, Q , and the selectivity coefficient, K , were fit to batch isotherm data in S1; (ii) the surface diffusion coefficient, D_s , was determined by fitting the HSDM to experimental kinetic data in S1.

Estimation of the parameters related to algal photosynthesis was done using the following approach: (i) a sensitivity analysis was performed to determine the most sensitive parameters, (ii) the most sensitive parameters were calibrated, whereas the least sensitive parameters were determined from the literature. The sensitivity analysis was conducted using an automated algorithm that uses a Gauss-Marquadt-Levenberg method (Doherty, 2010). The algorithm calculates a dimensionless composite sensitivity value, which is a measure of the impact a change in a parameter value has on model output (Doherty, 2010). Results (Table 4.3) indicated that two most sensitive parameters were the light attenuation constant, k ($\text{m}^2 \text{g}^{-1}$) and the maximum specific growth rate, μ_{max} (d^{-1}). Calibration of k from 0.2 to 0.8 $\text{m}^2 \text{g}^{-1}$ and μ_{max} from 0.96 to 0.5 d^{-1} in the developed model lead to a good fit of the experimental data. Figure 4.5A shows the concentration history of $\text{NH}_4^+\text{-N}$ in the aqueous phase using the parameters shown in Table 4.3. The model captures the processes within HAPIX reactor as shown by the removal of most of the NH_4^+ within the first four hours of the experiment, followed by a period of relatively constant concentrations.

Table 4.3: Parameters used in numerical simulation of concentration profiles and the sensitivity scores

Parameter	Definition	Value	Source	Sensitivity score
IX Model Parameters				
K	Selectivity coefficient	2.9 (dimensionless)	Calibrated to isotherm data (S1)	Not calculated
Q	Maximum ion exchange capacity	2.8 meq g ⁻¹	Calibrated to isotherm data (S1)	Not calculated
D_s	Surface diffusion coefficient	9.1x10 ⁻¹² m ² d ⁻¹	Calibrated to kinetic data (S1)	Not calculated
Algal Photosynthesis Parameters				
K_{S,NH_4^+}	Half saturation coefficient	0.36 meq L ⁻¹	Lee and Zhang, 2016	0.000001
μ_{max}	maximum algae growth rate	0.5 d ⁻¹	Calibrated	73.7
k	Light attenuation rate	0.8 m ² g ⁻¹	Calibrated	24.1
θ	Arrhenius growth coefficient	1.35 (dimensionless)	Lee and Zhang, 2016	16.8
I_0	Incident light intensity	100 μ mol photon s ⁻¹	Measured	
I_k	Light saturation point	16.9 μ mol photon s ⁻¹	Lee and Zhang, 2016	0.00168

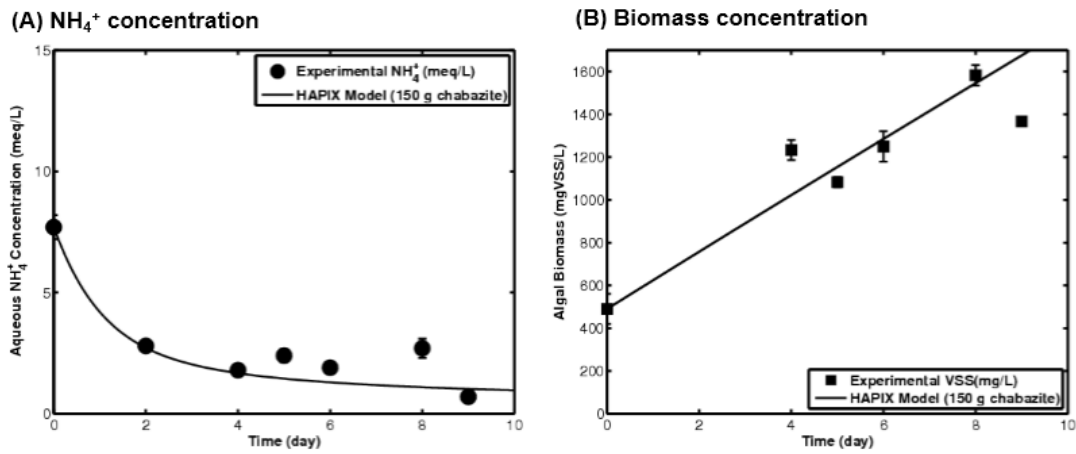


Figure 4.5: (A) NH₄⁺ concentration in HAPIX reactor over time; (B) Algae biomass concentration in HAPIX reactor over time. Chabazite dosage of 150 g L⁻¹

4.5.2 Prediction of NH_4^+ Concentrations in Aqueous Phase

Simulated temporal variations of the $\text{NH}_4^+\text{-N}$ concentration for dosages of 60 and 250 g L^{-1} are shown in Figure 4.6. Note that the simulation results only show model correspondence to Phase 1 of the experimental data, since the periodic algal harvesting and recycling of supernatant introduced external factors that may affect the IX process. Thus, it was infeasible to appropriately specify the solid phase NH_4^+ concentrations in Phases 2 and 3, which are required for assigning quantitative initial conditions in the model. The model is in reasonable agreement ($R^2 = 0.83$ and $R^2 = 0.7$) with the observed concentrations, showing that most of the removal occurs within the first 100 hours of the HAPIX experiment. The NH_4^+ removal rates markedly increased with the increase of zeolite dosage within the first 50 hours of the HAPIX experiment because high zeolite dosages tend to have more available IX sites for NH_4^+ adsorption. Overall, for each dosage the model provides a reasonable description of the experimental data. In general, the model predicted lower NH_4^+ concentrations than were observed in the effluent, most likely because mass transfer resistance due to algal biomass growth was neglected. Incorporating mass transfer resistance caused by the presence of a biofilm on the zeolite surface would reduce the rate at which ions diffuse into the zeolite, which would lead to an improved representation of the data. However, a caveat is that an additional parameter, a mass transfer coefficient, would need to be introduced, which would require further experimental justification.

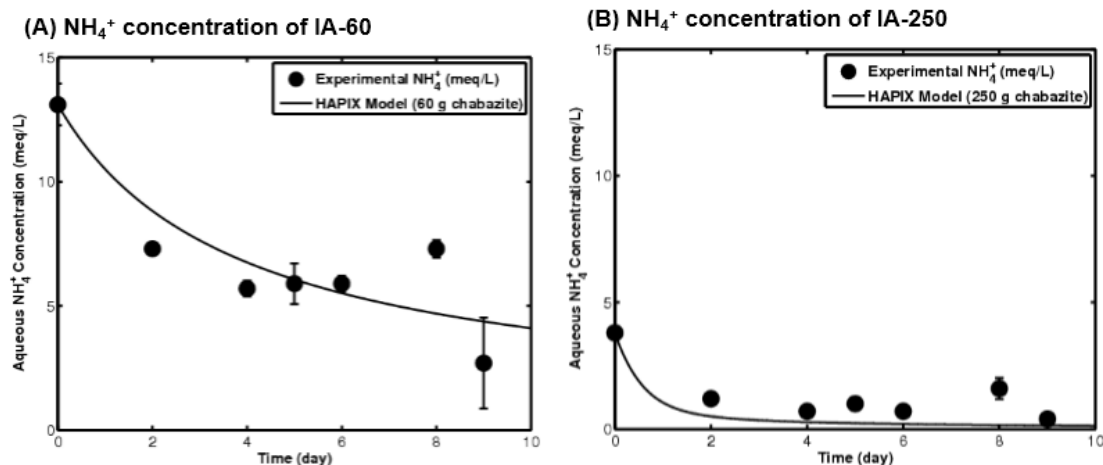


Figure 4.6: NH_4^+ concentration history in HAPIX reactor over time (A) dosage of 60 g L⁻¹, (B) dosage of 250 g L⁻¹

4.5.3 Prediction of Microalgae Biomass Concentration

Model and experimental microalgae growth results for Phase 1 of HAPIX operation for dosages of 60 and 250 g L⁻¹ are shown in Figures 4.7. The model prediction is in good agreement ($R^2 = 0.98$) with the experimental data for a dose of 60 g L⁻¹. However, for a dose 250 g L⁻¹ the model does not predict as rapid a rate of biomass growth observed experimentally ($R^2 = 0.58$). This slower growth rate predicted by the model is most likely because the highest dosage resulted in lowest aqueous phase NH_4^+ concentrations, so less N was available to support algal growth. Nevertheless, the model captures the trend of the algae growth data, showing linear growth characteristics. This positive trend corresponds with the utilization of NH_4^+ -N in solution and conversion of light, nutrients and CO_2 to new algal cells. The model behavior is consistent with recent findings from the model developed by Lee and Zhang (Lee and Zhang 2016), which was fit to experimental microalgae biomass growth for centrate of various characteristics.

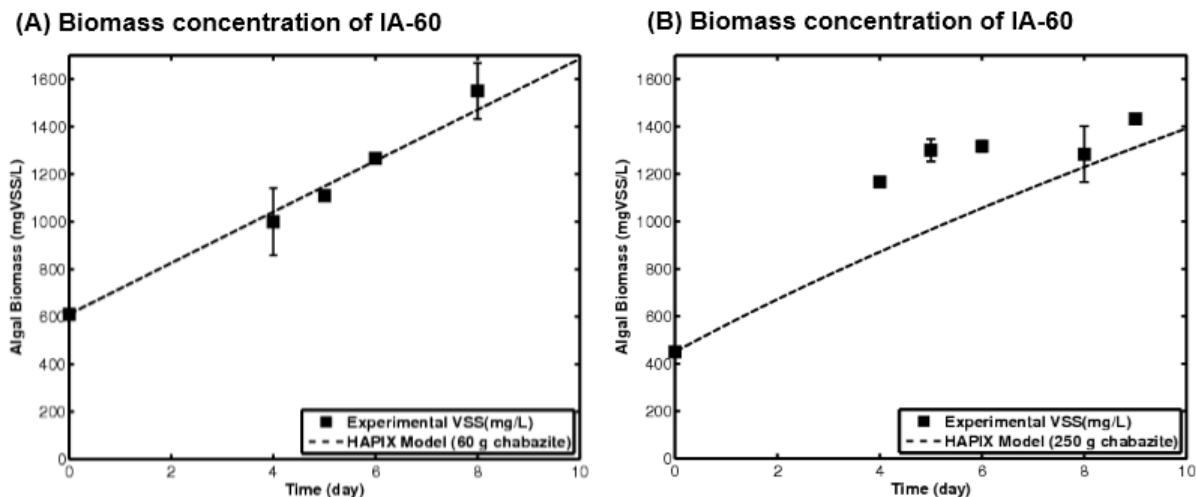


Figure 4.7: Algae biomass concentration in HAPIX reactors over time, (A) dosage of 60 g L⁻¹, (B) dosage of 250 g L⁻¹

4.6 Conclusions

This research demonstrated that the HAPIX process is suitable for treatment of high NH₄⁺ strength wastewater (>1000 mg N L⁻¹) without dilution. Zeolite dosages of 60, 150 and 250 g L⁻¹ resulted in stable NH₄⁺-N concentrations, lower than 10.1 ± 0.8 mg L⁻¹ in the effluent. Algae control reactors without zeolite addition showed no algae growth. The IX process reduced the FA of the centrate from 4.7mM to < 0.18 mM, and promoted algae growth. Different dosages of zeolite resulted in different NH₄⁺-N concentrations in the aqueous phase and different protein and starch contents of the algal biomass. Zeolite dosages at 60 g L⁻¹ resulted in higher protein and starch contents in the biomass than doses of 150 g L⁻¹ and 250 g L⁻¹. Valuable products may be extracted from the harvested biomass due to the high protein content (27% to 57% by dry weight). About 67-70% of the fatty acid in the biomass were unsaturated fatty acids. The lipid contents in all the cultures were lower than 10%, which are not economically feasible to produce biofuels. A mathematical model describing the HAPIX process was developed that accurately predicts the fate of NH₄⁺-N and algal biomass growth over time. The light attenuation constant (k) and the maximum specific growth rate (μ_{\max}) were the most sensitive parameters in the model. Calibration

of k from 0.2 to 0.8 m² g⁻¹ and μ_{\max} from 0.96 to 0.5 d⁻¹ in the developed model led to a good fit of the experimental data. The HAPIX process serves a two-fold purpose: treatment of high NH₄⁺-N strength wastewater and production of agricultural and commercial biopolymers. The main limitation of the modeling framework is that the model does not account for algal biomass growth on the zeolite with time. Future work could be focused on accounting for both suspended and attached growth into the model. Moreover, the model can be integrated with computational fluid dynamics models to simulate the performance of the HAPIX process for a full-scale system.

4.7 Supplementary Information

Batch isotherm study to evaluate the ion exchange capacity study was carried out by adding various mass of Chabazite in the fixed volume (100 mL) of centrate. The chabazite dosages used in the isotherm study were (g L⁻¹): 0, 13, 25, 50, 150, 250, respectively. The system was assumed to remove over 70% of NH₄⁺ after 24 hours reaction based preliminary study (data not shown). Kinetic study was performed with the mass of zeolite dosage of 150 g L⁻¹ with the fixed volume of liquid (300 mL). Samples were taken at 0.5 hr, 1 hr, 1.5 hr, 2 hr, 3 hr, 4 hr, 5 hr, 6hr, 12 hr and 24 hr for cations analysis. Both isotherm and kinetics study were set up in the 21±2°C constant temperature room in duplicate. Reactors were placed on the shaking table (VWR Advanced 3500 Orbital Shaker, USA), which was set at 90 rpm continuously.

Isotherm study (Figure 4.8) indicated that chabazite dosages more than 50 g L⁻¹ can reduce the NH₄⁺ concentration below the 200-300 mg/L. Kinetic study (Figure 4.9) provided the kinetic parameters for the modeling development.

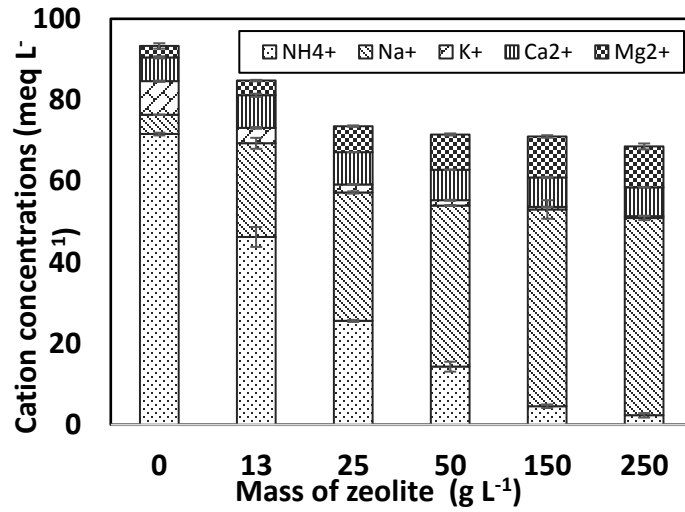


Figure 4.8: Isotherm study of NH₄⁺-N adsorption by zeolite after 24 hours

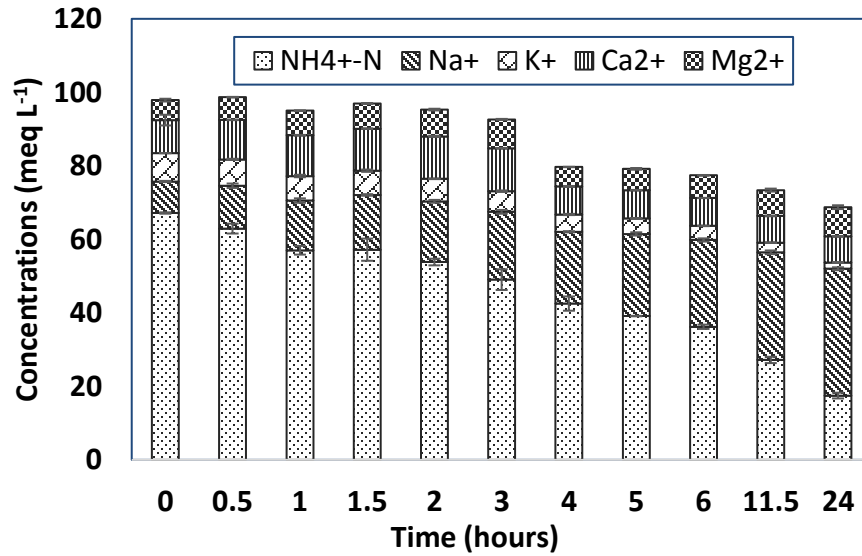


Figure 4.9: Kinetic study of NH₄⁺-N adsorption by 150 g L⁻¹ chabazite after 24 hours

The isotherm constants, Q and K , were determined manually adjusting the values to provide a reasonable fit to the experimental isotherm data. Figure 4.10 shows the simulated isotherm compared the experimental isotherm data for different dosages. Figure 4.11 shows the simulated homogeneous surface diffusion model (HSDM) NH₄⁺ and Na⁺ concentrations in the aqueous phase

as a function of time. The model captures the behavior of the IX kinetics, showing a decrease in the NH_4^+ concentration with most of the removal occurring within ~ 10 hours of the kinetic experiment. The removal of NH_4^+ by uptake onto the chabazite is associated with a release of Na^+ ions. The HSDM predicts a faster release of ions than observed, likely due to the presence of other competing cations, which were not accounted for in the mathematical model.

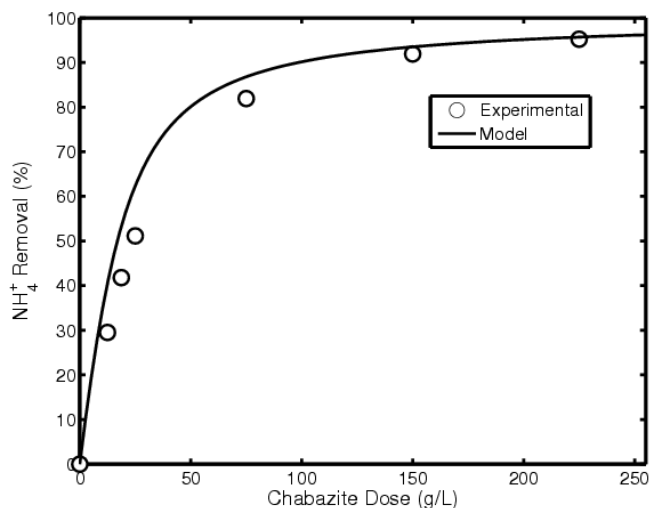


Figure 4.10: Effect of chabazite dose on the observed removal efficiency of NH_4^+

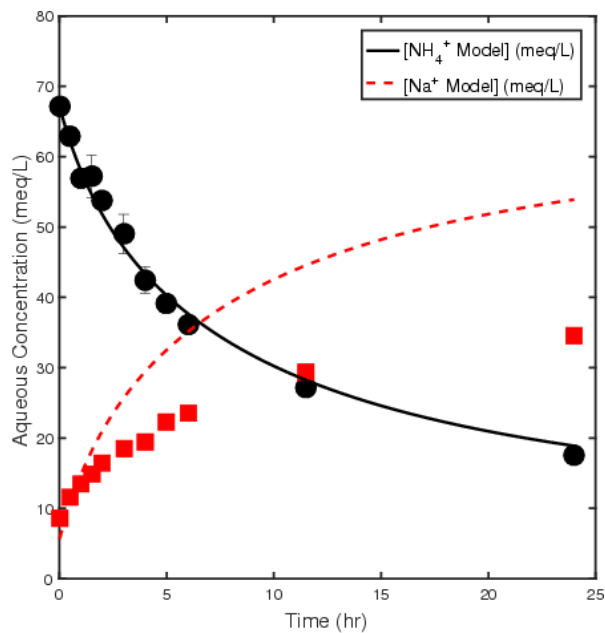


Figure 4.11: IX kinetics for NH_4^+ uptake onto chabazite and release of co-ion Na^+

The HAPIX model equations were solved by employing a finite-difference approximation, with a Crank-Nicolson scheme for the temporal discretization. The temporal resolution used in the numerical approximation was a time step size of 0.01 h. The chabazite particles were discretized into 50 evenly spaced intervals from the zeolite-bulk interface to the center of the particles using a centered difference scheme. A predictor-corrector approach was adopted for time iterations due to the non-linear IX isotherm. The solution to the non-linear growth equation was computed using a fourth-order Runge-Kutta algorithm. All the simulations were performed using the MATLAB software, version 2016a, and a built-in algorithm ode15, was used to solve the ordinary differential equation describing algal growth.

4.8 References

American Public Health Association. *Standard Methods for the Examination of Water and Wastewater*. 22nd ed.; American Public Health Association, American Water Works, Water Environment Federation: Washington, DC, 2012.

Amini, A.; Aponte-Morales, V.; Wang, M.; Dilbeck, M.; Lahav, O.; Zhang, Q.; Cunningham, J. A.; Ergas, S. J. Cost-effective treatment of swine wastes through recovery of energy and nutrients. *Waste Manage.* **2017**, *69*, (Supplement C), 508-517.

Anthonisen, A. C.; Loehr, R. C.; Prakasam, T. B. S.; Srinath, E. G. Inhibition of Nitrification by Ammonia and Nitrous Acid. *J. Water Pollut. Control Fed.* **1976**, *48*, (5), 835-852.

Aponte-Morales, V. E. Ammonium Removal from High Strength Wastewater Using a Hybrid Ion Exchange Biological Process. Ph.D. Dissertation, University of South Florida, Tampa, FL, 2015.

Aponte-Morales, V. E.; Tong, S.; Ergas, S. J. Nitrogen Removal from Anaerobically Digested Swine Waste Centrate Using a Laboratory-Scale Chabazite-Sequencing Batch Reactor. *Environ. Eng. Sci.* **2016**, *33*, (5), 324-332.

Aponte-Morales, V. E. Ammonium Removal from High Strength Wastewater Using a Hybrid Ion Exchange Biological Process. Ph.D. Dissertation, University of South Florida, Tampa, FL, 2015.

Aponte-Morales, V. E.; Tong, S.; Ergas, S. J. Nitrogen Removal from Anaerobically Digested Swine Waste Centrate Using a Laboratory-Scale Chabazite-Sequencing Batch Reactor. *Environ. Eng. Sci.* **2016**, *33*, (5), 324-332.

Aponte-Morales, V. E.; Payne, K. A.; Cunningham, J. A.; Ergas, S. J. Bioregeneration of Chabazite During Nitrification of Centrate from Anaerobically Digested Livestock Waste: Experimental and Modeling Studies. *Environ. Sci. Technol.* **2018**, 52(7), 4090-4098.

Auerbach, S.M.; Carrado, K.A.; Dutta, P.K. Handbook of zeolite science and technology, CRC press, 2003.

Barber, J.; Shieh, Y.J. Sodium transport in Na⁺-rich *Chlorella* cells. *Planta* **1973** 111(1), 1322.

Becker, E.W. Micro-algae as a source of protein. *Biotechnol. Adv.* **2007** 25(2), 207-210.

Cantrell, K.B.; Ducey, T.; Ro, K.S.; Hunt, P.G. Livestock waste-to-bioenergy generation opportunities. *Bioresour. Technol.* **2008**, 99(17), 7941-7953.

Converti, A.; Casazza, A.A.; Ortiz, E.Y.; Perego, P.; Del Borghi, M. Effect of temperature and nitrogen concentration on the growth and lipid content of *Nannochloropsis oculata* and *Chlorella vulgaris* for biodiesel production. *Chem. Eng. Process: Process Intensification* **2009**, 48(6), 1146-1151.

Crofts, A.R. (1966) Uptake of ammonium ion by chloroplasts, and its relation to photophosphorylation. *Biochem. Biophys. Res. Commun.* **1966**, 24(5), 725-731.

Ergas, S. J.; Aponte-Morales, V. Biological nitrogen removal, 2014.

Fux, C.; Velten, S.; Carozzi, V.; Solley, D.; Keller, J. Efficient and stable nitrification and denitrification of ammonium-rich sludge dewatering liquor using an SBR with continuous loading. *Water Res.* **2006**, 40(14), 2765-2775.

González-Dávila, M. The role of phytoplankton cells on the control of heavy metal concentration in seawater. *Mar. Chem.* **1995**, 48(3), 215-236.

Halfhide, T.; Dalrymple, O.; Wilkie, A.; Trimmer, J.; Gillie, B.; Udom, I.; Zhang, Q.; Ergas, S. Growth of an Indigenous Algal Consortium on Anaerobically Digested Municipal Sludge Centrate: Photobioreactor Performance and Modeling. *Bioener. Res.* **2014**, 1-10.

Hedström, A. Ion Exchange of Ammonium in Zeolites: A Literature Review. *J. Environ. Eng.* **2001**, 127(8), 673-681.

Jorgensen, T.C.; Weatherley, L.R. Ammonia removal from wastewater by ion exchange in the presence of organic contaminants. *Water Res.* **2003**, 37(8), 1723-1728.

Juneja, A.; Ceballos, R.; Murthy, G. Effects of Environmental Factors and Nutrient Availability on the Biochemical Composition of Algae for Biofuels Production: A Review. *Energies* **2013**, 6(9), 4607.

Källqvist, T.; Svenson, A. Assessment of ammonia toxicity in tests with the microalga, *Nephroselmis pyriformis*, Chlorophyta. *Water Res.* **2003**, 37(3), 477-484.

Kim, Y. M.; Park, D.; Lee, D. S.; Park, J. M., Inhibitory effects of toxic compounds on nitrification process for cokes wastewater treatment. *J. Hazard. Mater.* **2008**, 152, (3), 915-921.

Kjeldsen, P.; Barlaz, M.A.; Rooker, A.P.; Baun, A.; Ledin, A.; Christensen, T.H. Present and Long-Term Composition of MSW Landfill Leachate: A Review. *Crit. Rev. Env. Sci. Technol.* **2002**, 32(4), 297-336.

Kotay, S.M.; Mansell, B.L.; Hogsett, M.; Pei, H.; Goel, R. Anaerobic ammonia oxidation (ANAMMOX) for side-stream treatment of anaerobic digester filtrate process performance and microbiology. *Biotechnol. Bioeng.* **2013**, 110(4), 1180-1192.

Krishna, R. and Wesselingh, J.A. The Maxwell-Stefan approach to mass transfer. *Chem. Engin. Sci.* **1997**, 52(6), 861-911.

Lackner, S.; Gilbert, E.M.; Vlaeminck, S.E.; Joss, A.; Horn, H.; van Loosdrecht, M.C.M. Full-scale partial nitrification/anammox experiences – An application survey. *Water Res.* **2014**, 55(Supplement C), 292-303.

Lee, E.; Zhang, Q. Integrated co-limitation kinetic model for microalgae growth in anaerobically digested municipal sludge centrate. *Algal Res.* **2016**, 18, 15-24.

Li, Y.; Chen, Y.-F.; Chen, P.; Min, M.; Zhou, W.; Martinez, B.; Zhu, J.; Ruan, R. Characterization of a microalga *Chlorella* sp. well adapted to highly concentrated municipal wastewater for nutrient removal and biodiesel production. *Bioresour. Technol.* **2012**, 102(8), 5138-5144.

Lin, L.; Chan, G.Y.S.; Jiang, B.L.; Lan, C.Y. Use of ammoniacal nitrogen tolerant microalgae in landfill leachate treatment. *Waste Manage.* **2007**, 27(10), 1376-1382.

Lito, P.F.; Aniceto, J.P.S.; Silva, C.M. Modelling ion exchange kinetics in zeolite-type materials using Maxwell-Stefan approach. *Desalin. Water Treat.* **2014**, 52(28-30), 5333-5342.

Malovanyy, A.; Sakalova, H.; Yatchyshyn, Y.; Plaza, E.; Malovanyy, M. Concentration of ammonium from municipal wastewater using ion exchange process. *Desalination* **2013**, 329(0), 93-102.

Martins, T.H.; Souza, T.S.O.; Foresti, E. Ammonium removal from landfill leachate by Clinoptilolite adsorption followed by bioregeneration. *J. Environ. Chem. Engin.* **2017**, 5(1), 63-68.

Park, J.; Jin, H.-F.; Lim, B.-R.; Park, K.-Y.; Lee, K. Ammonia removal from anaerobic digestion effluent of livestock waste using green alga *Scenedesmus* sp. *Bioresour. Tech* **2010**, 101(22), 8649-8657.

Rožić, M.; Cerjan-Stefanović, Š.; Kurajica, S.; Vančina, V.; Hodžić, E. Ammoniacal nitrogen removal from water by treatment with clays and zeolites. *Water Res.* **2000**, 34(14), 3675-3681.

Rusten, B.; Sahu, A.K. Microalgae growth for nutrient recovery from sludge liquor and production of renewable bioenergy. *Water Sci. Technol.* **2011**, 64(6), 1195-1201.

Schaedle, M.; Jacobson, L. Ion absorption and retention by *Chlorella pyrenoidosa*. III. Selective accumulation of rubidium, potassium and sodium. *Plant Physiol.* **1967**, 42(7), 953-958.

Shifrin, N.S.; Chisholm, S.W. Phytoplankton lipids: interspecific differences and effects of nitrate, silicate and light-dark cycles. *J. Phycol.* **1981**, 17(4), 374-384.

Solovchenko, A.E.; Khozin-Goldberg, I.; Didi-Cohen, S.; Cohen, Z.; Merzlyak, M.N. Effects of light intensity and nitrogen starvation on growth, total fatty acids and arachidonic acid in the green microalga *Parietochloris incisa*. *J. Appl. Phycol.* **2008**, 20(3), 245-251.

Sukenik, A.; Livne, A. Variations in lipid and fatty acid content in relation to acetyl CoA carboxylase in the marine prymnesiophyte *Isochrysis galbana*. *Plant Cell Physiol.* **1991**, 32(3), 371-378.

Suresh Kumar, K.; Dahms, H.-U.; Won, E.-J.; Lee, J.-S.; Shin, K.-H. Microalgae – A promising tool for heavy metal remediation. *Ecotoxicol. Environ. Saf.* 13(Supplement C), **2015**, 329-352.

Tada, C.; Yang, Y.; Hanaoka, T.; Sonoda, A.; Ooi, K.; Sawayama, S. Effect of natural zeolite on methane production for anaerobic digestion of ammonium rich organic sludge. *Bioresour. Technol.* **2015**, 96(4), 459-464.

Third, K.A.; Paxman, J.; Schmid, M.; Strous, M.; Jetten, M.S.M.; Cord-Ruwisch, R. Treatment of nitrogen-rich wastewater using partial nitrification and Anammox in the CANON process. *Water Sci Technol.* **2005**, 52(4), 47-54.

Udert, K.M.; Fux, C.; Münster, M.; Larsen, T.A.; Siegrist, H.; Gujer, W. Nitrification and autotrophic denitrification of source-separated urine. *Water Sci Technol.* **2003**, 48(1), 119-130.

Wang, H.; Xiong, H.; Hui, Z.; Zeng, X. Mixotrophic cultivation of *Chlorella pyrenoidosa* with diluted primary piggy wastewater to produce lipids. *Bioresour. Technol.* **2012**, 104(Supplement C), 215-220.

Wang, L.; Li, Y.; Chen, P.; Min, M.; Chen, Y.; Zhu, J.; Ruan, R.R. Anaerobic digested dairy manure as a nutrient supplement for cultivation of oil-rich green microalgae *Chlorella* sp. *Bioresour. Technol.* **2010**, 101(8), 2623-2628.

Wang, M.; Park, C. Investigation of anaerobic digestion of *Chlorella* sp. and *Micractinium* sp. grown in high-nitrogen wastewater and their co-digestion with waste activated sludge. *Biomass Bioenergy* **2015**, 80, 30-37.

Wang, M.; Yang, H.; Ergas, S.J.; van der Steen, P. A novel shortcut nitrogen removal process using an algal-bacterial consortium in a photo-sequencing batch reactor (PSBR). *Water Res.* **2015**, 87, 38-48.

Wang, S.; Peng, Y. Natural zeolites as effective adsorbents in water and wastewater treatment. *Chem. Eng. J.* **2010**, 156(1), 11-24.

Wang, X.-X.; Wu, Y.-H.; Zhang, T.-Y.; Xu, X.-Q.; Dao, G.-H.; Hu, H.-Y. Simultaneous nitrogen, phosphorous, and hardness removal from reverse osmosis concentrate by microalgae cultivation. *Water Res.* **2016**, 94(Supplement C), 215-224.

Wett, B.; Alex, J. Impacts of separate rejection water treatment on the overall plant performance. *Water Sci. Technol.* **2015**, 48(4), 139-146.

Yuan, X.; Wang, M.; Park, C.; Sahu, A.K.; Ergas, S.J. Microalgae Growth Using High-Strength Wastewater Followed by Anaerobic Co-Digestion. *Water Environ. Res.* **2012**, 84(5), 396-404.

CHAPTER 5:

MODELING OF MASS TRANSPORT AND BIODEGRADATION IN A HYBRID ADSORPTION AND MIXOTROPHIC DENITRIFICATION BIOREACTOR

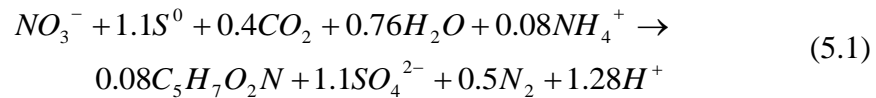
5.1 Introduction

In the US, approximately 25% of the wastewater generated is treated by decentralized treatment systems (Lowe and Siegrist, 2008). The most common decentralized systems are conventional onsite wastewater treatment systems (OWTS), which are comprised of a septic tank, drainfield, and soil treatment area. These systems were originally intended to serve rural and suburban communities where access to sewer connections was not a viable option. While there are several advantages of conventional OWTS, including simplicity of operation and low cost relative to centralized systems, major challenges persist related to nitrogen (N) removal (USEPA, 1999 ; Siegrist et al., 2013). Environmental risks stemming from these challenges include contamination of surface and groundwater bodies (Howe et al., 2012).

Advanced treatment systems have been proposed for enhancing N removal in OWTS, with the goal of enabling groundwater recharge, safe disposal, and reuse options (Siegrist et al., 2013). Environmental biotechnologies for advanced onsite treatment include moving bed bioreactors and membrane bioreactors. However, these technologies are associated with relatively high energy costs and maintenance requirements (Diaz-Elsayed, 2017). Therefore, passive OWTS have been developed that require minimally skilled operations and maintenance interventions by the end user or septic tank installer (e.g., Smith et al., 2008). Passive OWTS typically are implemented in a packed-bed bioreactor configuration, utilize reactive media for denitrification, require no

mechanical aeration, and utilize a single pump (FDOH, 2013). Although passive OWTS demonstrate potential in terms of N removal, several outstanding knowledge gaps remain pertaining to how the confluence of hydrodynamic, physical, chemical, and biological factors affect their treatment efficacy.

Advanced treatment within passive bioreactors typically occurs in two stages: a bioreactor operating under partially saturated conditions for nitrification, followed by treatment in a fully saturated bioreactor for denitrification. Biological denitrification of nitrified wastewater requires an electron donor. Passive bioreactors containing lignocellulosic materials that slowly release organic carbon to support heterotrophic denitrifying biofilm growth are one approach for denitrification (Lopez-Ponnada et al., 2017). An alternative approach to heterotrophic denitrification is sulfur-oxidizing denitrification (SOD), which utilizes elemental sulfur (S^0) as the electron donor for autotrophic denitrification. This process has been shown to achieve high NO_3^- -N removal rates and, low costs, as well as lower sludge production and lower maintenance requirements than heterotrophic denitrification (Sengupta et al., 2007). The reduction of NO_3^- -N to N_2 and conversion of S^0 to SO_4^{2-} -S catalyzed by sulfur-oxidizing denitrifying bacteria is given by (Batchelor and Lawrence, 1978):



While there are several advantages of SOD, potential drawbacks include the consumption of alkalinity and SO_4^{2-} production. The production of SO_4^{2-} can pose aesthetic effects, if an OWTS recharges groundwater used as a potable water source (USEPA, 2008). Since inhibition of denitrification can occur below a pH of 5.5, solid-phase buffers are typically used for imparting alkalinity to bioreactors in OWTS (Sengupta et al., 2007). It has been shown previously that

crushed oyster shell was a more suitable buffer than marble chips or limestone, based on factors including the buffer's dissolution rate, the suitability of the buffer's surface for supporting microbial attachment, and economics (Sengupta et al., 2007).

Prior studies at the University of South Florida reported the results of a novel tire-sulfur hybrid adsorption denitrification (T-SHAD) process for removal of NO_3^- -N in OWTS (Krayzelova et al., 2014). The T-SHAD process utilizes mixotrophic denitrification, which combines the processes of heterotrophic and autotrophic denitrification (Sahinkaya, 2012). The benefits include lower SO_4^{2-} -S production and alkalinity consumption than SOD by itself, as well as consistent performance under transient loading conditions. While experimental studies have been performed, mathematical and numerical models have not previously been developed to elucidate the effluent characteristics of the T-SHAD process under varying influent flow conditions. The development of such models would not only provide an understanding of the role of various mechanisms but would also be critical in facilitating optimal design of the denitrification stage of full-scale OWTS.

The literature on mathematical modeling of adsorption onto granular activated carbon and biodegradation in packed-bed bioreactors provides many commonalities with the T-SHAD model developed (Shen et al., 2012). For example, a model was developed to investigate the processes of adsorption and biodegradation in a packed-bed of granular activated carbon for degradation of phenol (Speitel Jr. et al., 1987). The model treated the aqueous and biofilm phases as continua and accounted for film transport resistance, biofilm growth, and decay. However, mass transfer resistance was ignored at the interface between the solid and biofilm. The adsorption phenomenon used a surface diffusion model with the Freundlich isotherm at the particle surface. More mathematically advanced approaches have arisen in recent times to describe processes in biofilters, and a comprehensive review of a broad spectrum of modeling approaches for biofilm-covered

activated carbon systems can be found elsewhere (Shen et al., 2012). Integral aspects highlighted in the review of Shen et al., (2012) were the mathematical description of the solid phase, biofilm phase on the substratum, and the liquid phase.

In this Chapter, a novel mathematical and numerical model that provides a framework for modeling environmental biotechnologies involving flow, mass transport, and mixotrophic denitrification processes in a packed-bed bioreactor is developed. The objectives of this Chapter are: (1) to develop a mathematical model that accounts for advection, dispersion, and mixotrophic denitrification under varying influent flow conditions; (2) to estimate all model parameters via literature values or results of previously performed experiments; and (3) to validate the model via comparison of the simulated effluent concentrations to experimental results.

5.2 Materials and Methods

5.2.1 Batch and Column Experiments

Details of the batch and column studies previously conducted within our research group are described elsewhere (Krayzelova et al., 2014). Briefly, batch abiotic NO_3^- adsorption and denitrification microcosm studies were performed. The NO_3^- adsorption study was performed in triplicate using scrap tire doses of 0, 2.5, 5, 10, 20, 30, and 40 g. The scrap tires were placed in 250-mL glass Erlenmeyer flasks, which were filled with 200 mL of a synthetic wastewater solution (see supplementary information [SI]). The synthetic wastewater solution contained KNO_3 to achieve an initial NO_3^- -N concentration of 100 mg L^{-1} . The bottles were placed on a Thermo Scientific multi-purpose rotator (Dubuque, Iowa, U.S.A) at 120 rpm. Samples were collected every ten days over a 30-day period and analyzed for anion and cation concentrations using an 850 Professional Ion Chromatography System (Metrohm AG, Herisau, Switzerland).

Four different denitrification microcosm studies were performed in triplicate, using 160 mL glass serum bottles containing 90 mL of a synthetic wastewater solution. The SOD microcosms

included 6 g of elemental sulfur and 2 g crushed oyster shells; the scrap tire chip microcosms included 10 g of tire chips; the T-SHAD microcosms contained 10 g of tire chips, 6 g of elemental sulfur, and 2 g of crushed oyster shells; the fourth set of microcosms consisted of synthetic wastewater and activated sludge, but no sulfur or tire chips, to control for endogenous decay. The inoculum used in each microcosm was 10 mL of activated sludge with a mixed liquor suspended solids concentration of 2.69 g L^{-1} . The activated sludge was obtained from the Northwest Regional Wastewater Reclamation Facility, Hillsborough County, Florida, which utilizes a 5-stage Bardenpho process. The wastewater solution used for each microcosm was spiked with a KNO_3 solution to achieve an initial NO_3^- -N concentration of 50 mg L^{-1} .

For column experiments, two 0.5 L acrylic Koflo columns (Cary, Illinois) were used in an upflow configuration (Figure 5.1), with an influent wastewater composition as shown in Table 5.1 pumped through the bottom of the columns. The media in the T-SHAD column were homogenously mixed and consisted of 250 g of scrap tire chips, 40 g of elemental sulfur pellets, and 13 g of crushed oyster shell, whereas the column strictly with tire chips consisted of 250 g of scrap tire chips. The T-SHAD column experiment was performed in four different phases. Phase 1 (20 d) was an acclimation period to allow for attachment and growth of a denitrifying biofilm. Phase 2 (46d) was a period with steady flow and a constant influent concentration of 50 mg L^{-1} NO_3^- -N. During Phase 3 (13 d) the influent NO_3^- -N was set to a constant value of 50 mg L^{-1} but the flow rate was varied to mimic transient inflow conditions of a household. Finally, Phase 4 conditions were a constant flow rate and transient influent NO_3^- -N concentrations. The tire-chip-only column was operated for Phase 1 and Phase 2 but then discontinued due to the low removal efficiency of NO_3^- -N observed.

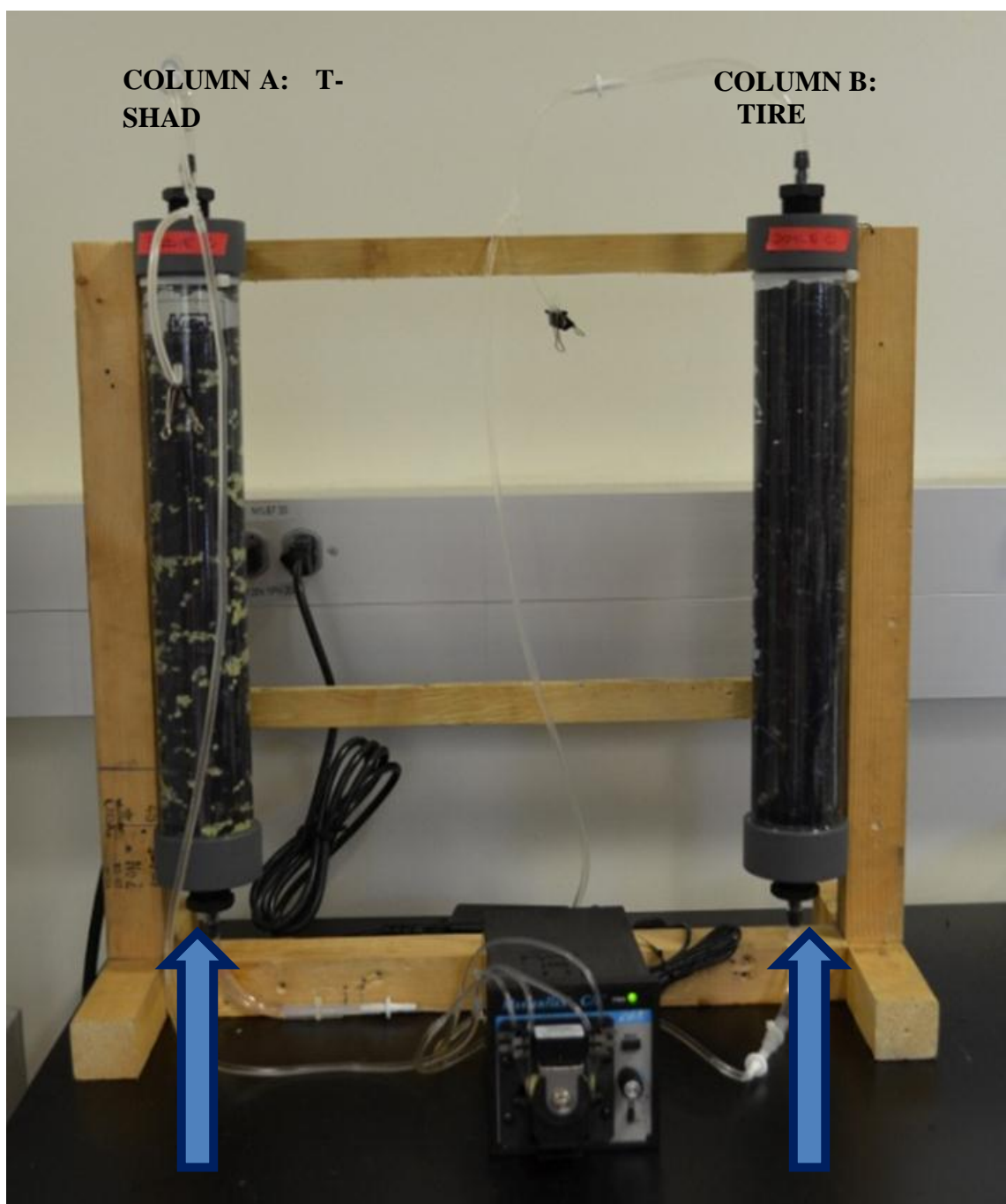


Figure 5.1: Column A shows the T-SHAD column and column B shows the tire-only-column. Blue arrows indicate the direction of flow (Krayzelova et al., 2014).

**Table 5.1: Composition of wastewater used in T-SHAD experiments
(from Krayzelova et al., 2014)**

Chemical constituent	Concentration (mg L⁻¹)
KH ₂ PO ₄	43.9
NH ₄ Cl	7.6
MgCl ₂ .6H ₂ O	33.0
FeCl ₂ .4H ₂ O	0.4
NaHCO ₃	50.0
ZnCl ₂	0.0189
EDTA	0.576
CaCl ₂ .2H ₂ O	0.07
MnCl ₂ .4H ₂ O	0.0472
(NH ₄) ₆ Mo ₇ O ₂₄ .4H ₂ O	0.01
CuSO ₄ .5H ₂ O	0.0281
CoCl ₂ .6H ₂ O	0.02
NO ₃ ⁻ -N	100.0

5.3 Mathematical Model Development

In the aqueous phase, there are generally two approaches for modeling flow and mass transport. In one approach, an advection-dispersion-reaction equation is adopted, whereby the reaction term is a rate expression describing the kinetics of biodegradation. However, it has been noted previously that conceptually, this type of mathematical model describes biofilm processes as occurring within the aqueous phase, although biodegradation explicitly occurs within the biofilm phase (Cunningham and Mendoza-Sanchez, 2006). An alternative and more physically consistent conceptual approach is to model advection and dispersion in the aqueous phase and couple the partial differential equation (PDE) for that process to a diffusion-reaction equation representing biodegradation within a biofilm. However, a comparison between these two approaches referred to as the “simple” and “biofilm” models showed that they provide identical results except for scenarios when biological reactions within the biofilm are slow relative to other mass transport mechanisms (Cunningham and Mendoza-Sanchez, 2006). Given the similarity in breakthrough behavior previously theoretically obtained for both approaches as well as the lower

computing time requirement for the “simple” model, a mathematical model was the T-SHAD model adopted an approach that considers advection-dispersion-reaction in the bulk liquid. Figure 5.2 is a conceptual image of the T-SHAD column, in which the following processes occur: mass transport by advection and dispersion, and mixotrophic biological denitrification. The assumptions are given as follows:

1. Flow and mass transport occur vertically upward and are one-dimensional.
2. The solid- phase uptake process onto tire chips is a slow process relative to mass transport and biological mechanisms, therefore is ignored for the time-period simulated (24 h).
3. Sulfur-oxidizing and heterotrophic denitrifying microorganisms mediate biological denitrification. In this Chapter, the nomenclature adopted to define the combination of these processes is mixotrophic denitrification.
4. The rate of substrate utilization is dependent on the electron acceptor (NO_3^-) and is described using a Monod model.
5. A single-step model for biological denitrification from NO_3^- to N_2 is assumed, whereby the conversion of NO_3^- to NO_2^- is ignored given that no significant accumulation of the intermediate chemical species was observed from at the T-SHAD column outlet.
6. The influent velocity varies with time, so that the dimensionless groups characterizing the T-SHAD bioreactor vary accordingly.

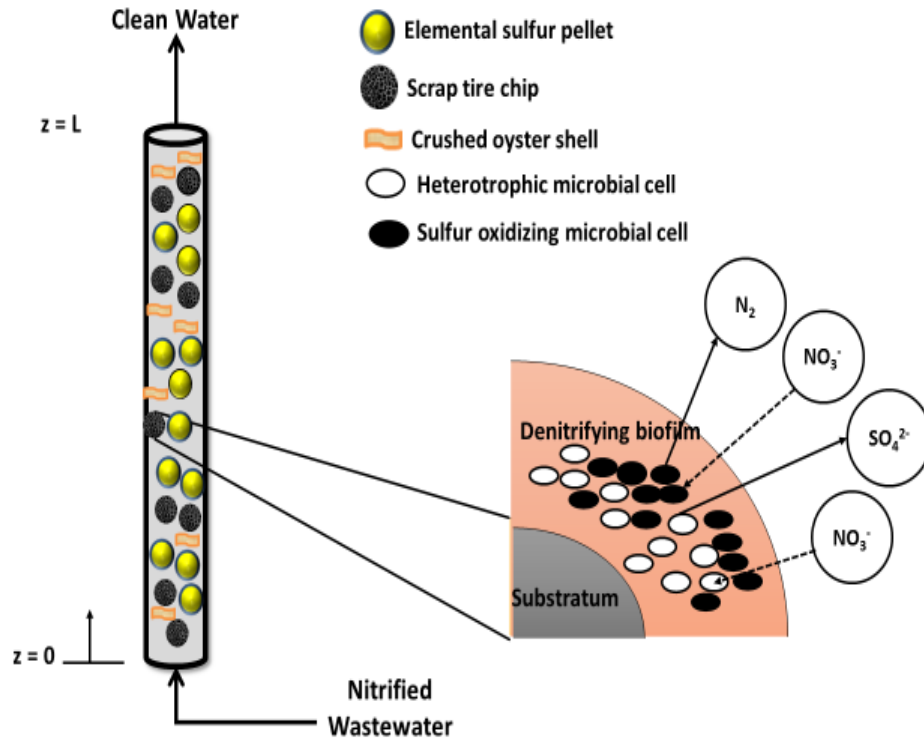


Figure 5.2: Conceptualization of major processes occurring within the T-SHAD bioreactor

5.3.1 Mass Transport Processes

Here, the T-SHAD model equations are presented in dimensionless form, adopting non-dimensionalization to reduce the number of model parameters and to facilitate the assessment of the T-SHAD bioreactor breakthrough characteristics under various limiting regimes. Table 5.2 provides definitions for each of the dimensionless variables and groups in the T-SHAD model.

The migration of chemical species in saturated porous media is controlled by advection, dispersion, and reactions occurring due to utilization by denitrifying microorganisms. Thus, the mathematical expression for the NO_3^- -N concentration in the aqueous phase is given by:

$$\begin{aligned}
\frac{\partial \bar{C}_{NO_3^-}(\bar{z}, \bar{t})}{\partial \bar{t}} = & \frac{1}{Pe_{NO_3^-}} \frac{\partial^2 \bar{C}_{NO_3^-}(\bar{z}, \bar{t})}{\partial \bar{z}^2} - \frac{\partial \bar{C}_{NO_3^-}(\bar{z}, \bar{t})}{\partial \bar{z}} \\
& - Da_{HET} \left(\frac{\bar{C}_{NO_3^-}(\bar{z}, \bar{t})}{\bar{C}_{NO_3^-}(\bar{z}, \bar{t}) + \gamma_{HET}} \right) - Da_{SOD} \left(\frac{\bar{C}_{NO_3^-}(\bar{z}, \bar{t})}{\bar{C}_{NO_3^-}(\bar{z}, \bar{t}) + \gamma_{SOD}} \right)
\end{aligned} \tag{5.2}$$

where $\bar{C}_{NO_3^-}(\bar{z}, \bar{t})$ is the dimensionless NO_3^- -N concentration in the liquid phase, Da_{HET} is the Damköhler utilization number for heterotrophic bacteria, Da_{SOD} is the Damköhler utilization number for SOD, $Pe_{NO_3^-}$ is the Peclet number for NO_3^- , \bar{t} is dimensionless time, \bar{z} is the dimensionless axial coordinate, γ_{HET} is the ratio between the half saturation constant for heterotrophic bacteria and the initial influent concentration, γ_{SOD} is the ratio between the half saturation constant for SOD and initial influent concentration.

Table 5.2: Definition of non-dimensional variables and dimensionless groups characterizing the T-SHAD system

Dimensionless variable/group	Equation	Definition
$\bar{C}_{NO_3^-}$	$\bar{C}_{NO_3^-} = \frac{C}{C_{0,NO_3^-}}$	Non-dimensional concentration of NO_3^- -N in the bulk liquid
$\bar{C}_{SO_4^{2-}}$	$\bar{C}_{SO_4^{2-}} = \frac{C}{C_{0,SO_4^{2-}}}$	Non-dimensional concentration of SO_4^{2-} -S in the bulk liquid
\bar{t}	$\bar{t} = \frac{tv}{L}$	Non-dimensional time indicating the number of pore volumes in the column
\bar{z}	$\bar{z} = \frac{z}{L}$	Non-dimensional distance along the characteristic length
Da_{HET}	$\frac{\hat{q}_{HET} X_{HET}}{C_{0,NO_3^-} v / L}$	Damköhler utilization number for heterotrophic bacteria: ratio of maximum utilization rate by heterotrophic bacteria to rate of advection in the bulk liquid
Da_{SOD}	$\frac{\hat{q}_{SOD} X_{SOD}}{C_{0,NO_3^-} v / L}$	Damköhler utilization number for SOD: ratio of maximum utilization rate by sulfur oxidizing bacteria to rate of advection in the bulk liquid
$Pe_{NO_3^-}$	$\frac{vL}{D_{NO_3^-}}$	Peclet number for NO_3^- : ratio of advective transport in the bulk liquid to dispersive transport
$Pe_{SO_4^{2-}}$	$\frac{vL}{D_{SO_4^{2-}}}$	Peclet number for SO_4^{2-} : ratio of advective transport in the bulk liquid to dispersive transport
γ_{HET}	$\gamma_{HET} = \frac{K_{S,HET}}{C_{0,NO_3^-}}$	Ratio between the Monod half saturation constant for heterotrophs and the initial concentration
γ_{SOD}	$\gamma_{SOD} = \frac{K_{S,SOD}}{C_{0,NO_3^-}}$	Ratio between the Monod half saturation constant for SOD and the initial concentration

Similarly, the equation governing mass transport for the SO_4^{2-} concentration in the liquid phase is given by:

$$\frac{\partial \bar{C}_{SO_4^{2-}}(\bar{z}, \bar{t})}{\partial \bar{t}} = \frac{1}{Pe_{SO_4^{2-}}} \frac{\partial^2 \bar{C}_{SO_4^{2-}}(\bar{z}, \bar{t})}{\partial \bar{z}^2} - \frac{\partial \bar{C}_{SO_4^{2-}}(\bar{z}, \bar{t})}{\partial \bar{z}} + \beta_{SOD} Da_{SOD} \left(\frac{\bar{C}_{NO_3^-}(\bar{z}, \bar{t})}{\bar{C}_{NO_3^-}(\bar{z}, \bar{t}) + \gamma_{SOD}} \right) \quad (5.3)$$

where $\bar{C}_{SO_4^{2-}}(\bar{z}, \bar{t})$ is the dimensionless SO_4^{2-} -S concentration in the liquid phase, $Pe_{SO_4^{2-}}$ is the Peclet number for SO_4^{2-} , and β_{SOD} is a stoichiometric constant relating NO_3^- -N consumed to SO_4^{2-} -S produced during the SOD process (Equation 5.1).

5.3.2 Initial and Boundary Conditions

The initial conditions and boundary conditions were specified to mimic the experimental configuration (Figure 5.3). In the aqueous phase, the NO_3^- -N and SO_4^{2-} -S concentrations were initialized to the observed effluent concentrations from Phase 2, so that the initial condition can be written as:

$$\begin{aligned} \bar{C}_{NO_3^-}(\bar{z}, \bar{t} = 0) &= C_{0,NO_3^-} \\ \bar{C}_{SO_4^{2-}}(\bar{z}, \bar{t} = 0) &= C_{0,SO_4^{2-}} \end{aligned} \quad (5.4)$$

At the biofilter inlet there is a continuous source of nitrified wastewater:

$$\begin{aligned} \bar{C}_{NO_3^-}(\bar{z} = 0, \bar{t}) - \frac{1}{Pe_{NO_3^-}} \frac{\partial \bar{C}_{NO_3^-}(\bar{z} = 0, \bar{t})}{\partial \bar{z}} &= 1 \\ \bar{C}_{SO_4^{2-}}(\bar{z} = 0, \bar{t}) - \frac{1}{Pe_{SO_4^{2-}}} \frac{\partial \bar{C}_{SO_4^{2-}}(\bar{z} = 0, \bar{t})}{\partial \bar{z}} &= 1 \end{aligned} \quad (5.5)$$

At the column outlet there is no dispersive flux:

$$\begin{aligned} \frac{\partial \bar{C}_{NO_3^-}(\bar{z} = 1, \bar{t})}{\partial \bar{z}} &= 0 \\ \frac{\partial \bar{C}_{SO_4^{2-}}(\bar{z} = 1, \bar{t})}{\partial \bar{z}} &= 0 \end{aligned} \quad (5.6)$$

The T-SHAD simulations were set-up to mimic the operation of the system, whereby at the inlet flow varies temporally to reflect changes typically observed in full-scale OWTS over a

daily period. Since the influent velocity is temporally variable, the Damköhler utilization number and Peclet groups, which are functions of velocity, were varied accordingly. Figure 5.3 shows the experimental configuration for three phases of the experiment. It should be noted that the third phase of the experiment was simulated to capture a 24-hour period during which the influent NO_3^- -N concentration was constant, and the effluent concentration was varied.

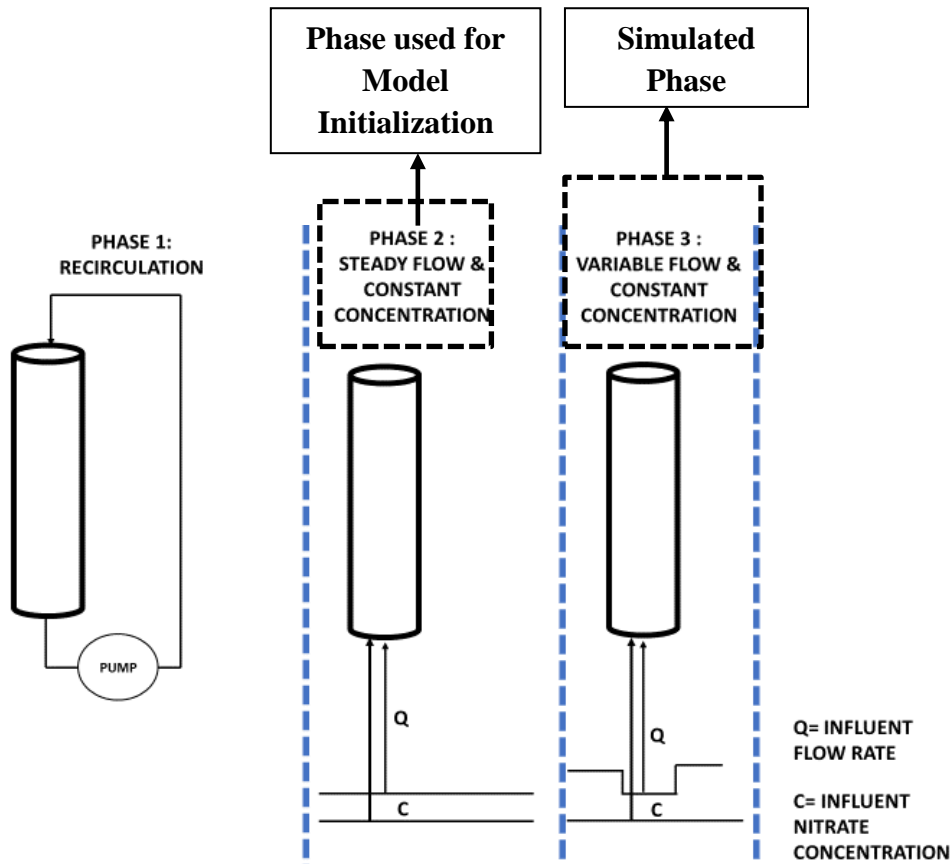


Figure 5.3: Phases of the experiment simulated and used for model initialization

5.4 Numerical Approach

The “pdepe” function in the MATLAB software was used for the numerical solution of the system of equations representing the T-SHAD system. The function solves one-dimensional parabolic and elliptic partial differential equations (PDEs) of the form:

$$c\left(z, t, u, \frac{u}{z}\right) \frac{\partial u}{\partial t} = z^{-m} \frac{\partial}{\partial z} z^m f\left(z, t, u, \frac{u}{z}\right) + s\left(z, t, u, \frac{u}{z}\right) \quad (5.7)$$

$$t_0 \leq t \leq t_n$$

$$a \leq z \leq b$$

where u is the vector of unknown variables, c is a diagonal matrix with coefficients of time derivatives, $f\left(z, t, u, \frac{u}{z}\right)$ is a flux term and $s\left(z, t, u, \frac{u}{z}\right)$ is a source/sink term. The term m takes strictly integer values 0, 1, and 2, representing cartesian, cylindrical, and spherical symmetry respectively, t_0 is the initial time of the simulation period, t_n is the final time of the simulation period, a and b correspond the end-points of the domain considered.

For some initial time, t_0 , the solution components satisfy the initial conditions:

$$u(z, t_0) = u_0(z) \quad (5.8)$$

The boundary condition imposed on the boundaries a and b is expressed as:

$$p(z, t, u) + q(z, t) f\left(z, t, u, \frac{u}{z}\right) = 0 \quad (5.9)$$

The numerical approximation uses a Petrov-Galerkin method for discretization of spatial derivatives and a vertical method of lines for the time derivatives (Skeel and Berzins, 1990). The pdepe formulation of the T-SHAD model as represented by Equations 5.1-5.6 is provided as follows. The term m was set to 0 to model a domain in cartesian coordinates, the diagonal matrix, flux term, and source/sink terms were specified as follows:

$$\left\{ \begin{array}{l} c = \begin{pmatrix} 1 & 0 \\ 0 & 1 \end{pmatrix} \\ u = \begin{pmatrix} \bar{C}_{NO_3^-} \\ \bar{C}_{SO_4^{2-}} \end{pmatrix} \\ f = \begin{pmatrix} \frac{1}{Pe_{NO_3^-}} * \frac{\partial \bar{C}_{NO_3^-}}{\partial \bar{z}} - \bar{C}_{NO_3^-} \\ \frac{1}{Pe_{SO_4^{2-}}} * \frac{\partial \bar{C}_{SO_4^{2-}}}{\partial \bar{z}} - \bar{C}_{NO_3^-} \end{pmatrix} \\ s = \begin{pmatrix} -Da_{HET} \left[\frac{\bar{C}_{NO_3^-}}{C_{NO_3^-} + \gamma_{HET}} \right] - Da_{SOD} \left[\frac{\bar{C}_{NO_3^-}}{C_{NO_3^-} + \gamma_{SOD}} \right] \\ \beta_{SOD} Da_{SOD} \left[\frac{\bar{C}_{NO_3^-}}{C_{NO_3^-} + \gamma_{SOD}} \right] \end{pmatrix} \end{array} \right\} \quad (5.10)$$

5.5 Estimation of Model Parameters

The same dispersive effects were assumed for NO_3^- and SO_4^{2-} and estimated using the following empirical equation for the dispersion coefficient (Bear, 1972):

$$D_{NO_3^-} = D_{SO_4^{2-}} = \tau D_m + \alpha_L v \quad (5.11)$$

where D_m is the molecular diffusion coefficient ($m^2 \text{ hr}^{-1}$), v ($m \text{ hr}^{-1}$) is the average linear fluid velocity, τ is the tortuosity factor in the bioreactor interstitial space (dimensionless), and α_L (m) is the axial dispersivity. Considering mechanical dispersion as the dominant mechanism relative to molecular diffusion, we use an empirical formula to estimate the longitudinal dispersivity (Fetter et al., 2017):

$$\alpha_L = 0.83 \log(L)^{2.414} \quad (5.12)$$

Data from a SOD microcosm were used to determine an effective rate constant for sulfur-oxidizing denitrification, $\hat{q}_{SOD}X_{SOD}$ (gVSS m⁻³ hr⁻¹), and the half saturation constant $K_{S, SOD}$ (g m⁻³). The Monod rate expression in Equation 5.3, which is the second term on the right side of the equation, was used to simulate the NO₃⁻-N concentration history shown in Figure 5.4. The effects due to biomass growth were ignored due to the time-scale for cell division of denitrifying bacteria compared to the study period of the experiment. The SO₄²⁻-S production over time for the first phase of the experiment (Figure 5.4) was simulated by multiplying the rate expression for the consumption of NO₃⁻-N by a stoichiometric constant ($\beta_{SOD} = 2.5$).

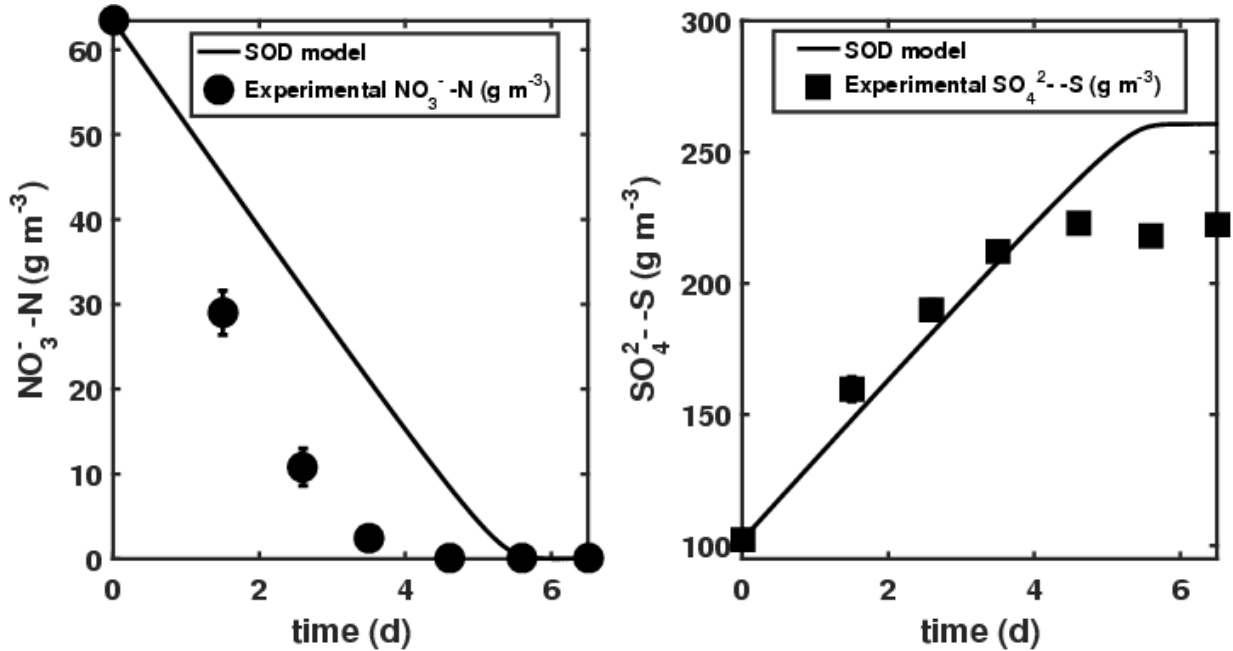


Figure 5.4: Mathematical model and experimental data for NO₃⁻-N consumption and SO₄²⁻-S production for an SOD microcosm over a 6.5-day period

The parameter values required to fit the concentration histories of the experiment were $K_{S, SOD} = 1.3$ g m⁻³ and $\hat{q}_{SOD}X_{SOD} = 0.52$ gVSS m⁻³ hr⁻¹. The model captures the trend of the experimental data as shown by the decrease in the NO₃⁻-N over the 5-day period of the simulation

from an initial value of 63.4 g m^{-3} to almost no $\text{NO}_3^- \text{-N}$ at day 5. In correspondence with the decreasing $\text{NO}_3^- \text{-N}$ concentration, simulation results for $\text{SO}_4^{2-} \text{-S}$ showed an increase from 102.2 g m^{-3} $\text{SO}_4^{2-} \text{-S}$ to approximately 260 g m^{-3} $\text{SO}_4^{2-} \text{-S}$. In addition, the simulation showed that once the $\text{NO}_3^- \text{-N}$ was consumed no more $\text{SO}_4^{2-} \text{-S}$ was produced. It should be noted that the model underestimates the $\text{NO}_3^- \text{-N}$ concentration and slightly overestimates the $\text{SO}_4^{2-} \text{-S}$ experimental data. Increasing the effective rate constant would improve the correspondence between the model and experimental $\text{NO}_3^- \text{-N}$ data, however this would result in an increased discrepancy in the $\text{SO}_4^{2-} \text{-S}$ model and observations due to a greater production of $\text{SO}_4^{2-} \text{-S}$. In addition, the model does not account for organic matter in the oyster shells, which may have contributed to heterotrophic denitrification.

5.6 Results and Discussion

Figure 5.5 shows the simulated effluent $\text{NO}_3^- \text{-N}$ concentration of the column compared to the experimental data under varying influent flow conditions. The model shows that periods with higher influent flow rates, which correspond to shorter residence times, result in an increase in effluent $\text{NO}_3^- \text{-N}$ concentrations. These periods of higher influent flow rates, which occurred during 8-12 hours and 20-24 hours, were simulated by changing the velocity accordingly which decreases the Damköhler utilization number by a factor of 1.5 relative to the medium flow rate period, based on the definition of this dimensionless group (Table 5.2). This resulted in an accumulation of $\text{NO}_3^- \text{-N}$ due to less contact time for treatment to occur in the bioreactor. In contrast, during the period with the longest residence time (12-20 hours) the velocity decreased which resulted in an increase in the Damköhler utilization number by a factor of 2 relative to the medium flow rate period, resulting in the greatest decrease in $\text{NO}_3^- \text{-N}$ due to the longer period for biological denitrification to occur. Moreover, it should be noted that the model semi-quantitatively

captures the transient behavior when velocity changes during the simulation by correctly predicting approximately 90% removal of the constant influent $50 \text{ g m}^{-3} \text{ NO}_3^- \text{-N}$.

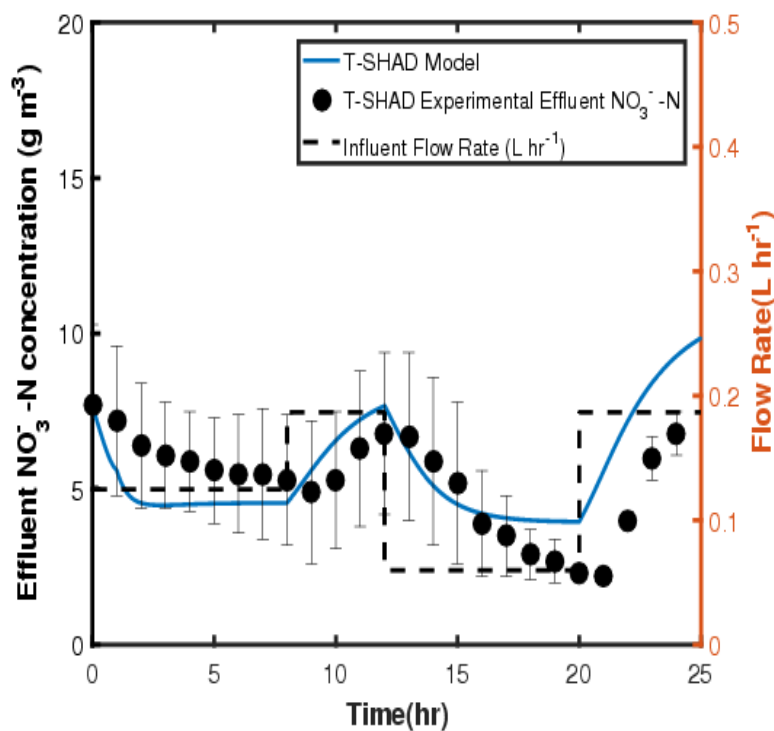


Figure 5.5: Mathematical model and experimental data for $\text{NO}_3^- \text{-N}$ from effluent of the T-SHAD column

Figure 5.6 shows the simulated effluent $\text{SO}_4^{2-} \text{-S}$ concentration of the column compared to the experimental data. During periods with the shortest residence time (8-12 hours and 20-24 hours), the model captures the decrease in the effluent $\text{SO}_4^{2-} \text{-S}$ concentration. This behavior is consistent with less time for SOD to occur and thus less $\text{SO}_4^{2-} \text{-S}$ produced as a by-product relative to periods with longer residence times. Conversely, the period from 12-20 hours showed the highest production of $\text{SO}_4^{2-} \text{-S}$, which corresponds with the lowest fluid velocity. During this period, there was more time for SOD to occur, therefore more production of $\text{SO}_4^{2-} \text{-S}$ as a by-product. The lack of incorporation of the dissolution rates of the electron donors could be one source of the discrepancy between the model and experimental data, particularly during the first

10 hours of the simulation. Accounting for dissolution processes and adsorption onto tire chips would likely improve the model correspondence with experimental data.

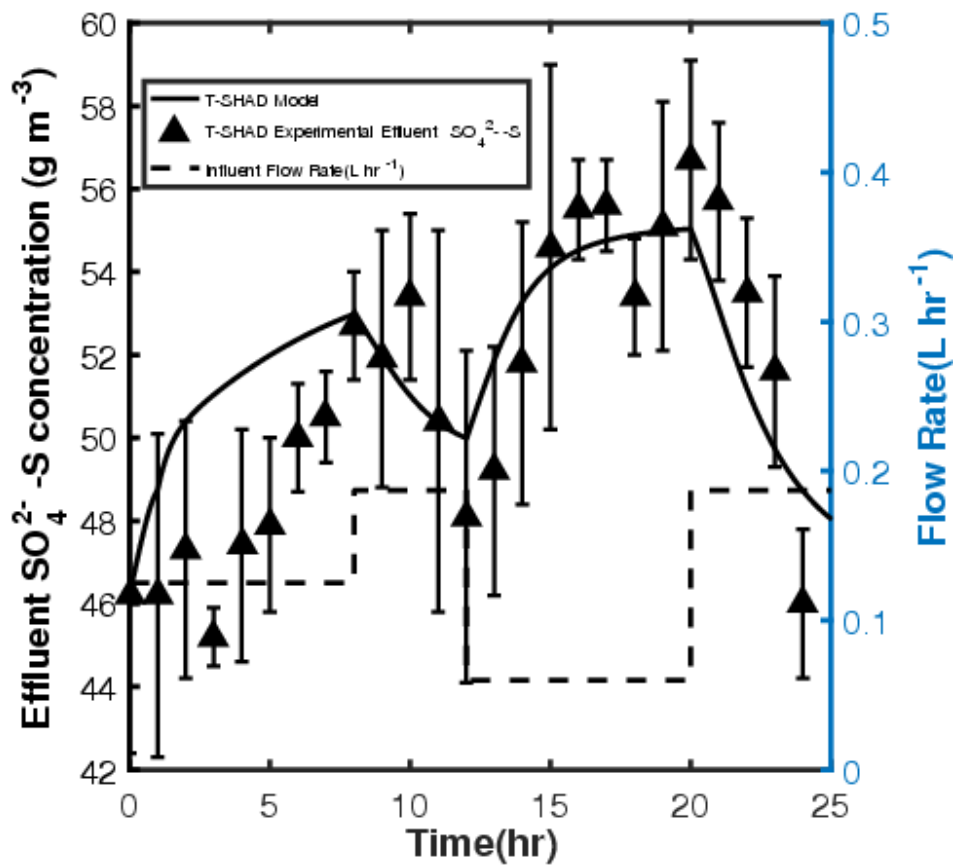


Figure 5.6: Mathematical model and experimental data for SO_4^{2-} - S from effluent of the T-SHAD column

Table 5.3: Definition of parameters appearing in dimensionless numbers

Parameter	Value	Source
$D_{NO_3^-}$	$4.15 \times 10^{-6} \text{ m}^2 \text{ hr}^{-1}$ (low flow) $8.3 \times 10^{-6} \text{ m}^2 \text{ hr}^{-1}$ (medium flow) $8.3 \times 10^{-6} \text{ m}^2 \text{ hr}^{-1}$ (high flow)	Empirically obtained (Fetter, 2017)
$D_{SO_4^{2-}}$	$4.15 \times 10^{-6} \text{ m}^2 \text{ hr}^{-1}$ (low flow) $8.3 \times 10^{-6} \text{ m}^2 \text{ hr}^{-1}$ (medium flow) $8.3 \times 10^{-6} \text{ m}^2 \text{ hr}^{-1}$ (high flow)	Empirically obtained (Fetter, 2017)
α_L	0.026	Empirically obtained (Fetter, 2017)
ε	0.3	Experimental configuration
$K_{s,HET}$	5.0 g m^{-3}	Rittmann and McCarty (2012)
$K_{s,SOD}$	1.3 g m^{-3}	Fitted to SOD microcosm
$\hat{q}_{SOD} X_{SOD}$	$0.52 \text{ gVSS m}^{-3} \text{ hr}^{-1}$	Fitted to SOD microcosm
$\hat{q}_{HET} X_{HET}$	$0.1 \text{ gVSS m}^{-3} \text{ hr}^{-1}$	Adjustable parameter
L	0.41 m	Experimental configuration
v	0.0005 m hr^{-1} (low flow)	Experimental configuration
	0.001 m hr^{-1} (medium flow)	Experimental configuration
	0.0015 m hr^{-1} (high flow)	Experimental configuration

5.7 Conclusions

Mathematical and numerical models of a packed-bed bioreactor for hybrid adsorption and mixotrophic denitrification have been presented. Several mechanisms occur in the reactor including advection and dispersion, adsorption, and biological denitrification. A process model was developed to describe the processes occurring within the bioreactor. A numerical model was used to simulate advection-dispersion-reaction processes under varying fluid velocity inflow conditions. The model showed reasonable quantitative agreement with experimental data and captured the trend of the data demonstrating how the effluent concentrations fluctuate depending

on the bioreactor residence time. The model could be used in future studies to optimize the design of systems in full-scale applications, where accounting for transient influent conditions is important. However, incorporating dissolution rates from the electron donors and adsorption mechanism would lead to a more robust modeling framework.

5.8 References

- Batchelor, B.; Lawrence, A. W. Autotrophic denitrification using elemental sulfur. *Journal Water Pollution Control Federation* **1978**, 50 (8), 1986–2001.
- Bear, J. Dynamics of Fluids in Porous Media. Elsevier, New York., 1972.
- Costa, P.; Lobo, J. M. S. Modeling and comparison of dissolution profiles. *Eur. J. Pharm. Sci.* **2001**, 13(2), 123-133.
- Crank, J.; Nicolson, P. A practical method for numerical evaluation of solutions of partial differential equations of the heat-conduction type. *Adv. Comput. Math* **1947**, 6, 207-226.
- Cunningham, J. A.; Mendoza-Sanchez, I. Equivalence of two models for biodegradation during contaminant transport in groundwater. *Water Resour. Res.* **2006**, 42(2).
- Diaz-Elsayed, N.; Xu, X.; Balaguer-Barbosa, M.; Zhang, Q. An evaluation of the sustainability of onsite wastewater treatment systems for nutrient management. *Water Res.* **2017**, 121, 186-196.
- Dokoumetzidis, A.; Macheras, P. A century of dissolution research: from Noyes and Whitney to the biopharmaceutics classification system. *Int. J Pharm* **2006**, 321(1-2), 1-11.
- Fetter, C. W.; Boving, T.; Kremer, D. Contaminant hydrogeology. Waveland Press, 2017
- FDOH. Standards for Onsite Sewage Treatment and Disposal Systems, Chapter 64E-6, Florida Administrative Code. Florida Department of Health (FDOH), 2013.
- Howe, K. J.; Crittenden, J. C.; Hand, D. W.; Trussell, R. R.; Tchobanoglous, G. Principles of water treatment. John Wiley & Sons, 2012.
- Krayzelova L.; Lynn T. J.; Banihani Q.; Bartacek J.; Jenicek P.; Ergas, S. J. A Tire-Sulfur Hybrid Adsorption Denitrification (T-SHAD) process for decentralized wastewater treatment. *Water Res.* **2014**, 61, 191-199.
- Lisi, R. D.; Park, J. K.; Stier, J. C. Mitigating nutrient leaching with a sub-surface drainage layer of granulated tires. *Waste Manage.* **2004**, 24(8), 831-839.

Lopez-Ponnada, E. V.; Lynn, T. J.; Peterson, M.; Ergas, S. J.; Mihelcic, J. R. Application of denitrifying wood chip bioreactors for management of residential non-point sources of nitrogen. *J. Biol. Eng.* **2017**, *11*(1), 16.

Lowe, K. S.; Siegrist, R. L. Controlled field experiment for performance evaluation of septic tank effluent treatment during soil infiltration. *J. Environ. Eng.* **2008**, *134*(2), 93-101.

Park, J.Y.; Yoo, Y.J., Biological nitrate removal in industrial wastewater treatment: which electron donor we can choose. *Appl. Microbiol. Biotechnol.* **2009**, *82*, 415-429.

Rittmann, B. E. The significance of biofilms in porous media. *Water Resour. Res.* **1993**, *29*(7), 2195-2202.

Rittmann, B. E.; McCarty, P. L. *Environmental Biotechnology: Principles and Applications*. The McGraw-Hill Companies: NY, 2012.

Sahinkaya, E.; Dursun, N. Sulfur-oxidizing autotrophic and mixotrophic denitrification processes for drinking water treatment: elimination of excess sulfate production and alkalinity requirement. *Chemosphere* **2012**, *89*(2), 144-149.

Sengupta, S.; Ergas, S. J.; Lopez-Luna, E. Investigation of solid-phase buffers for sulfur-oxidizing autotrophic denitrification. *Water Environment Research* **2007**, *79*(13), 2519-2526.

Siegrist, R. L.; McCray, J. E.; Lowe, K. S.; Cath, T. Y.; Munakata-Marr, J. Onsite and Decentralised Wastewater Systems: Advances from a decade of research and educational efforts. *Water* **2013**, pages 77-84.

Smith, D. P.; Otis, R.; Flint, M. Florida passive nitrogen removal study (Final report). Florida Department of Health, Tallahassee, Florida, 2008.

Tong, S.; Rodriguez-Gonzalez, L. C.; Feng, C.; Ergas, S. J. Comparison of particulate pyrite autotrophic denitrification (PPAD) and sulfur oxidizing denitrification (SOD) for treatment of nitrified wastewater. *Water Sci. Technol.* **2017**, *75*(1), 239-246.

USEPA. Decentralized Systems Technology Fact Sheet for Septic Tank and Soil Absorption Systems. EPA 932-F-99-075. United States Environmental Protection Agency. Office of Water, Washington D.C., USA, 1999.

USEPA. The Clean Water Act. United States Environmental Protection Agency. Office of Water, Washington D.C., USA, 2008.

Williamson, K., & McCarty, P. L. A model of substrate utilization by bacterial films. *J. Water Pollut. Control Fed* **1976**, 9-24.

CHAPTER 6:

CONCLUSIONS AND RECOMMENDATIONS

Effective nutrient management is critical to mitigating several negative environmental and health consequences on aquatic ecosystems. Environmental biotechnology is an essential component of managing the nitrogen cycle; however, for high ammonium (NH_4^+) strength wastewater and onsite wastewater treatment (OWT) applications, conventional approaches are stymied due to their heavy reliance on biological nitrogen removal (BNR).

Hybrid adsorption and biological treatment systems (HABiTS) utilize a combination of biological, physical, and chemical processes to overcome the challenges associated with BNR. While experimental studies have shown HABiTS to be effective in terms of nitrogen removal, the interaction between underlying mechanisms within these systems remained somewhat nebulous. This work was motivated by the need to develop a theoretical foundation and new numerical tools that elucidate the underlying complex processes and facilitate the design of full-scale systems involving similar mechanisms.

This dissertation was divided in three chapters; the corresponding research questions, objectives, major findings, and recommendations are provided as follows:

1. Chapter 3: How accurately does an internal diffusion mass transfer model coupled with a bioprocess model that considers a single limiting substrate predict nitrogen speciation in a bioreactor comprised of zeolite and nitrifying microorganisms?

- Develop a homogenous surface diffusion model (HSDM) for surface diffusion kinetics within the intra-crystalline zeolite structure, with an appropriate boundary condition at the zeolite-bulk interface that establishes equilibrium between the solid and liquid phases.

A mathematical model was developed that accounts for ion exchange (IX) of NH_4^+ and sodium (Na^+) at the surface of chabazite, and surface diffusion of adsorbed NH_4^+ within the grains of chabazite. At the zeolite-bulk interface, an IX isotherm derived from the mass action law for IX equilibrium was adopted as a boundary condition. The IX isotherm was found to be in good agreement with experimental batch data. The HSDM with the IX isotherm was also found to be in good agreement with batch kinetic data for the uptake of NH_4^+ ions and release of Na^+ ions.

- Develop bioprocess kinetic models of nitrification and combine with the HSDM model.

Mathematical models of sequential biological conversion of aqueous NH_4^+ to NO_2^- and NO_3^- were developed. Inhibition of the rates of the nitritation and nitrataion due to the presence of NH_4^+ were described by the Andrews equation. These models were fit to experimental data from nitrification inhibition studies and provided a sound description of nitritation and nitrataion rates.

- Implement a numerical algorithm to transform the system of PDEs into algebraic expressions and create a computer code to simulate the process.

A new numerical tool was developed based on a finite difference discretization of the equations describing surface diffusion and nitrification with inhibitory kinetics. The computer code simulated the temporal histories of NH_4^+ , Na^+ , NO_2^- , and NO_3^- in the aqueous phase, and predicted the NH_4^+ in the solid phase.

- Conduct side by side control and hybrid bioreactor experiments to investigate the effect of zeolite amendment on easing nitrification inhibition.

Experiments were conducted to determine the efficacy of amending a bioreactor with chabazite for overcoming nitrification inhibition due to high NH_4^+ concentrations. In the reactors without zeolite, high NH_4^+ was found to be inhibitory to nitrifying microorganisms as evidenced by the accumulation of NO_2^- and relatively low concentration of NO_3^- observed. In contrast, the chabazite amended bioreactor showed a low production of NO_2^- and high production of NO_3^- , which provided support for the hypothesis that the IX process assists in overcoming nitrification inhibition.

- Validate the model by comparing simulation results with experimental data of NH_4^+ , NO_3^- , NO_2^- , and Na^+ concentration data.

Estimates of the chemical species were in good agreement with experimental data, especially considering that no additional parameters were required to fit the experimental data. All model parameters were independently obtained from abiotic and biotic studies. It is envisioned that the model can be useful in assessing reactor size, amount of zeolite material required, and material properties desirable to achieve a particular nitrogen removal performance.

- Recommendations

To improve the accuracy of the model developed, processes that could be accounted for in future work are biofilm growth and competitive IX. Biofilm growth modeling at the continuum scale using a phase-field approach, which is a thermodynamically sound method for free-boundary problems, would be useful in determining the expansion of biofilm over time. For the IX isotherm, a model that takes into consideration the uptake of K^+ ions would lead to more accurate results since an underlying assumption of the model is that exchange occurs strictly between NH_4^+ and Na^+ . For IX kinetics, the Maxwell-Stefan and Nernst-Planck models consider diffusion driven by electrochemical gradients, whereas the HSDM model developed herein only considers Fickian

diffusion. These models have a stronger theoretical foundation than the HSDM; however, the caveat is that more sophisticated numerical solutions would have to be implemented.

2. Chapter 4: Can a mechanistic model of surface diffusion combined with a kinetic algal process model predict the temporal history of nitrogen species and microalgae growth in a bioreactor with zeolite and microalgae?

- Combine a kinetic model of nitrogen utilization by algae under multiple limiting conditions with the HSDM.

The HSDM model developed in Chapter 3 was combined with a co-limitation Monod model accounting for a NH_4^+ and incident light as limiting factors for algal growth. The model also incorporated light attenuation effects due to self-shading of algae. The model represents the first such model of a novel process of IX and algal photosynthesis, referred to as a hybrid adsorption and ion exchange (HAPIX) process.

- Create a computational tool that predicts microalgae growth, and the concentration of NH_4^+ in the bioreactor as a function of time.

A new computational tool was developed based on a finite difference implementation of the differential equations describing the uptake of NH_4^+ by algae as well as algae growth. The computer code can predict the temporal evolution of NH_4^+ for various reactor designs, including various zeolite dosages, light intensity, and reactor sizes.

- Calibrate the mathematical model to experimental data derived for experiments for a specific zeolite dosage.

The HAPIX reactor experiments were conducted for three different dosages of zeolite: 60, 150, and 250 g. The approach adopted established the most sensitive model parameters, and adjusted the most sensitive parameters to minimize the discrepancy between the model predictions

and experimental data for a zeolite dosage of 150 g. The light attenuation constant, k , and the maximum specific growth rate, μ_{\max} were the parameters adjusted; the values were found to have a physically and biologically sound basis based on comparison with literature values.

- Validate the model by comparing simulation results with experimental data of NH_4^+ , and microalgae biomass to experimental data for two different zeolite dosages from the calibrated model.

The computer simulations of NH_4^+ and algal biomass growth as a function of time were compared to HAPIX experimental data for zeolite dosages 60 and 250 g. The computer simulations and experimental data were in reasonable agreement. These results provided credence to the hypothesis that surface diffusion combined with a co-limitation model depending on NH_4^+ and light as factors limiting algal growth is a sufficient theoretical explanation of the HAPIX process. A potential application of the computational tool developed for the HAPIX system would be to screen various system designs based on the purpose for the photobioreactor. More specifically, the amount of chabazite utilized, particle size, and light intensity could be determined to provide either a goal of reaching a required nitrogen concentration.

- Recommendations

Since Chapter 3 and 4 have the same underlying assumptions and use the same modeling approach, similar recommendations are suggested. The description of IX processes can be improved by considering competitive IX isotherm and kinetic models that account for the presence of competing cations. The algal process model adopted a Monod approach, which for practical design purposes is relatively straightforward to implement numerically. However, more rigorous approaches such as constraint-based genome scale metabolic models would provide more insight into the algal processes.

3. Chapter 5: How does a mathematical model of mass transport by advection and dispersion combined with mixotrophic denitrification combined predict the breakthrough characteristics of a tire-sulfur hybrid adsorption denitrification (T-SHAD) bioreactor?

- Develop a mathematical model that translates the simplified system representation into mathematical equations.

A mathematical model of a tire-sulfur adsorption and denitrification (T-SHAD) was developed. The model considered mass transport by advection, dispersion, and biological degradation. Mathematically, the T-SHAD system was described using non-dimensional equations with two important dimensionless groups: Peclet number and Damköhler utilization number. The model predicts the removal behavior of the bioreactor as well as simulates effluent characteristics under varying inflow conditions via changes in the dimensionless groups with changes in velocity.

- Recommendations

The technology previously proposed and implemented at the laboratory scale, referred to as a tire-sulfur hybrid adsorption denitrification system (T-SHAD) showed promising performance in terms of low, steady effluent NO_3^- and SO_4^{2-} concentrations. In addition, the technology utilizes low-cost packing material which improves the system's overall sustainability. Through the development of models that capture the most salient features occurring within the T-SHAD system, the model supported the hypothesis that mixotrophic denitrification indeed occurs and results in lower SO_4^{2-} production than what would be expected based on the stoichiometry of the denitrification reaction.

Overall, the environmental biotechnology systems modeled in this dissertation together with the computational framework have the potential to be applied across wide range of environmental engineering problems related to nutrient management. With increasing computing power that facilitate rapid prototyping of algorithms, it is expected that in the future extensions of

computational framework developed in this dissertation will accelerate the development of new sustainable technologies that address the grand engineering challenges in the 21st century.

APPENDIX A:

COPYRIGHT PERMISSIONS

The permission below is for the use of material in Chapter 3.



[Home](#) [Create Account](#) [Help](#)





Title: Bioregeneration of Chabazite During Nitrification of Centrate from Anaerobically Digested Livestock Waste: Experimental and Modeling Studies
Author: Verónica E. Aponte-Morales, Karl A. Payne, Jeffrey A. Cunningham, et al
Publication: Environmental Science & Technology
Publisher: American Chemical Society
Date: Apr 1, 2018
Copyright © 2018, American Chemical Society

LOGIN
If you're a [copyright.com](#) user, you can login to RightsLink using your [copyright.com](#) credentials. Already a [RightsLink](#) user or want to [learn more?](#)

PERMISSION/LICENSE IS GRANTED FOR YOUR ORDER AT NO CHARGE

This type of permission/license, instead of the standard Terms & Conditions, is sent to you because no fee is being charged for your order. Please note the following:

- Permission is granted for your request in both print and electronic formats, and translations.
- If figures and/or tables were requested, they may be adapted or used in part.
- Please print this page for your records and send a copy of it to your publisher/graduate school.
- Appropriate credit for the requested material should be given as follows: "Reprinted (adapted) with permission from (COMPLETE REFERENCE CITATION). Copyright (YEAR) American Chemical Society." Insert appropriate information in place of the capitalized words.
- One-time permission is granted only for the use specified in your request. No additional uses are granted (such as derivative works or other editions). For any other uses, please submit a new request.

[BACK](#)[CLOSE WINDOW](#)

Copyright © 2018 Copyright Clearance Center, Inc. All Rights Reserved. [Privacy statement](#). [Terms and Conditions](#). Comments? We would like to hear from you. E-mail us at customer@copyright.com

The permission below is for the use of material in Chapter 4.



[Home](#)[Account Info](#)[Help](#)



Title: Hybrid algal photosynthesis and ion exchange (HAPIX) process for high ammonium strength wastewater treatment

Author: Meng Wang, Karl A. Payne, Shuang Tong, Sarina J. Ergas

Publication: Water Research

Publisher: Elsevier

Date: 1 October 2018

© 2018 Elsevier Ltd. All rights reserved.

Logged in as:
Karl Payne
University of South Florida
Account #: 3001286487

[LOGOUT](#)

Please note that, as the author of this Elsevier article, you retain the right to include it in a thesis or dissertation, provided it is not published commercially. Permission is not required, but please ensure that you reference the journal as the original source. For more information on this and on your other retained rights, please visit: <https://www.elsevier.com/about/our-business/policies/copyright#Author-rights>

[BACK](#)[CLOSE WINDOW](#)

Copyright © 2018 [Copyright Clearance Center, Inc.](#) All Rights Reserved. [Privacy statement](#). [Terms and Conditions](#).
Comments? We would like to hear from you. E-mail us at customercare@copyright.com

APPENDIX B:

SUPPLEMENTARY DATA

The following data are associated with the material presented in Chapter 3 of this dissertation. Table B1 presents NH_4^+ -N, Na^+ , NO_2^- -N, NO_3^- -N concentration data over time for experiments conducted without the addition of chabazite. Table B2 presents NH_4^+ -N, Na^+ , NO_2^- -N, NO_3^- -N concentration data over time for experiments conducted with the addition of chabazite.

Table B1: Nitrogen species and sodium data for bioreactor without chabazite

Time (hr)	NH_4^+ -N (meq L ⁻¹)	Na^+ (meq L ⁻¹)	NO_2^- -N (meq L ⁻¹)	NO_3^- -N (meq L ⁻¹)
0	75.52 (0.32)	26.74 (2.23)	0.32 (0.012)	0.083 (0.011)
24	76.94 (1.14)	25.43 (3.42)	0.9 (0.038)	0.093 (0.021)
48	71.26 (0.75)	24.29 (0.05)	1.47 (0.053)	0.034 (0.029)
72	71.35 (0.0064)	22.43 (0.98)	2.48 (0.26)	0.025 (0.022)
96	71.92 (0.045)	25.18 (1.23)	3.18 (0.051)	0.025 (0.048)
120	71.40 (0.03)	22.21 (0.54)	3.55 (0.041)	0.12 (1.43)
144	68.66 (1.18)	25.64 (0.67)	4.28 (0.1)	0.103 (0.0014)
168	71.27 (1.12)	22.90 (1.29)	5.12 (0.12)	0.67 (0.011)
192	66.03 (0.76)	26.77 (5.46)	5.83 (0.12)	0.79 (0.051)

Table B2: Nitrogen species and sodium data for bioreactor with chabazite

Time (hr)	NH₄⁺-N (meq L⁻¹)	Na⁺ (meq L⁻¹)	NO₂⁻-N (meq L⁻¹)	NO₃⁻-N (meq L⁻¹)
0	80.13 (0.5)	24.75 (2.5)	0.023 (0.0021)	0.27 (0.17)
24	10.32 (6.9)	65.35 (2.6)	0.36 (0.51)	1.29 (0.16)
48	9.55 (3.9)	62.31 (6.0)	0.28 (0.45)	3.14 (0.169)
72	9.29 (0.34)	60.34 (2.9)	0.43 (0.21)	4.39 (0.17)
96	7.56 (4.21)	61.33 (7.0)	0.28 (0.32)	5.68 (0.41)
120	7.82 (6.37)	60.53 (3.1)	0.47 (0.48)	6.66 (0.89)
144	7.42 (0.7)	57.52 (1.9)	0.43 (0.38)	7.95 (0.071)
168	7.31 (4.06)	50.44 (2.8)	0.36 (0.27)	10.31 (0.56)
192	6.98 (0.25)	49.16 (3.2)	0.014 (0.005)	11.37 (0.59)